AL-FARABI KAZAKH NATIONAL UNIVERSITY

UDC: 620.3 On manuscript rights

TULEGENOVA MALIKA ASKAROVNA

Anticorrosion protective coatings based on graphene nanostructures

6D071000 – Materials Science and Technology of New Materials

Thesis for the degree of Doctor of Philosophy (PhD)

Scientific consultants:
Doctor of physical-mathematical science
Professor A.M. Ilyin

Doctor of physical-chemistry
Professor G.W. Beall
Texas State University (San Marcos, USA)

The Republic of Kazakhstan
Almaty, 2023

CONTENTS

SYMBOLS AND ABBREVIATIONS

CNT – carbon nanotubes
GO – graphene oxide
RGO – reduced graphene oxide
T-RGO – thermally reduced graphene oxide
HI-RGO – chemically reduced GO with hydroiodic acid
VC-RGO – chemically reduced GO with ascorbic acid
FLG – few-layer graphene
CCG – chemically converted graphene
FGNS – functionalized graphene nanostructures
HOPG – highly oriented pyrolytic graphite
CVD – chemical vapor deposition
RTR – Roll-to-Roll process
QHE – Quantum Hall Effect
DMol3 – it is a commercial (and academic) software package
DFT – density functional theory
H_2SO_4 – sulfuric acid
HCl – hydrogen chloride
HNO_3 – nitric acid
$KMnO_4$ – potassium permanganate
$KClO_3$ – potassium chlorate
$NaNO_3$ – sodium nitrate
ClO_2 – chlorine dioxide
H_2O_2 – hydrogen peroxide
CO – carbon monoxide
CO_2 – carbon dioxide
SiC – silicon carbide
Ga – gallium
GV – graphene containing vacancy
GDV – graphene containing divacancy
AES – Auger electron spectroscopy
SEM – scanning electron microscopy
EDX, EDRS or EDS – energy dispersive X-ray spectroscopy
XRD –X-ray diffraction
TGA – thermogravimetric analysis

INTRODUCTION

The relevance of the study

One of the important constructional, technical and economic problems of our time is the protection of materials and products from the effects of aggressive environmental factors, which include mechanical action, chemical effects of gases and liquids, high temperatures, as well as radiation of various kinds. Such aggressive influences can lead not only to the deterioration of physical and mechanical characteristics, but even to complete destruction. This thesis focuses on the problem of corrosion, which leads to partial or complete destruction of materials as a result of chemical, electrochemical, and physicochemical interaction with the environment. Corrosion of metal products is a widespread problem, especially in industrialized countries with a large number of enterprises, where metal products and equipment are used daily in conditions of aggressive environments, high temperatures and pressures. In the near future the problem of corrosion may become a significant problem of the world economy due to the depletion of world metal reserves and it is necessary to address it now to ensure the safety of the stock of metal products. Based on the above, prediction and prevention of corrosion problems is one of the most important tasks of industry and economy. To solve this problem Nobel Prize winner K.S. Novoselov proposed to use graphene nanostructures as a very effective anticorrosion coating because of their chemical inertness and impermeability.

Ideal defect-free graphene film is capable of becoming ultrathin and effective anticorrosion coating. However, obtaining the graphene film of large size on an industrial scale has certain unresolved technological problems. The difficulties of obtaining the perfect graphene coating can be solved by replacing it with functionalized graphene nanostructures (FGNS), which are much easier to obtain on a large scale and their physical and mechanical properties can be close to those of graphene, which in turn stimulates a huge scientific interest from researchers around the world. Graphene oxide (GO) is one of the most common representatives of FGNS, which can be easily applied to various surfaces, which is a great advantage in coating technologies.

This thesis is devoted to the theoretical and experimental studies of the anticorrosion protective coatings based on graphene nanostructures. A common and optimal method for growing graphene coatings is the chemical vapor deposition (CVD) method, as well as the proposed and implemented method of obtaining graphene by carbon diffusion through nickel. Especially, the graphene grown directly on the surface of copper and nickel by the CVD method has a higher resistance to corrosion in contrast to the transferred graphene. Functionalization of graphene can be carried out by various methods, including oxidation, doping, creation of radiation defects and other methods. There are two main categories of functionalization of graphene: chemical and non-chemical. Both types of functionalization contribute to changing the properties of graphene, but the most effective and cost-effective is the chemical modification.

The detailed study of nanosystems associated with the creation of protective coatings is a difficult task even for well-equipped laboratories. An important method to study and predict the barrier properties of graphene nanostructures is computer simulation and quantum-mechanical numerical calculations. The use of numerical methods such as DFT allows us to obtain sufficiently accurate information about the properties of the studied complex nanosystems and to predict their behavior under different external factors. Computer models of nanomaterials allow researchers to better understand their features and open up new possibilities for functionalizing and modifying their physical, mechanical and chemical properties.

The purpose of the thesis is the theoretical and experimental study of the effectiveness of anticorrosion protective coatings based on graphene nanostructures under the influence of external factors.

The tasks of the thesis:

1. Computer simulation of graphene nanostructures, calculation of the efficiency of their anticorrosion properties using "first-principles" methods;
2. Development of technology for obtaining coatings based on graphene nanostructures on the surface of copper and nickel for corrosion protection;
3. Study of the protection efficiency of the obtained coatings based on graphene nanostructures by energy dispersive X-ray spectroscopy under the influence of various external factors;
4. Development of a specialized Auger analyzer for the analysis of ultrathin layers of anticorrosion protective coatings based on graphene nanostructures.

The objects of the study are protective coatings based on graphene and FGNS.

The subject of the research

Anticorrosion properties of graphene nanostructures under the influence of various external factors.

The methodological basis of the study

Quantum-mechanical numerical methods of the density functional theory, technology for obtaining graphene nanostructures by chemical vapor deposition, obtaining of graphene nanostructures by the diffusion method under vacuum conditions, obtaining graphene oxide films by electrophoretic deposition, analytical methods (optical microscopy, electron microscopy, Raman spectroscopy, Auger electron spectroscopy, energy dispersive X-ray spectroscopy, thermogravimetric analysis, X-ray diffraction).

The scientific novelty of the thesis

1. For the first time, computer simulation and quantum-mechanical numerical calculations of various possible situations were carried out, where graphene nanostructures demonstrate a sufficiently high energy barrier when an oxygen molecule penetrates through them;
2. The method of deposition of graphene oxide film by preliminary heat treatment in a flow tube in a stream of argon-hydrogen mixture (90% Ar + 10% H_2) was improved, which enhanced the adhesive properties and resistance of anticorrosion protective coatings;

3. For the first time was shown high efficiency and reliability of anticorrosion protective coatings based on graphene at temperature exposure using complex methods of materials characterization;

4. For the first time was developed a specialized electrostatic energy analyzer for Auger electron spectroscopy, allowing to analyze ultrathin layers of anticorrosion protective coatings based on graphene nanostructures.

The scientific and practical significance of the study

The obtained results are of both theoretical and practical value. In terms of theoretical value, the computer simulation is of great scientific interest, since it is able to predict and evaluate the anticorrosion protective properties of graphene nanostructures at the nanoscale, which is difficult to achieve in real laboratory conditions. It is well known that today computer simulation is an indispensable tool for solving a wide range of problems in physics and chemistry, including the study of corrosion processes.

The simulation results predict the high efficiency of the protective properties of the anticorrosion coatings based on graphene nanostructures. Moreover, the experimental results obtained in the course of the work are in good agreement with the quantum-mechanical calculations, which is of great practical interest for industrial, shipbuilding, oil and gas and other companies that incur huge annual losses when dealing with corrosion-related problems.

During the thesis work for a more accurate quantitative analysis of the composition and structure of graphene's thin layers, a specialized Auger analyzer was developed and this method of analysis was implemented in the ultrahigh vacuum unit USU-4, due to which the sensitive analysis to light elements of thin near-surface layers of various materials became possible.

The main provisions for the defense of the thesis

1. Ideal graphene, graphenes with structural defects in the form of vacancy, divacancy and a small gap in the sheet (0.25 nm) have a high efficiency of protective effect against oxygen penetration due to the formation of a potential barrier when the oxygen molecule interacts with the surface of the graphene layer.

2. In the graphene sheet with sufficiently large gaps (0.45 nm) the maintenance of high efficiency of protective effect against oxygen penetration is achieved by its functionalization with impurity gallium atoms due to the formation of a strong Ga-C covalent bond (2.6 eV) and high oxygen adsorption energy of gallium (1.8 eV).

3. Anticorrosion graphene coatings obtained by chemical vapor deposition demonstrate reliable protection of copper and nickel surfaces from thermal corrosion, which is associated with the high quality of the coatings (D/G ratio ≈ 0.08).

4. Auger spectrometer, designed and implemented using the Conical Face-Field Electrostatic Energy Analyzer ($R_E \approx 0.71$ % for $\gamma = -0.04$ and $R_E \approx 0.60$ % for $\gamma=0$), allows to control both small and large areas of anticorrosion graphene coatings, as well as their structures in situ.

The author's personal contribution

Computer models and theoretical calculations were carried out by the author using the DFT method in Dmol3 module of the Materials Studio program.

Experimental studies of the anticorrosion protective coatings based on graphene nanostructures, namely, obtaining, processing and analysis of the results were performed independently. Author also completed a scientific internship from June 15 to September 15, 2019 under the guidance of Dr. G.W. Beall at Texas State University in San Marcos, Texas, USA.

Publications

Based on the thesis materials 11 publications were made, including 3 articles published in journals recommended by the Committee for Control of Education and Science of the Ministry of Education and Science of the Republic of Kazakhstan, 1 article was published in the “Journal of Electron Spectroscopy and Related Phenomena” in 2022, which is included in Scopus database (percentile: 60%), 2 articles published in 2019 in the “Journal of Computational and Theoretical Nanoscience” included in Scopus database, 1 article in international journal “Journal of Materials Science and Engineering B” and 4 abstracts published at national and international conferences.

Relation of the dissertation topic with the plans of scientific works

This dissertation work was carried out within the scientific project № AP05130413 "Development of technology for creating protective coatings based on functionalized graphene nanostructures and researching their properties" funded under the grant funding for scientific and (or) scientific and technical projects of the Committee of Science of the Ministry of Education and Science of Kazakhstan.

Volume and structure of the thesis

The thesis contains a list of symbols and abbreviations, an introduction, the main part of 3 sections, a conclusion and a list of references. The work is presented on 102 pages, contains 69 figures, 5 tables and 232 bibliographical references.

1 LITERATURE REVIEW

1.1 Corrosion of materials and corrosion protection methods

Corrosion is the destructive result of an electrochemical reaction between a metal or alloy and its environment [1].

There are generally two types of corrosion, which include "dry" and "wet" corrosion [2]. Dry corrosion occurs in the absence of water or moisture contributing to corrosion, resulting in the metal oxidizes only in the atmosphere. Wet corrosion of metals occurs through electron transfer involving two reactions: oxidation and reduction [3]. Oxidation can be very simply described using the electrochemical reaction equation (1) [4], in which the metal atom M donates one or more electrons to become a cation.

$$M \rightarrow M^{n+} + ne^{-} \quad (1)$$

The reduction reaction will only occur in the presence of an appropriate cathode reagent, which is used to obtain electrons; in aqueous solutions, it is usually one of the following [4]: in acidic solutions (2), in neutral or alkaline solutions (3).

$$2H^{+} + 2e^{-} \rightarrow H_2 \quad (2)$$

$$1/2O_2 + H_2O + 2e^{-} \rightarrow 2(OH)^{-} \quad (3)$$

Metal ions can remain dissolved in solution or can react with other ions and precipitate as solid compounds.

As in any other electrical circuit, the passage of electrons between the anode and cathode generates a current. Measurements of electrochemical corrosion are based on a direct or indirect measurement of this current using Faraday's law to convert it into corrosion rate such as material losses expressed in μm/yr [1].

Some metals can still resist certain aggressive environmental factors by reducing the rate of corrosion as a result of reaction with the environment through the formation of a surface passivating film, usually an oxide or hydroxide. Passivity is the ability of a metal to resist corrosion despite the thermodynamic tendency of the metal to react with an aggressive environment [5]. Surface oxides can exhibit more significant protective properties under the influence of anodic polarization (noble potentials) and maintain a low current density at the anode, significantly slowing the destructive dissolution of the metal [5,6]. Surface oxides/hydroxides usually increase the noble properties and hence the corrosion resistance [6,7].

The effects of corrosion in our daily lives can be both direct, i.e. corrosion affects the useful life of our property, and indirect, which includes costs and damages from corrosion. In everyday life, we can easily see examples of the direct effects of corrosion on cars body panels, braziers, outdoor furniture and metal tools. Protection of such items from corrosion can be achieved through preventive maintenance, such

as painting. The indirect impact of corrosion on our economy has been investigated by the corrosion control standards and certification association NACE International, where findings based on a two-year global study were published [8]. According to the data, the annual global cost of corrosion is $2.5 trillion, equivalent to about 3.4% of the world's gross domestic product. The implementation of advanced corrosion prevention techniques could result in global savings of 15-35% of these costs, or $375-875 billion annually.

Corrosion can lead to much more serious consequences, even during an ordinary car ride. Corrosion of steel reinforcement in concrete can flow out of sight and suddenly cause the collapse of a highway section, the collapse of an electric tower and damage buildings, parking structures and bridges, resulting in significant repair costs and posing a threat to public safety. For example, the sudden collapse due to fatigue corrosion of the Silver Bridge over the Ohio River at Point Pleasant in 1967, which led to the death of 46 people and cost millions of dollars [9].

Perhaps the most dangerous of all is the corrosion that occurs in large industrial plants, such as power plants or chemical processing plants. There are many cases of corrosion-related injuries and deaths, but by far the worst man-made disaster in terms of loss of life, injuries, and subsequent health problems is the explosion at the Bhopal chemical plant in India in 1984 (Figure 1). This plant was part of India's "Green Revolution" designed to provide fertilizers and pesticides. However, a series of design flaws and management problems converged to cause a catastrophic explosion. According to reports, when steel pipes corroded and water leaked into tanks containing methylisocyanate, corrosion products from the iron created a reaction that blew up the plant, allowing methylisocyanate and other toxic gases to escape, killing more than 8000 people. Since then, another 15000 people have died in the explosion and approximately 500000 people suffer from gas-induced disorders [10-13].

Figure 1 – Burned down pesticide plant in Bhopal (India) after an explosion in 1984 [14]

Corrosion occurs in several widely varying forms. The classification is usually based on one of three factors [15]:

- Nature of corrosion source: As mentioned earlier, corrosion can be classified as "wet" or "dry" [2].
- Mechanism of corrosion: Includes electrochemical or direct chemical reaction.
- Appearance of corroded metal: Corrosion is either uniform and the metal corrodes at the same rate over the entire surface, or localized, in which case only small areas are affected.

Classification by appearance, based on the identification of corrosion forms by visual observation with the naked eye or by magnification. The morphology of the corroded area is the basis for classification. Figure 2 schematically illustrates some of the most common forms of corrosion.

According to the appearance of metal corrosion, eight forms of wet corrosion can be defined [15]. These are:

- Uniformcorrosion
- Pitting corrosion
- Crevice corrosion, which includes corrosion under bumps or deposits, filamentous corrosion, and abrasion-chemical corrosion

- Galvanic corrosion
- Erosion corrosion, which includes cavitation erosion and frictional corrosion
- Intergranular corrosion, which includes sensitization and corrosion delamination
- Dealloying corrosion of one or more components from solid solution, which includes removal of zinc alloys and graphite corrosion
- Cracking, formed by exposure to the environment, which includes stress corrosion cracking, corrosion fatigue, and hydrogen damage

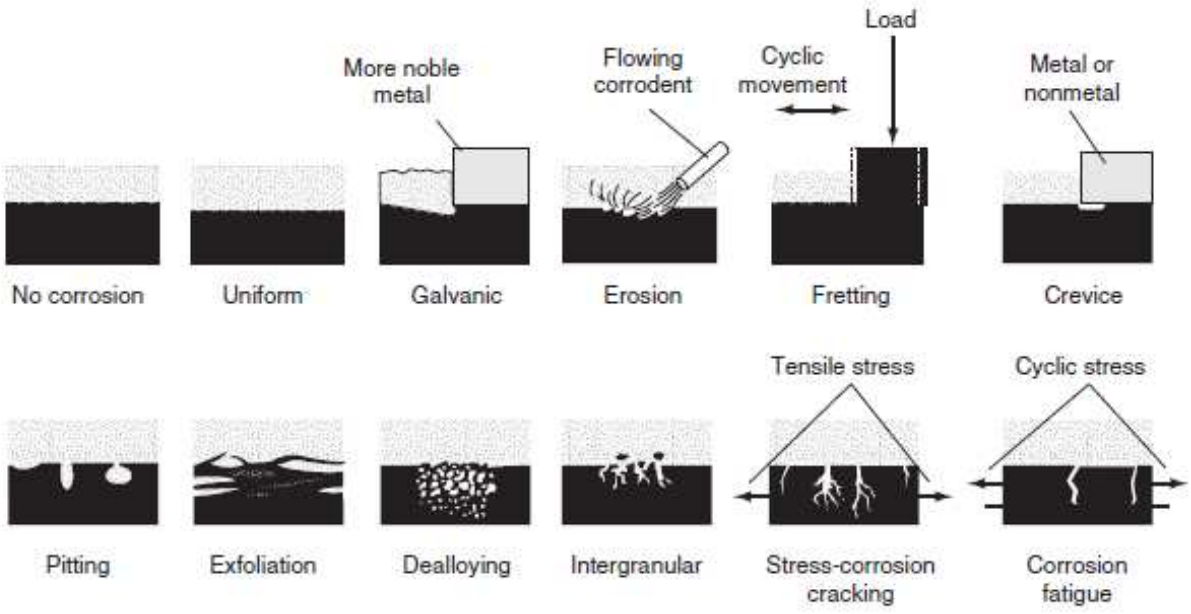

Figure 2 – Schemes of common forms of corrosion [15]

There are five basic methods of corrosion control: material selection, use of coatings, cathodic protection, addition of inhibitors and the necessary design solution [15]. In this thesis we deal specifically with protective coatings.

Coatings for corrosion protection can be divided into two broad groups - metallic (e.g., noble Cr and sacrificial Zn coating) and non-metallic, which in turn are divided into organic (e.g., resins and latexes) and inorganic (e.g., zinc silicate and SiO_2 coatings). These materials are widely used to protect metals from corrosion through barriers, inhibition and galvanic effects (anodic protection) [16, 17].

Barrier protective coatings hinder the penetration of oxygen or help slow down corrosion. An inhibitor is a substance (or combination of substances) that is added in a very low concentration to treat the surface of a metal exposed to a corrosive environment to stop or mitigate corrosion [18]. The common expression "anodic protection" refers to a method of corrosion protection for certain metals and alloys in an aggressive chemical environment by anodic polarization with an external DC power supply. Keeping the metal surface in a passive state practically stops the corrosion processes. However, it should be noted that the phenomenon of anodic passivity can occur in the case of contact with other metals that have a potential with

more positive values. Cathodic coatings that cause anodic passivity are an example. The same role is played by platinum, palladium or copper impurities introduced into steel alloys. This method of protection is sometimes called galvanic anodic protection [19].

Anticorrosion coatings have attracted much attention over the years due to their simplicity and effectiveness [20-22]. Numerous anticorrosion coatings have been developed and tested to combat the detrimental effects of corrosion on metal. Because of differences in the physical and chemical properties of different types of metals and alloys, the protection provided by each coating depends on the type of metal to which it is applied and the environment in which it is exposed. As material science advances, new anticorrosion coating systems are being developed. The development of these coatings is focused on expanding functionality, including corrosion protection and adhesion, environmentally friendly materials, corrosion and mechanical damage detection, improved fatigue strength and water resistance [23].

1.2 Structure and basic properties of graphene

For 60 years there is a theoretical study of the existence possibility of graphene or two-dimensional (2D) allotropic modification of carbon. Often the term graphene was used to describe the properties of carbon allotropic modifications [24-26]. However, four decades later it became clear that graphene also forms a perfect analog of the condensed matter (2+1)-dimensional quantum electrodynamics [27-30], thus demonstrating graphene on the dynamically developing theoretical "toy" model [30]. It was expected that graphene would be unstable due to the formation of bent structures such as soot, fullerenes and nanotubes. Experimental study of the properties of graphene, as a separate object, almost did not exist until very recent years because of the difficulty to identify and unambiguously characterize a sheet that is one atom thick. In addition, it was believed that graphene does not exist in its free state. Unexpectedly, in 2004, model calculations of graphene became true when Geim and Novoselov discovered free-standing graphene, resulting in them sharing the 2010 Nobel Prize in Physics for its discovery [30-32].

Graphene is a new two-dimensional allotropic modification of carbon that has a hexagonal (honeycomb) lattice structure, one atom thick, where the carbon-carbon bond length is about 0.142 nm, as shown in Figure 3 [30,33]. In other words, it is a single layer of graphite with sp^2 hybridized carbon atoms.

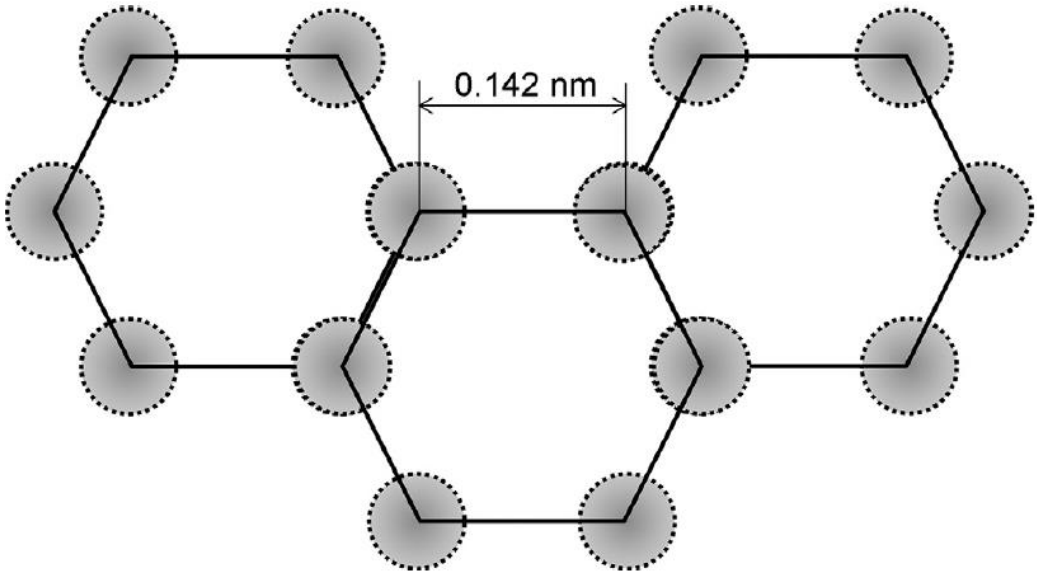

Figure 3 – Hexagonal lattice of graphene [33]

The electrical conductivity of graphene is mainly due to π-bonding, located vertically to the lattice plane. The stability of graphene is due to tightly packed carbon atoms and sp^2 hybridization of atomic orbitals - a combination of s, p_x and p_y orbitals, which form a σ-bond. The final p_z-electron forms a π-bond. The π-bonds hybridize together to form the π-zone and π*-zone. These zones are responsible for most of the exceptional electronic properties of graphene, due to the half-filled zone that allows electrons to move freely [33]. In addition, graphene is the basic structural element of all other graphite materials, such as zero-dimensional (0D) fullerenes, one-dimensional (1D) carbon nanotubes (CNTs) and three-dimensional (3D) graphite [34] (Figure 4).

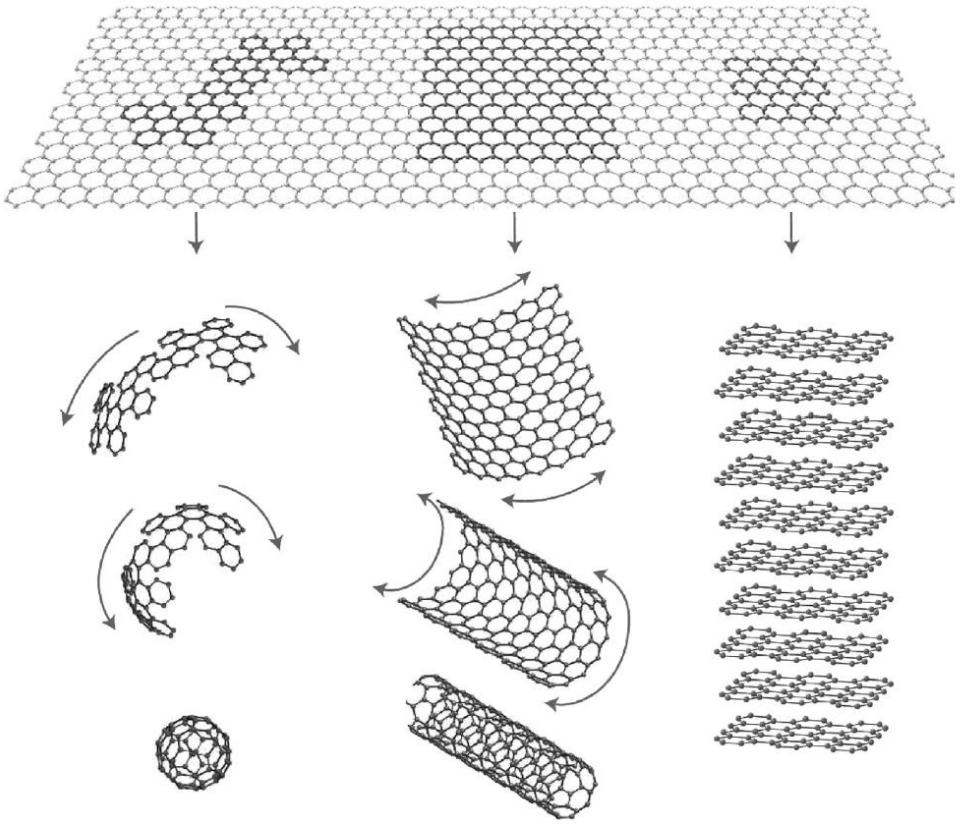

From left to right, respectively: (0D) fullerenes, (1D) CNT, (3D) graphite

Figure 4 – Allotropic modifications of carbon [30]

Like CNT, the edge of graphene can be classified into zigzag and armchair configurations based on different carbon chains, as shown in Figure 5. The variety of configurations at the edges leads to different behavior of electrical conductivity. A graphene nanoribbon with a zigzag edge typically behaves like a metal, while a nanoribbon with an armchair edge can conduct electricity like a metal or a semiconductor [33].

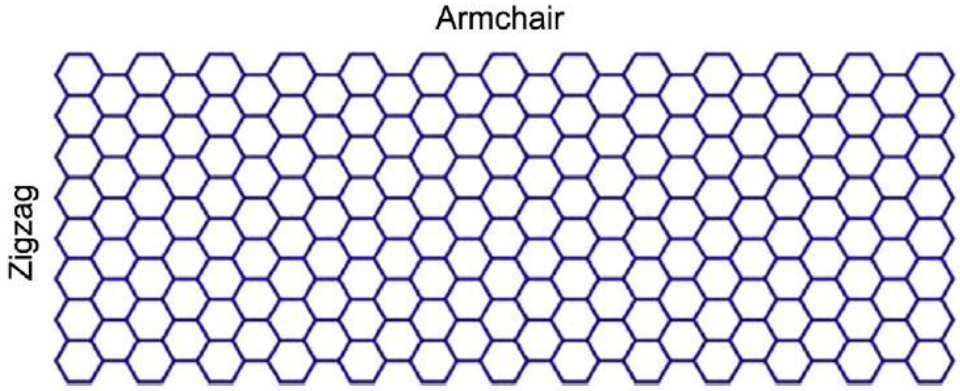

Figure 5 – Graphene nanoribbon [33]

Graphene has a wide potential application due to its excellent mechanical, electrical, thermal and optical properties and its large surface to mass ratio (for example, 1 g of graphene can cover soccer field) [35, 36]. The literature reports remarkable properties of graphene: Young's modulus is about 1100 GPa [37]; tensile strength is 125 GPa [37]; thermal conductivity is about 5000 W/mK [38]; charge carrier mobility is 200000 cm^2/Vs [39]; and calculated specific surface area value of 2630 m^2/g [40]. Graphene has a remarkable transport phenomenon, namely the Quantum Hall Effect (QHE) [41]. The exceptional thermal, optical and electrical properties of graphene are the result of its elongated π-π-coupling [34].

1.3 Methods of graphene production

This section focuses on the main methods for producing graphene. The main characteristics of the most common methods of graphene production are shown in Figure 6. Graphene was first obtained by mechanical exfoliation in 2004. It was this simple method that produced free-standing graphene, for which Geim and Novoselov were awarded the Nobel Prize [42]. The Scotch tape method is an alternative name for the micromechanical exfoliation method, since here scotch tape is used to repeatedly split a piece of graphite, after which the material is transferred to a substrate. This method of obtaining graphene has a significant disadvantage due to the inability to scale up the production process, but is still very common because it allows the creation of high-quality crystals, which is invaluable for basic research and prototyping.

Liquid-phase exfoliation is one of the methods for the production of graphene produced by the separation of graphite caused by ultrasound treatment in a liquid medium. The method basically includes three different steps: (1) dispersion of graphite in a solvent or surfactant, (2) exfoliation, and (3) purification [43,44]. In the exfoliation stage, the ultrasound treatment time is very important because higher concentrations of graphene can be achieved due to longer ultrasound treatment time. After the ultrasound treatment stage comes the purification, where thicker flakes can be separated from thinner flakes by centrifugation. Liquid-phase exfoliation is one of the most promising methods of mass production of graphene due to its simplicity and high productivity.

The method of electrochemical exfoliation consists in the use of carbon sources (graphite, rods of highly oriented pyrolytic graphite, graphite foil) as electrodes in a liquid electrolyte solution. Electrochemical reactions result in the splitting of graphite to graphene. Good quality graphene materials were obtained in [45-48], which showed comparable or somewhere even better characteristics than other types of graphene when they were tested for various applications (as adsorbents, electrodes for supercapacitors, conductive films, etc.). The main advantage of this method is the one-stage process, which makes it significantly easier and faster compared to other methods of graphene production.

Chemical reduction of graphene oxide (GO) is one of the most promising and inexpensive methods of producing graphene-like monolayers on a larger scale. The essence of this method is the delamination of graphene oxide into single-layered

sheets and removal of functional groups in the process (reduction). The quality of the resulting material is highly dependent on the choice of solvent, reducing agent and surfactant. The resulting material is commonly referred to as reduced graphene oxide (RGO), as it is not quite correct to classify it as graphene due to the content of not only its own defects (edge, deformation), but also impurity defects (not completely removed O- and H-containing groups). Another disadvantage of this method is the use of toxic reducing agents, such as hydrazine monohydrate [49], sulfur-containing compounds [50], sodium borohydride, etc. Despite the existing drawbacks, the chemical reduction of graphene oxide has great potential for obtaining graphene-like material in large volumes, which is convenient for its application. Also some recent works try to replace toxic chemical reducing agents with green reducing agents [51-53].

Epitaxial method of growing graphene consists of dissolution of carbon in transition metals such as ruthenium, iridium, platinum, palladium, nickel, etc. at high temperatures and the subsequent release of carbon on the metal surface due to compression of the crystal lattice when cooling in a high or ultrahigh vacuum. Our team obtained graphene and few-layer graphene (FLG) nanostructures by diffusion of carbon through polycrystalline nickel under high vacuum conditions. Highly oriented pyrolytic graphite was used as a carbon source [54]. The graphene samples obtained by the proposed method had excellent quality. A promising method for obtaining epitaxial high-quality graphene is the thermal decomposition of SiC. The advantages of this method are mainly related to the scale of the synthesized graphene samples. Thus, with high quality of the original crystal, the size of the graphene can be comparable with the size of the crystal itself. Although this method has a number of advantages due to its simplicity and efficiency, but the great difficulties associated with the process of transferring the obtained graphene to another substrate limit its application in the manufacture of final devices. In turn, the graphene produced on SiC can be used without transfer in the electrical devices.

A very common and promising method for obtaining graphene is the method of chemical vapor deposition (CVD method) because of its cost-effectiveness and availability. This method produces graphene of sufficiently high quality on the surfaces of transition metals such as Ni, Pd, Ru, Ir, Cu, etc. The method is based on the decomposition of carbon-containing substances (hydrocarbon precursors) on the substrate surface at high temperatures. Not only gaseous hydrocarbons, such as methane or ethylene, but also liquid hydrocarbons, such as hexane [55], pentane [56] or benzene are used as precursors. Many scientists involved in the production and synthesis of graphene have focused their attention on this method because of the possibility of obtaining high-quality samples of large area, which, in turn, can be the optimal solution for the scalability of the graphene nanostructure production process. The team of Bae et al. [57] were one of the first to obtain a good 30-inch graphene film using the Roll-to-Roll (RTR) process. The RTR method was subsequently used to stably obtain the graphene film on metal surfaces. Despite all the advantages, the CVD method is quite a complicated process, requiring precise control of the synthesis parameters, including the choice of the substrate and precursor type [58].

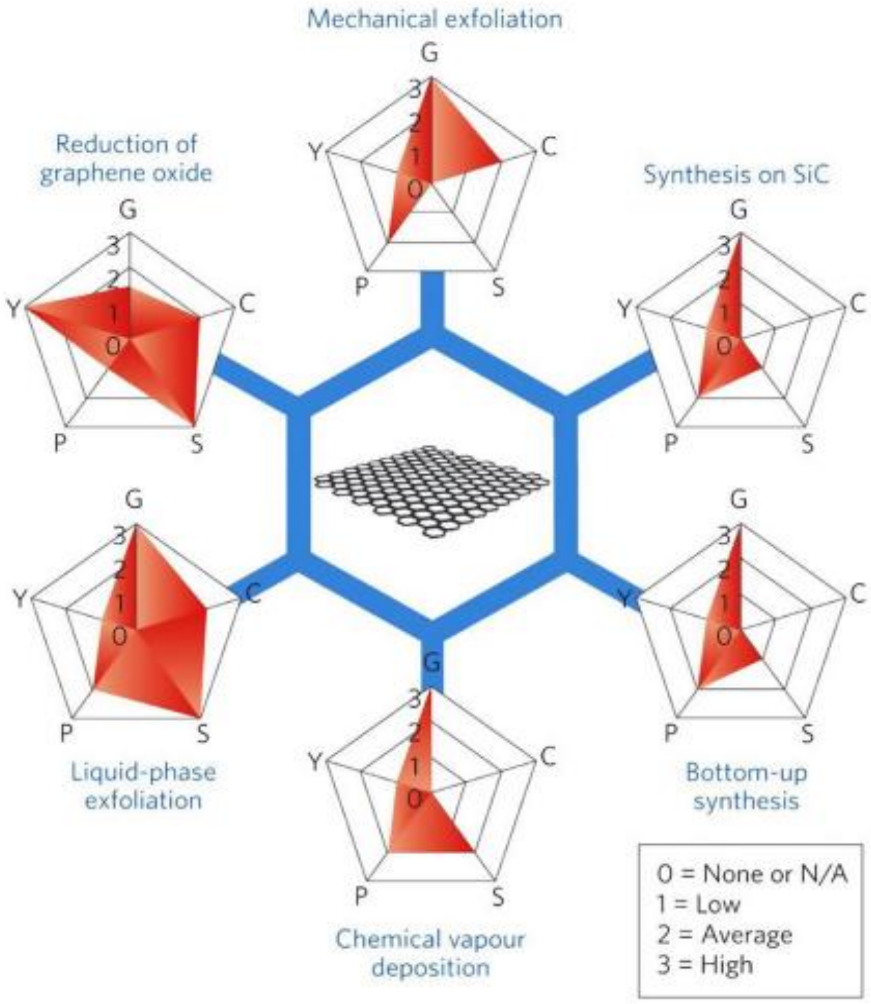

G - quality of graphene, C - production cost (low value corresponds to high production cost), S - scalability, P - purity and Y - product yield

Figure 6 – The main characteristics of the most common methods of graphene production from 0-3 [59]

Formation of graphene by the bottom-up approach starts from the lower orders, where the material is formed atom by atom [60]. In the bottom-up synthesis of graphene it is possible to accurately control the growth process at the atomic level, which avoids a large number of defects. This process is difficult to scale, which is a big disadvantage when used in production, but the resulting high quality graphene is very useful for research purposes.

1.4 Functionalized graphene nanostructures

As mentioned earlier, there are many ways to obtain graphene with relatively perfect structural characteristics, but no matter how many methods exist, the problem of obtaining graphene by economic methods on a large scale with a high degree of purity and satisfactory properties remains far from being solved. For this reason, graphene is not in great demand in commercial applications [61]. A solution to this problem could be the replacement of pure graphene with functionalized graphene

nanostructures (FGNS). FGNS can be close in physical and mechanical properties to graphene and they can be produced on a larger scale. Graphene functionalization methods include: oxidation [68-70], irradiation, ion-atom implantation [86], reduction of graphene oxides [72-75], etc. One of the common representatives of FGNS is graphene oxide. Graphite oxide is obtained by oxidizing inexpensive graphite with hydroxyl, alkoxy, carbonyl, carboxylic acid and other oxygen-containing functional groups [62], which increases the spacing of graphite sheets from 0.336 nm [63] to about 1 nm [49,64,65]. The process of graphite oxidation leads to a change in the strength between graphite layers, so graphite oxide can be stratified into single layers of graphene oxide using ultrasound. Graphene oxide is reduced to graphene nanostructures in order to obtain a material that will be close in structure and properties to pure graphene. The reduction process implies the removal of all oxygen-containing functional groups [66]. At the moment it remains impossible to get rid of all oxygen-containing functional groups, but scientists from all over the world are working to eliminate this problem. Figure 7 shows the transition process from graphite to reduced graphene oxide (another name chemically converted graphene (CCG)) [67].

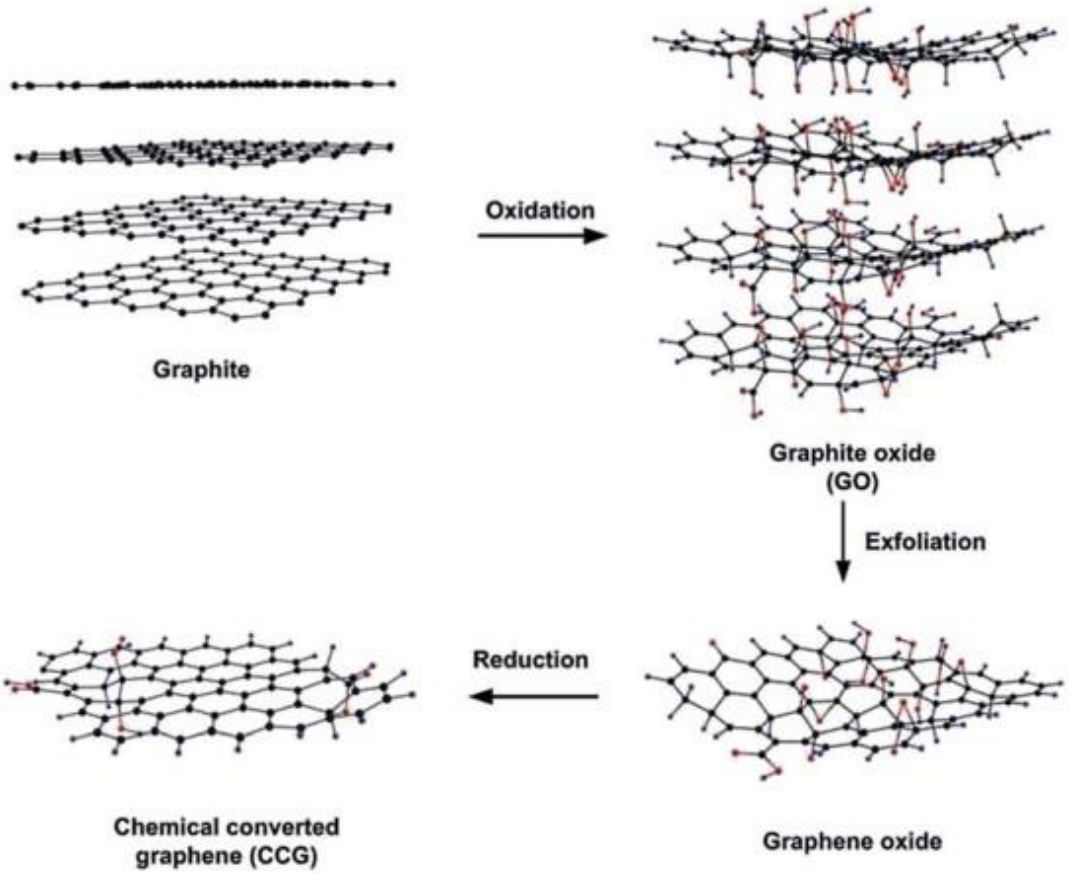

Figure 7 – Illustration of the transition process from graphite to reduced graphene oxide (another name CCG) [67]

Brodie [68], Staudenmaier [69] and Hummers [70] are the first who synthesized graphene oxide by oxidation of graphite by different methods. The essence of these methods for obtaining graphene oxide is that graphite powder chemically reacts with acids (H_2SO_4, HCl and HNO_3, etc.), after which alkali metals (alkali metal compounds $KMnO_4$, $KClO_3$, $NaNO_3$, etc.) are introduced into graphite layers, which additionally contributes to the destruction of graphite layers into smaller pieces. Graphite oxide can be stratified into single-layer and few-layer sheets of graphene oxide under mechanical forces such as ultrasonic treatment. Staudenmaier and Brodie obtain GO by the chlorate route and Hummers by the permanganate route. Hummers made some modifications to the other two methods to make the process safer, which includes using $KMnO_4$ in combination with H_2SO_4 [71] rather than $KClO_3$, which emits the toxic gas ClO_2, and adding $NaNO_3$ to form nitric acid in the process instead of using it as a solvent. One problem with this method is contamination by excess permanganate ions, which can be solved by H_2O_2 treatment followed by water washing. The Hummers' method and its modifications are the preferred method of GO production because of its safer nature as well as the shorter reaction completion time.

Graphene oxide reduction is usually performed by removing functional groups to restore the original hexagonal structure of graphene containing sp^2 -hybridized carbon-carbon bonds. RGO, which is close to the properties of graphene, can be produced on a larger scale, which will contribute to its active practical application. This topic is very topical, so there are many methods of GO reduction, which include thermal reduction [72], chemical reduction [73], photocatalytic reduction [74], solvothermal reduction [75], etc. Each method has its advantages and disadvantages, but chemical and thermal reduction are considered the most common methods of GO reduction.

Thermal reduction is a process of thermal annealing of dried GO. In thermal heating, the atmosphere in which the process takes place plays an important role. Thermal reduction is usually performed in an inert atmosphere [76], in a reducing atmosphere [76-78], or in a vacuum [79]. When the GO is heated, multistep removal of intercalated H_2O molecules and oxygen-containing functional groups occurs. Thermally reduced graphene oxide can have better barrier properties compared to chemically reduced graphene oxide [80]. However, thermal annealing of GO leads to embrittlement of the resulting RGO [80]. There is a suggestion that rapid heating causes the formation of gases such as CO, CO_2, and H_2, which lift the RGO sheets as they leave the material and remain in the same elevated position [66]. In thermal reduction, there are certain requirements for the used substrate material. First of all, the substrate must be able to withstand the heat treatment and GO is preferably applied to the substrate to be used in the final product. Also, it takes a long time at high temperatures to achieve a high C/O ratio, making thermal reduction an energy-consuming process. Thermally reduced graphene oxide can be used in electronic devices, as well as in anticorrosion coatings.

Chemical reduction of GO is the most preferred method of synthesizing RGO on a large scale. For the process of chemical reduction of GO, a homogeneous

aqueous dispersion of GO is used. There are many methods of chemical reduction based on the interaction of GO with a reducing agent. Depending on the purpose of the RGO application, a suitable chemical process can be chosen. In the process of chemical reduction, most of the oxygen-containing functional groups are eliminated and the π-electron conjugation in the aromatic system of graphene is partially restored. The resulting RGO is almost similar to graphene, but still contains residual functional groups and structural defects. The most common GO reducing agent is hydrazine because of its efficiency, which was first proposed by Stankovich et al. [49]. However, hydrazine is trying to replace with less toxic and explosive reducing agents, with the help of which it is possible to obtain a RGO with a more perfect structure and properties. At the moment there are studies involving such reducing agents as ascorbic acid (vitamin C) [81], [82], green tea extract [83], chitosan [84], oxalic acid [85], etc. Chemical reduction can be performed at moderate heat or ambient temperature, which is a great advantage over thermal reduction.

GO is capable of forming stable aqueous colloids due to its high hydrophilicity, which makes it very easy to assemble macroscopic structures using simple dissolution processes. It is also relatively easy to create macroscopic structures from RGO if it is stable in solution. This ability is important for the large-scale use of GO and RGO, so this topic is of continuing relevance and is of particular interest to researchers.

1.5 Anticorrosion coatings based on graphene nanostructures

Corrosion of metals such as copper, nickel, carbon steel and magnesium affects industrial production, which in turn causes huge economic losses. The solution to this problem are corrosion resistant coatings that can insulate the underlying metal from aggressive media, thereby reducing the risk of corrosion. Anticorrosion coating for metal surfaces is an economical and effective method of corrosion protection. In recent years, graphene coatings for the protection of metals against oxidation and corrosion have become widespread due to the properties of strength, impermeability, chemical inertness and hydrophobicity. Graphene is an ultrathin coating and its anticorrosion effect is superior to traditional anticorrosion coatings without changing the initial thermal/electrical conductivity of the substrate [87, 88].

The study of the corrosion resistance of pure graphene coatings dates back to 2011 [89]. Protective graphene films usually covered the surfaces of metals such as copper, nickel, steel, titanium, aluminum alloy, magnesium alloy, etc. [90-98]. Many methods of coating based on graphene nanostructures have been proposed, but the CVD method has been one of the most commonly used methods because of its simplicity and efficiency. The graphene coating obtained by the CVD method provides corrosion protection for not only copper or nickel, but also provides surface protection for alloys, carbon and stainless steel [99-105]. Prasai et al. studied the anticorrosion properties of graphene coatings in aerated Na_2SO_4 solution to protect the surface of Cu and Ni metals. According to Tafel analysis, the corrosion rate of graphene-coated Cu was seven times slower than that of uncoated Cu. SEM micrographs show that the uncoated Cu was uniformly corroded and there were

numerous corrosion products of white copper oxide on the surface. At the same time, the copper protected by the anticorrosion graphene coating was almost not corroded and small amounts of corrosion products appeared in the cracks of the coating only (Figure 8 (a)). The results showed that the corrosion rate of uncoated nickel was 20 times higher than the corrosion rate of graphene-coated nickel. The corrosion resistance of anticorrosion graphene coating obtained by mechanical transfer was also tested. The corrosion resistance of the transferred two-layer and four-layer protective graphene coatings was compared. It was determined that the thicker the graphene coating, the lower the corrosion rate (Figure 8 (b,c,d)). Based on the results of the analysis, it is clear that the transferred graphene still prevents the attack of the aggressive environment on the substrate, which ensures the protection of the underlying metal [88]. Although only certain metal substrates (copper, nickel) can be used to obtain high-quality graphene nanostructures by CVD method, the mechanical transfer method allowed the anticorrosion graphene film to cover the surface of any metallic material. Yuda Zhao et al. prepared monolayer graphene films by CVD on the copper surface and then transplanted them to the silver surface by mechanical transfer [106]. Transparent and ultrathin protective coatings were formed on the surface of silver thin films, which can be used for optical applications. Based on Tafel analysis the corrosion rate of graphene-coated silver was about 66 times lower than that of pure silver. Monolayer graphene demonstrated not only high corrosion resistance to gases and liquids, but also had excellent transparency. Thus, silver coated with graphene films retains its original optical properties, as well as maintains high stability and resistance to oxidation in corrosive environments.

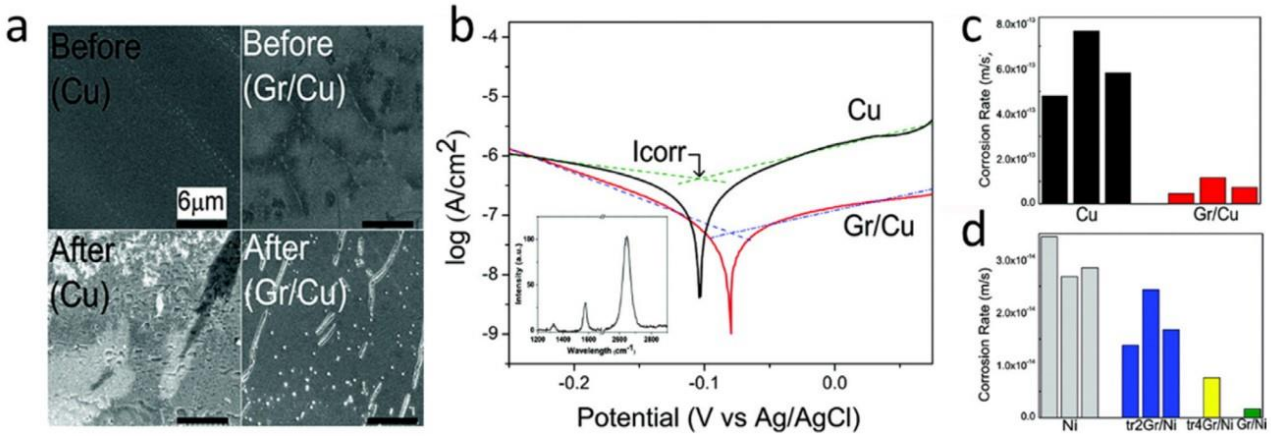

a) Comparison of SEM images of Cu and Gr/Cu before and after corrosion; b) Tafel curve fitting results for Cu and Gr/Cu samples (inset: Gr/Cu Raman spectrum); c) corrosion rates of Cu and Gr/Cu samples extracted from the Tafel plots; d) corrosion rates of Ni, Gr/Ni and graphene coatings transferred to Ni

Figure 8 – Results of corrosion resistance analysis of pure graphene coatings [88]

Directly grown graphene films have many potential advantages compared to transferred graphene films and anticorrosion coatings obtained by conventional methods, such as anticorrosion paints and electro galvanization. Graphene grown in situ, unlike conventional paints, connects to the metal substrate with greater bonding force and avoids the peeling of the film from the metal surface. CVD-grown graphene films are ultrathin and the most effective anticorrosion coatings for underlying metallic materials. The main problems of the CVD method are its limited industrial application and the presence of structural defects, but recently CVD methods have been significantly improved and successfully used to grow high-quality graphene with low defects.

Despite the excellent barrier properties, high chemical and thermal stability of monolayer graphene, the prospects for its use as an anticorrosion protective coating are obscure, because it is quite difficult to grow large defect-free films. A potential solution to this problem is the use of FGNS. GO can serve as a good and attractive alternative to pure graphene coating, since these films can be produced quite easily and inexpensively by applying GO solutions to various substrates by spraying, dipping and other methods. Some studies have shown that GO-based protective coatings have very unusual permeation properties [107-110]. Recently, scientists have made significant efforts to obtain and study FGNS films incorporating thermally reduced GO (T-RGO) [111,112] and graphene-based composites [113] as ultrabarriers for organic electronics and as anticorrosion coatings [113,114-116]. However, T-RGO membranes have disadvantages in the form of its extreme brittleness and content of many structural defects, due to which there is a noticeable water penetration through the membranes [107,113]. GO-polymer composites also have disadvantages, one of which is too high gas permeability, which makes their practical application difficult [113].

Su et al. in his work compared the barrier properties of GO, T-RGO and functionalized graphene films obtained by mild chemical reduction of GO by hydroiodic acid (HI-RGO) and ascorbic acid (VC-RGO) [80]. Recent studies show that the use of hydroiodic acid as a reducing agent leaves fewer structural defects and deformations. In terms of electrical and mechanical properties, the quality of HI-RGO is higher than that provided by other reduction methods [117, 118]. Another interesting reducing agent is ascorbic acid, i.e. vitamin C, which shows good reducing characteristics and it is also non-toxic and environmentally friendly, which can be used in applications with special requirements. [119,120]. In HI-RGO films up to 30 nm thick, no hydrogen and moisture penetration has been detected, while they remain optically transparent. In HI-RGO films over 100 nm thick, no permeability to all of the studied gases and liquids was detected. It was found that the studied HI-RGO and VC-RGO form high-quality barriers and are impervious to strong chemical and salt solutions. These exceptional properties offer close prospects for mass applications of chemically resistant and inert paints as well as flexible RGO-based anticorrosion coatings. Figure 9 shows a comparison of water penetration measurements through freestanding GO, T-RGO, VC-RGO and HI-RGO membranes.

Another representative of the anticorrosion FGNS coatings are composite coatings, where the graphene nanostructures act as a filler. The composite coating from graphene nanostructures combines the strong adhesion and barrier properties of graphene and film-forming properties of the matrix, the role of which is often played by polymers. A key indicator of the degree of shielding protection of composite coatings is the dispersity and orderly arrangement of the graphene in the matrix. The preparation method and process of the anticorrosion composite coating from graphene nanostructures can be based on the traditional production methods, which facilitates the process controllability and can provide manufacturability in industrial applications. Composite coating from graphene nanostructures can be a driving force for anticorrosion coatings in the future, but so far this area remains not well understood.

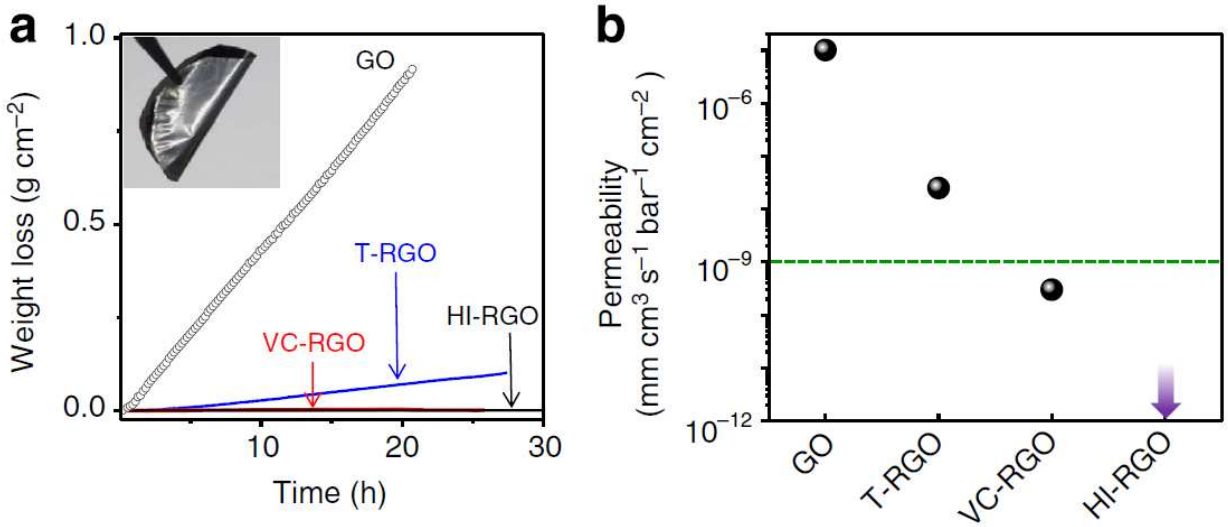

a) water loss from the container sealed with GO, T-RGO, VC-RGO and HI-RGO membranes (inset: photo of HI-RGO membrane); b) permeability of GO, T-RGO, VC-RGO and HI-RGO membranes to moisture (green line shows water permeability value for standard barrier films)

Figure 9 – Water penetration through freestanding multilayer graphene membranes [80]

1.6 Raman spectroscopy of carbon materials

Raman spectroscopy is an efficient, powerful and non-destructive method of spectral analysis to characterize the structure and chemical nature of matter. It is widely used to analyze physical properties such as crystallinity, phase transitions, and to identify polymorphic forms. Provides key information on the structure of molecules, and the analysis can identify chemical components or study intramolecular interactions. The main applications of Raman spectroscopy are materials science (particularly nanomaterials), chemistry, pharmaceuticals, biology

and geology. The types of samples that can be studied by this method include crystals, films, powders and solutions.

The Raman effect is a process of inelastic scattering between incident photons and phonons in materials, known as Raman scattering [121]. During the interaction of incident light photons with vibrational phonons of materials, scattering of light into frequencies occurs and information about the lattice vibrations can be obtained from the difference in frequencies between the incident and scattered light [122]. Therefore, Raman vibrational spectra are widely used in chemistry for the identification of molecules by a structural "fingerprint".

Raman spectroscopy is based on the inelastic scattering process between incident light and the irradiated sample [121]. When the incident light interacts with molecules, the electron cloud is distorted, forming an unstable "virtual level," causing the photons to immediately scatter into another state, which is relatively stable [123]. In the elastic collision process, when photons return to the initial energy level, there is no energy transfer between the incident and scattered light and there is no change in the frequency and wavelength of photons. This elastic collision process is known as Rayleigh scattering [123,124] (Figure 10 (a)). Inelastic light scattering occurs when photons fall to a new energy level, which is different from the initial energy level, as a result of which the photon loses or gains some energy, resulting in a downward or upward energy shift of the laser photons. This energy shift provides information about the oscillations in the system [123]. Inelastic light scattering was theoretically predicted in 1923 by Smekal [125] and was first experimentally discovered in 1928 by Chandrasekhara Venkata Raman [126], so this phenomenon is usually called Raman scattering. There are two types of Raman scattering: Stokes Raman scattering and anti-Stokes Raman scattering. These two types of Raman scattering differ in that in Stokes Raman scattering (Figure 10 (b)) the scattered light holds a lower frequency than the incident light, with energy transferring from light to matter, and in anti-Stokes Raman scattering (Figure 10(c)) the scattered light holds a higher frequency than the incident light, with energy transferring from matter to light.

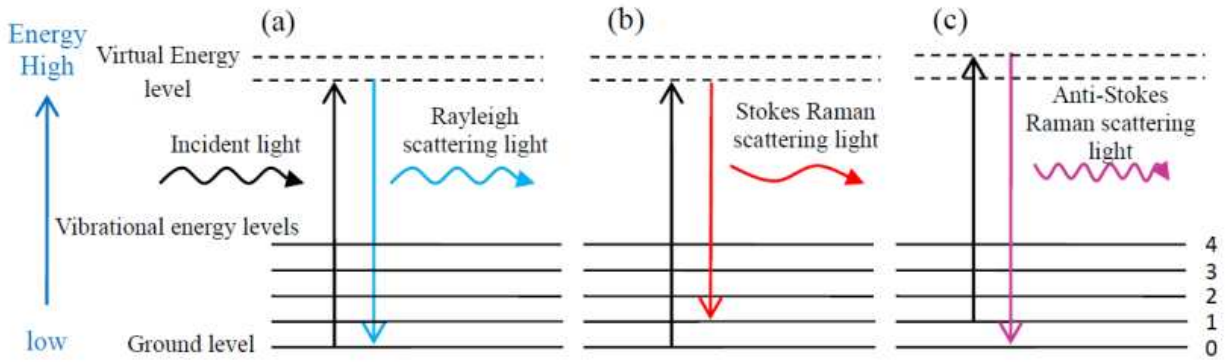

a) Rayleigh scattering; b) Stokes Raman scattering; c) Anti-Stokes Raman scattering

Figure 10 – Illustration of Rayleigh and Raman scattering processes [135]

Thermal equilibrium at room temperature leads to the situation in which the number of molecules is always greater for low-energy vibrations than for high-energy vibrations. The intensity of Stokes light scattering is greater than the intensity of anti-Stokes light scattering, because the number of molecules on the ground level is the highest, so Raman light scattering, for the most part, is Stokes light scattering.

The Raman spectrum shows the dependence of the intensity of scattered light on the wave number (inverse of the wavelength value). The wave number is linearly correlated with the energy of incident and scattered light, so the Raman shift of materials is independent of the wavelength of incident light. The instrument collects scattered light from the material under test and the resulting corresponding spectra contain information on molecular vibrations and crystal structure [127]. Figure 11 shows a typical Raman spectrum and material information. Raman spectroscopy is widely used in various fields of science and technology, such as materials science [128,129], chemical industry [130], environmental monitoring [131], archaeology [132], etc.

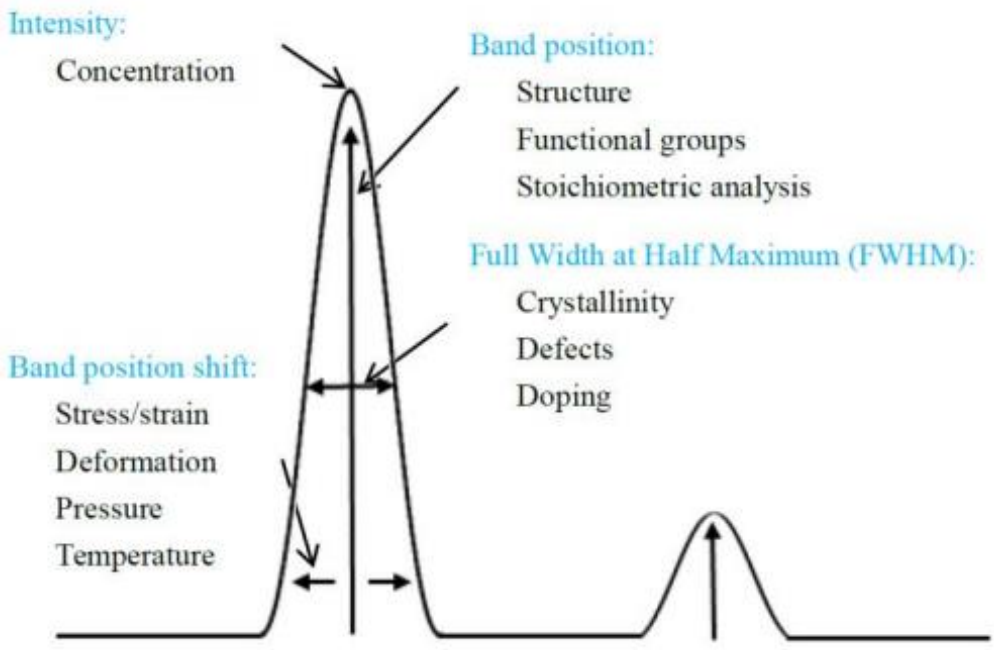

Figure 11 – Typical Raman spectrum and related material information [135]

Allotropic modifications of carbon can serve as the most obvious example of Raman spectroscopy application. Figure 12 shows Raman spectra of such carbon materials as diamond, diamond-like film, graphite, graphene, fullerenes C60 and multi-walled carbon nanotubes. These spectra were obtained at the NNLOT of Al-Farabi KazNU on the NTegra Spectra spectrometer when excited by a laser with a wavelength of 473 nm.

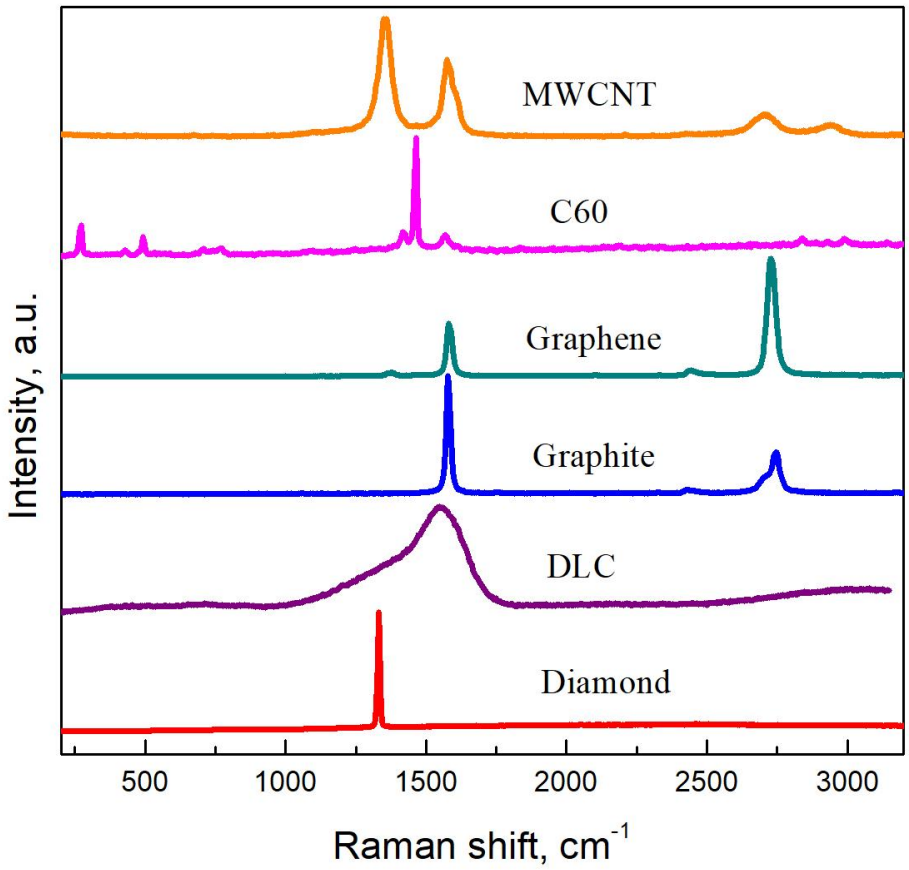

Figure 12 – Typical Raman spectra of carbon materials

As we see from Figure 12, each of the possible allotropic modifications of carbon has its own specific Raman spectrum [133]. When studying anticorrosion coatings based on graphene nanostructures it becomes important to distinguish between the graphite and graphene spectra, so we will dwell on their distinctive features in more detail. Figure 13 (a) shows a typical Raman spectrum of graphite. In the Raman spectrum of monocrystalline hexagonal graphite is manifested an intense line - the G (graphite) line. Line G at a frequency ~ 1580 ± 5 cm^{-1} is proof of the presence of hexagonal graphite layers of sp^2 carbon, and the appearance in the structure of carbon material in a small number (up to 20%) sp^3-bonds leads to a low-frequency shift band G to 1565 cm^{-1}. In Raman spectra of non-ideal graphite single crystals with a hexagonal type of crystal lattice appears an additional line in the region of ~1350 cm^{-1} - the D line (disorder, defects). The broadening of the G line and the increase in the intensity of the D line indicate an increase in defectiveness. In Raman spectra of single-crystal highly ordered graphites the line at ~ 2700 cm^{-1} is observed, which is historically called G', since it is characteristic for any graphite samples along with the G line. However, the G' line has nothing in common with the G line, but is a second-order scattering peak corresponding to the D peak because of this, in modern literature this line in spectra is commonly referred to as 2D [134]. When the exciting beam falls on the graphite plane containing the edges of the graphene planes, the splitting of the D and 2D lines is characteristic. Figure 13 (b)

shows Raman spectra of thin layers of graphene on Si/SiO_2 substrate. These spectra show that the relative intensity of the G line increases and the 2D line slightly widens and shifts to the long wave region of the spectrum with increasing number of graphene layers. Raman spectra of graphene in three or more layers already differ little from each other.

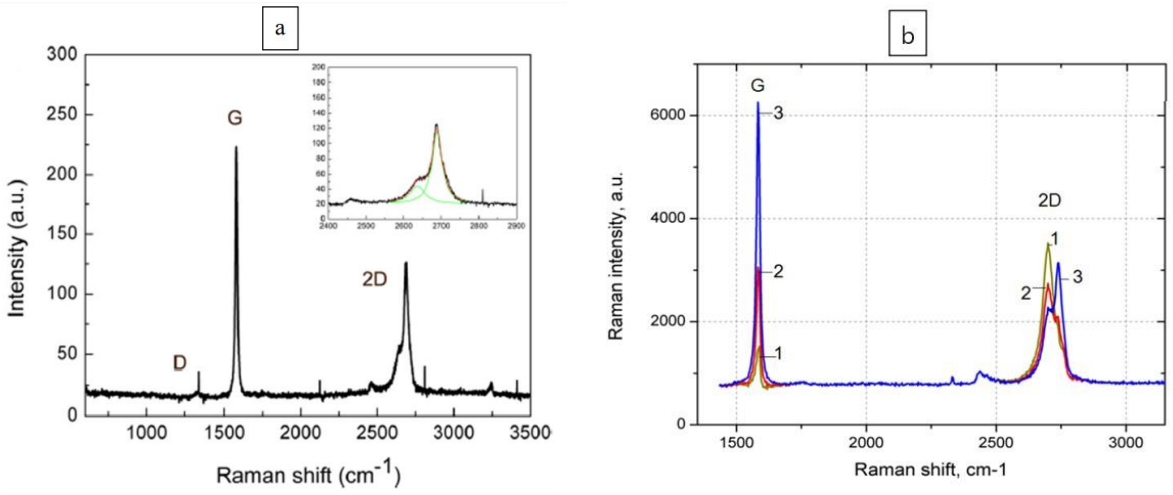

a) graphite; b) dependence of spectra on the number of graphene layers: 1 - monolayer of graphene, 2 - double layer of graphene, 3 - three or more layers

Figure 13 – Typical Raman spectra of graphite and graphene [134]

1.7 Scanning electron microscopy and energy dispersive X-ray spectroscopy

Scanning electron microscopy (SEM) is a common and informative method for microstructural analysis of materials. In this method, electrons accelerated by a high voltage (0-30 kV) are focused on a sample. The surface is scanned by a focused electron beam, during which the electrons and atoms of a material under study interact. Response signals of different physical nature appear when the electrons interact with a material, including primary backscattered electrons, secondary electrons, Auger electrons, X-ray radiation, cathodoluminescence, etc. Figure 14 shows a diagram of the effects of electron beam on a sample in the SEM (Diagram courtesy of Iowa State University) [136]. Although all these signals are present in the SEM, not all of them are detected and used to obtain information. The most commonly used signals are Secondary Electrons, the Backscattered Electrons and X-rays. Detectors collect secondary electrons, backscattered electrons, X-rays and convert them into a signal, which is transmitted to a screen as an image with high (several nanometers) spatial resolution. The image obtained on the screen gives us information about the microstructure and some other properties of the near-surface layers of a sample. In addition, energy dispersive X-ray spectroscopy (EDX, EDRS or EDS) can be used to perform elemental analysis of the sample surface. SEM has advantages over optical microscopes in the form of higher resolution and depth of focus.

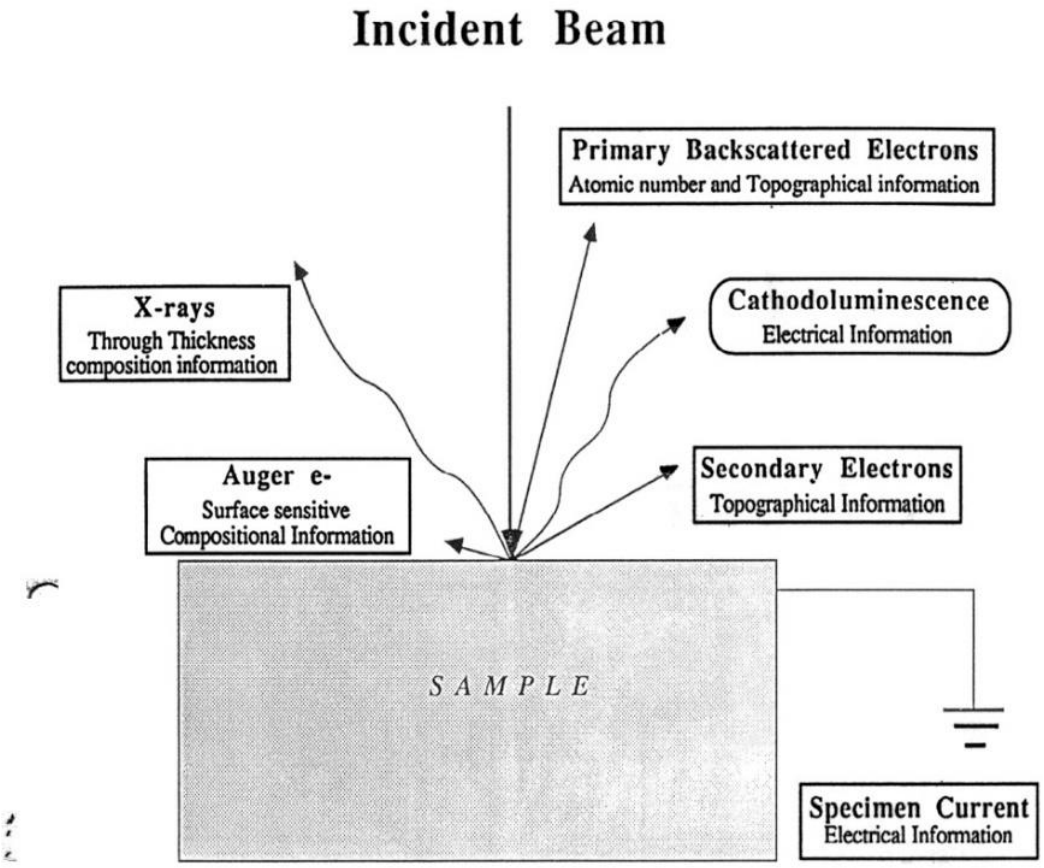

Figure 14 – Diagram of effects of electron beam on a sample [136]

When the electrons hit the surface of a sample target, a number of rather complex phenomena related to the transfer electron energy of beam to the target substance occur. In first approximation, all these phenomena can be divided into two large groups: elastic scattering, associated with changes in electron trajectories with a small loss of energy; inelastic scattering, due to inelastic interactions with atomic nuclei, and inelastic interactions with bound electrons.

The electron penetrates the solid body mainly due to the "inelastic" interaction with the outer electrons of the atom, while the "elastic" interaction with the atomic nucleus determines the spatial distribution. The "secondary", " backscattered " electrons leaving the sample surface are mainly used to form the image. Also, the interaction between the bombarding electrons and the atomic nucleus gives rise to the emission of X-ray photons, exciting a "continuous X-ray spectrum." "Characteristic" X-rays (used for chemical analysis) are excited by electrons during transitions between intra-atomic energy levels, creating electron vacancies on the inner shells of the atom [137]. Figure 15 shows a schematic diagram of the generation of characteristic X-ray radiation.

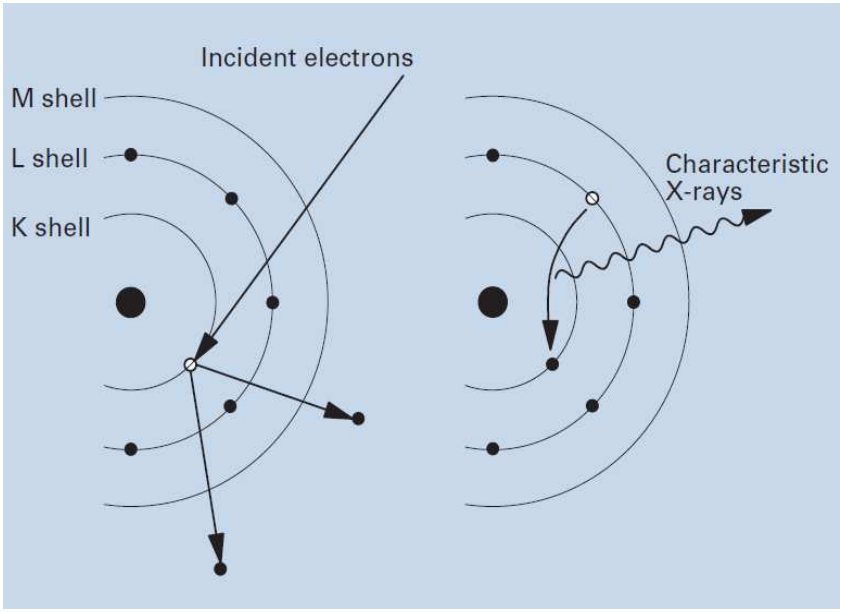

Figure 15 – Principle of characteristic X-ray generation [137]

When electrons from the inner shells are emitted from atoms in matter due to irradiation with outer electrons, the vacant orbits are filled with electrons from the upper shells and the substance emits X-rays, the energy of which corresponds to the energy difference between the upper and inner electron shells. This X-ray radiation is called "characteristic X-ray radiation" because its energy (wavelengths) is a characteristic for each element. Thus, characteristic X-rays are used for elemental analysis. The characteristic X-ray radiation emitted by the excitation of electrons in the K shell is called "K lines," while the radiation emitted by the excitation of the L and M shells is called "L lines" and "M lines," respectively. If the constituent element is heavier, the energy of the characteristic X-ray radiation is correspondingly higher, so high-energy bombarding electrons are required to excite the characteristic X-ray radiation from heavy elements. On the other hand, when bombarding electrons are slowed down by the atomic nucleus, different X-rays are emitted. Such X-rays are called "continuous X-rays" or "white X-rays" or "background X-rays. When X-rays emitted from a sample hit a semiconductor detector, electron-hole pairs are generated, the amount of which corresponds to the energy of the X-rays. Measuring this quantity (electric current) allows us to obtain the value of X-ray energy. The sensor is cooled with liquid nitrogen to reduce the electrical noise. The advantage of EDS is that X-rays from a wide range of elements from B to U are analyzed simultaneously.

1.8 Fundamentals of computer simulation

In the twenty-first century computer modeling has been applied in various fields of science. Natural sciences, social sciences, humanities, life sciences, etc. have somehow or other developed methodologies that use computational tools and, in particular, computer modeling. Current modeling techniques can be roughly divided into material and ideal ones. Material modeling is modeling, which is carried out with the use of a material analogue of the object under study, reproducing basic

geometrical, physical, functional and dynamic characteristics of this object. Material modeling can include the use of models and experimental specimens. Ideal modeling is based not on a material analogy of the object, but on an ideal analogy, i.e. conceivable and always has a theoretical character. As a rule, complex products are created by entire teams of developers, because the more complex and reliable a technical product should be, the more types of models should be applied at the stage of its design.

The essence of computer modeling lies in obtaining quantitative and qualitative results from the available model. The subject of computer modeling can be: technological process, information-computer network, any real object or process in any subject area (physics, chemistry, economics, biology, engineering, etc.).

Computer simulations have advantages over conventional experimental and theoretical physics. Computer simulations can deal with systems that do not exist in reality, thus overcoming the difficulties of experiments. It is possible to construct systems consisting of particles interacting using imaginary model potentials for the sake of revealing the fundamental rules of nature. A wide range of physical properties can be measured in computer simulations, in contrast to real laboratory conditions. For example, based on the available complete information about the positions and velocities of all particles in the simulated system, any desired microscopic physical quantities can be obtained. Also, some extreme limits can be realized in computer models, which cannot be achieved even by the most modern instrumentation. Examples of such extreme limits are extremely high pressures, extremely fast hardening rates, etc. To make real physical systems amenable to theory, it is always necessary to extract essential aspects and build simple models. Very often rigorous solutions are achieved only for oversimplified models, consequently, the physical relevance of the solutions is questionable. For less simple models, on the other hand, problems have to be solved with approximations, but the validity of these approximations is not always guaranteed from a physical point of view. Computer simulation is free from these difficulties, since exact solutions are obtained even for complex systems without approximations. As a result, it is possible to study models that are much closer to realistic materials. It should be noted that computer simulations are performed only for systems of finite size for a limited observation time. Methods that minimize the impact of these limitations must be developed in realistic simulation processes.

The task of computer simulation of nanosystems is extremely complicated and laborious, because at the molecular level the traditional macroscopic laws of physics, mechanics, resistance of materials, hydraulics, etc. are no longer valid. Instead, quantum laws come into play, which lead to results completely unexpected from the point of view of classical notions. If we try to identify the main numerical methods for systems containing a large number of particles, they can be summarized in the following four: quantum-theoretical calculations "from first principles" [138], molecular mechanics, molecular dynamics [139] and Monte Carlo methods [140]. Each of these four calculation methods has its own advantages and limitations. Calculation results should reflect reality as closely as possible.

Since it is not possible to solve the quantum Schrödinger equation for a system of many particles, the quantum-theoretic approach consists in finding reasonable approximations and possibilities for separating variables, allowing to simplify the calculation scheme without involving experimental data. The most common methods of calculations "from first principles" are self-consistent field models (Hartree–Fock method), linear combination of atomic and molecular orbitals, density functional theories, potential energy surface, etc. Calculations "from first principles" without additional a priori assumptions regarding the interaction potentials of particles take into account various quantum effects. However, due to enormous computational difficulties, it is possible to consider only systems containing not more than a few hundred atoms. Nevertheless, such methods have stimulated the accelerated development of chemistry, allowed the computer calculation of molecules, and promoted the creation of semiempirical methods for the calculation of large molecular systems. Density functional theory (DFT) is a quantum mechanical method for calculating the electronic structure of atoms, molecules and solids. In this way, larger (and often more significant) molecular systems can be studied with sufficient accuracy, thereby extending the predictive power inherent in electronic structure theory. Because of this, DFT is currently the most widely used electronic structure method. The enormous importance of DFT in computational modeling is evidenced by the award of the 1998 Nobel Prize to Walter Kohn for the development of density functional theory [141].

The methods of molecular mechanics and molecular dynamics are based on classical physics of systems of many particles and cannot describe quantum effects. Moreover, these methods require detailed knowledge of inter-particle interactions to obtain numerical results, so different models must be used in each individual case. Quantum mechanics is introduced in this case in an implicit way (using interaction potentials obtained, for example, by calculations "from first principles"). To obtain realistic results in most cases additional fitting of these potentials to experimental data is required. Thus, the ambiguity of the interaction potentials used in molecular mechanics and molecular dynamics limits the wide application of these methods. At the same time, they make it possible to consider large nanosystems containing 10^5–10^7 atoms, depending on the study. The goal of molecular mechanics (as well as of "first principles" calculations) is to find stable configurations for systems of many particles, i.e. to determine saddle points (local minima) on the potential energy surface. However, in contrast to calculations "from first principles," methods of molecular mechanics and molecular dynamics are based on classical notions. Particles are considered in these cases as material points interacting through force fields, which, in turn, are determined by interaction potentials. While in quantum mechanical calculations the concept of chemical bonds is absent a priori, the methods of molecular mechanics select interaction potentials, as well as energy and parameters corresponding to certain local configurations of atoms, depending on the type of bonds. However, the methods of molecular mechanics can be successfully applied only to a relatively narrow class of molecular structures in configurations close to the equilibrium state. The methods of molecular dynamics make it possible

to solve the Newtonian equations of motion of particles. In this regard, the evolution of a system of many particles over a certain number of time steps can be calculated, and at each step information about the position of particles, their velocity, kinetic and potential energy, etc., is available. All thermodynamic characteristics of the system can be determined without using any additional parameters.

The most common method of stochastic simulation is the Monte Carlo method, a general name for a group of numerical methods that are widely used in statistical physics, where different variants of the system configuration that form a statistical ensemble are randomly generated. The term "Monte Carlo" was a reference to the gambling town of Monaco and was first introduced by Ulam and von Neumann [142]. Using Monte Carlo methods, the entire statistical totality of the energy states of atoms in a molecule is examined, which makes it possible to determine the most favorable spatial structure of molecules in terms of energy, as well as to estimate their thermodynamic characteristics. The Monte Carlo method can be applied to assess the uncertainty of financial forecasts, the results of investment projects, when forecasting the cost and schedule of project implementation, business process disruptions and personnel replacement. This method is used in situations where results cannot be obtained by analytical methods or there is high uncertainty of input or output data.

Computer simulation in this dissertation was performed using DMol3. DMol3 is a commercial (and academic) software package that uses density functional theory with a basis of numerical radial functions to calculate the electronic properties of molecules, clusters, surfaces and crystalline solid materials from first principles. DMol3 allows optimizing the geometry and searching for saddle points with and without geometric constraints, as well as calculating various derivative properties of the electronic configuration [143].

Hohenberg and Kohn [230] introduced the density functional theory (DFT) in 1964. Let an arbitrary number of electrons in a box be subject to an external potential $v(\mathbf{r})$ and the electron-electron Coulomb repulsion, then, this potential is a unique functional of the electron density $n(\mathbf{r})$, except for an additive constant [231]. Expressions or equations for the potential, the density, and functionals in bold indicate that the position variable is a vector. The Hamiltonian of the system is written as

$$H = T + U + V \tag{4}$$

where T and U are for the kinetic energy and electron-electron interaction operators, with

$$V = \int v(\mathbf{r})\psi^*(\mathbf{r})\psi(\mathbf{r})d\mathrm{r} \tag{5}$$

Sum of the kinetic and electron-electron interaction energies is a universal functional of the charge density, since Ψ is a functional of $n(\mathbf{r})$:

$$F\,[n(\mathbf{r})] \equiv (\Psi, (T + U)\,\Psi) \tag{6}$$

It followed from the above results that, for a given potential $v(\mathbf{r})$, we have the energy functional

$$E_v[n] = \int v(\mathbf{r})n(\mathbf{r})d\mathbf{r} + F[n] \tag{7}$$

Hohenberg and Kohn proceeded to establish that this unique functional of the density attains its minimum (from above) for the correct ground state density $n(\boldsymbol{r})$, provided the total number of particles,

$$N[n] \equiv \int n(\mathbf{r})d\mathbf{r} = N \tag{8}$$

is kept constant. Specifically, the actual quote from the Hohenberg and Kohn article follows. "It is well known that for a system of N particles, the energy functional of Ψ'

$$E_v[\Psi'] = (\Psi', V\Psi') + (\Psi', (T+U)\Psi') \tag{9}$$

has a minimum at the 'correct' ground state Ψ, relative to arbitrary variations of Ψ' in which the total number of particles is kept constant."

The authors took the next crucial step consisting of showing that a density $n'(\boldsymbol{r})$, associated with a another potential $v'(\boldsymbol{r})$ [different from $v(\mathbf{r})$], leads to a minimum value of the above energy functional that is higher than the one obtained with the ground state density $n(\mathbf{r})$ of the system.

Specifically, they established the following inequality:

$$\int v(\mathbf{r})n'(\mathbf{r})d\mathbf{r} + F[n'] > \int v(\mathbf{r})n(\mathbf{r})d\mathbf{r} + F[n] \tag{10}$$

It should be noted that the potential $v(\mathbf{r})$ is used on both sides of the inequality. This result is generally referred to as the second Hohenberg and Kohn theorem or as the DFT variational principle.

Kohn and Sham [232] introduced the local density approximation (LDA) of DFT in 1965. These authors rewrote the energy functional in Equations (7) and (9) as

$$E = \int v(\boldsymbol{r})n(\boldsymbol{r})d\boldsymbol{r} + \frac{1}{2}\iint \frac{n(\boldsymbol{r})n(\boldsymbol{r}')}{|\boldsymbol{r}-\boldsymbol{r}'|}d\boldsymbol{r}d\boldsymbol{r}' + T_s[n] + E_{xc}[n], \tag{11}$$

where $T_s[n]$ is the kinetic energy of a system of non-interacting electrons whose density is $n(\boldsymbol{r})$, while $E_{xc}[n]$ is defined as the exchange correlation energy of a system of interacting electrons with the same density $n(\boldsymbol{r})$. In the case of slowly varying densities, Kohn and Sham obtained an expression for $E_{xc}[n]$ in terms of the exchange correlation energy per electron of a uniform gas whose density is n.

$$E_{xc}[n] = \int n(\boldsymbol{r}) \in_{xc} (n(\boldsymbol{r}))\, d\boldsymbol{r}, \tag{12}$$

where $\in_{xc}(n(\boldsymbol{r}))$ is the exchange and correlation energy per electron of a uniform electron gas of density n. The next pivotal step taken by these authors consisted of using the stationary property of Equation (11) (i.e., a particular form of Equation (9)) to derive an equation that straightforwardly leads to the Kohn Sham (KS) equation,

$$\{-\frac{1}{2}\nabla^2 + [v(\boldsymbol{r}) + \int \frac{n(\boldsymbol{r}')}{|\boldsymbol{r}-\boldsymbol{r}|}d\boldsymbol{r}' + \mu_{xc}(n(\boldsymbol{r}))]\}\ \psi_i(\boldsymbol{r}) = \in_i \psi_i(\boldsymbol{r}), \tag{13}$$

with the charge density computed using only the wave functions of the occupied states as

$$n(\boldsymbol{r}) = \sum_{i=1}^{N} |\psi_i(\boldsymbol{r})|^2. \tag{14}$$

The referenced derivation of the Kohn Sham equation requires that the total number of particles (N) be kept constant. Interestingly enough, Equation (14) is sufficient to underscore the fact that N must be constant. Any change in N means a totally new density and hence new values for all quantities that are unique functionals of the density! The above KS equation describes a system of non interacting electrons moving in the potential between brackets in Equation 13. The exchange correlation contribution to the chemical potential of a uniform gas of density n is $\mu_{xc}(n(\boldsymbol{r}))$.

Conclusions for section 1

Corrosion is a vast problem that we also encounter in everyday life. Corrosion of metals such as copper, nickel, carbon steel and magnesium affects industrial production, which in turn leads to enormous economic losses. The solution to this problem are anticorrosion coatings that can insulate the base metal from aggressive media, thereby reducing the risk of corrosion. In recent years, graphene coatings for the protection of metals against oxidation and corrosion have become widespread due to the properties of strength, impermeability, chemical inertness and hydrophobicity. Graphene is an ultrathin coating and its anticorrosion effect is superior to the traditional anticorrosion coatings without changing the original thermal/electrical conductivity of the substrate. However, the prospects for its use as an anticorrosion protective coating are murky because it is difficult to grow large defect-free films. A possible solution to this problem is the use of FGNS, a prominent representative of which is GO. GO can serve as a good and attractive alternative to the coating of pure graphene, as these films can be obtained quite simply and inexpensively by applying GO solutions to various substrates by spraying, dipping and other methods.

Raman spectroscopy is an effective, powerful and non-destructive method of spectral analysis for characterizing the structure and chemical nature of matter. The most striking example of Raman spectroscopy application is the allotropic modifications of carbon. Each of the possible allotropic modifications of carbon has its own specific Raman spectrum. When studying anticorrosion coatings based on graphene nanostructures it becomes important to distinguish between graphite and graphene spectra. Scanning electron microscopy (SEM) is a common and informative method of microstructural analysis of materials. SEM images give us information

about the microstructure and some other properties of the near-surface layers of the sample. Energy dispersive X-ray spectroscopy (EDX, EDRS or EDS) is used to perform elemental analysis of the sample surface.

Computer simulation has advantages over conventional experimental and theoretical physics. Computer simulation can deal with systems that do not exist in reality, thus overcoming the difficulties of experiments. A wide range of physical properties can be measured by computer simulation, unlike real laboratory conditions. Computer simulation in this thesis was performed using DMol3.

2 COMPUTER SIMULATION

2.1 Computer simulation and calculations of the protective properties of graphene against oxygen penetration

To theoretically confirm the effectiveness of the protective action of graphene against metal corrosion, two main possibilities for oxygen penetration into the area of the copper surface covered by graphene were simulated: directly through the graphene and through the gap between the substrate and the graphene. Bunch et al. [144] reported that monolayer graphene is practically impermeable to standard gases, including even helium. Nevertheless, this variant was modeled. Computer simulations of the investigated nanostructures were performed using the DMol3 software package, which uses density functional theory (DFT). The DFT method has proven to be an effective tool in previously published works for the description of the energy and structural characteristics of graphene nanostructures, including functionalized ones [145-149]. The calculations showed that for the oxygen molecule penetration directly through the graphene, the energy barrier is very high even for the most favorable orientation of the molecule - when the axis is perpendicular to the graphene plane and passes through the hexagon center (Figure 16). For the other orientations the barrier is even higher.

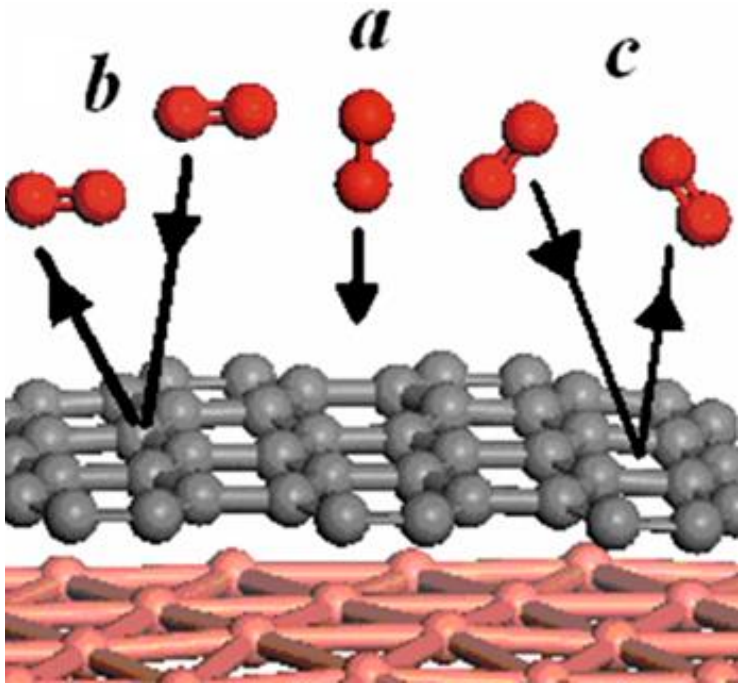

Figure 16 – Computer simulation of O_2 molecule passing directly through graphene. Energy barriers for different orientations of the molecule (E): a) 34.3 eV; b) 40 eV; c) 38 eV

For the possibility of oxygen penetration through the gap between the substrate and graphene two basic orientations of the oxygen molecule when entering the gap were considered: the axis of the molecule is parallel to the graphene edge, the axis of

the molecule is perpendicular to the graphene edge. Computer simulation and calculations showed the potential barrier for the molecule entry in the graphene-substrate gap region (Figure 17). It is shown that the value of the barrier for the entry of the O_2 molecule into the space between the graphene and the substrate strongly depends on the orientation of the molecule. It is approximately two times smaller for the orientation in which the axis of the molecule is perpendicular to the graphene edge. Nevertheless, even in this case the probability of oxygen penetration into the zone closed by graphene is negligible.

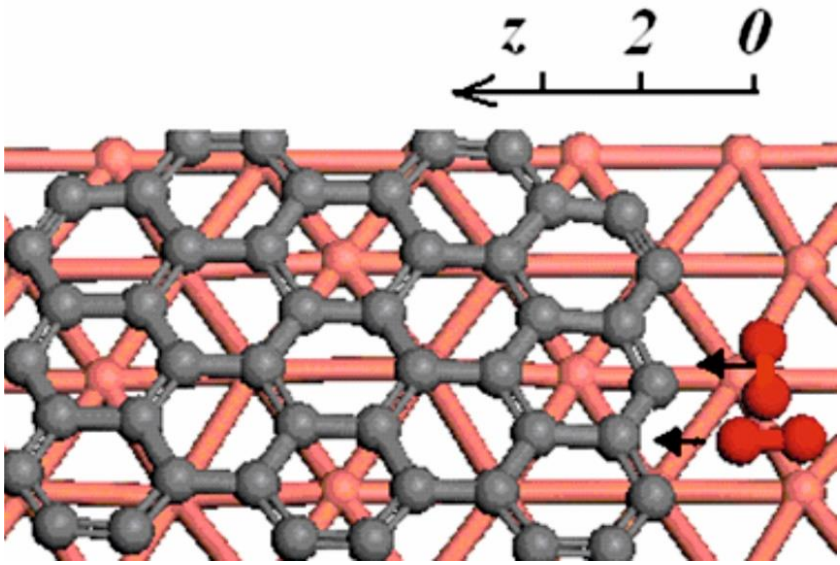

Figure 17 – Computer models of the two main types of orientation of the O_2 molecule

The results of calculations of the energy barrier (ΔE) dependence on the distance (Z) through the gap between the substrate and graphene for two basic types of orientation, when the axis of the O_2 molecule is parallel to the graphene edge and when the axis of the O_2 molecule is perpendicular to the graphene edge are presented in Table 1.

Table 1 – Dependence of (ΔE) on (Z) when oxygen penetrates through the gap between the substrate and graphene

Z, Å	ΔE, eV	
	the axis of the O_2 molecule is parallel to the graphene edge	the axis of the O_2 molecule is perpendicular to the graphene edge
0	0	0
0.5	1.5	
1.0	4.1	4.2
2.0	14.6	6.9
3.0	11.6	5.6
3.5	11.4	5.5

2.2 Computer simulation and calculations of the effectiveness of the protective graphene coating containing defects

Graphene has excellent barrier properties, but in practice it is almost impossible to obtain perfect defect-free graphene. When graphene is synthesized on the surface of the protected metal or when applied to it ready grown graphene particles, these materials usually contain structural defects, such as vacancies or their complexes, discontinuities in the structure and gaps between the sheets of graphene nanoparticles [150]. Despite intensive research, this problem related to the question of the effectiveness of protective coatings containing defects has not been studied enough. Theoretical studies of the protective properties of the graphene coating containing structural defects (vacancies and vacancy complexes) and discontinuities (breaks between graphene sheets) from oxygen penetration were carried out in this part of the work. For a more detailed study and prediction of the properties of the studied nanostructures, computer models were created and quantum-mechanical numerical calculations were performed using the well-proven DFT method and the optimization procedure built into the DMol3 package, widely used by researchers in nanomaterials physics, which has proven its reliability and high efficiency.

In Figure 18 was used a model gap in the coating between two graphene sheets, which had a width of 0.25 nm when the sheets were arranged in the same plane. Figure 19 shows the computer models used to calculate the energy characteristics of the configurations of oxygen (O_2) molecules approaching the gap in the coating (in the plane passing through the center of the gap).

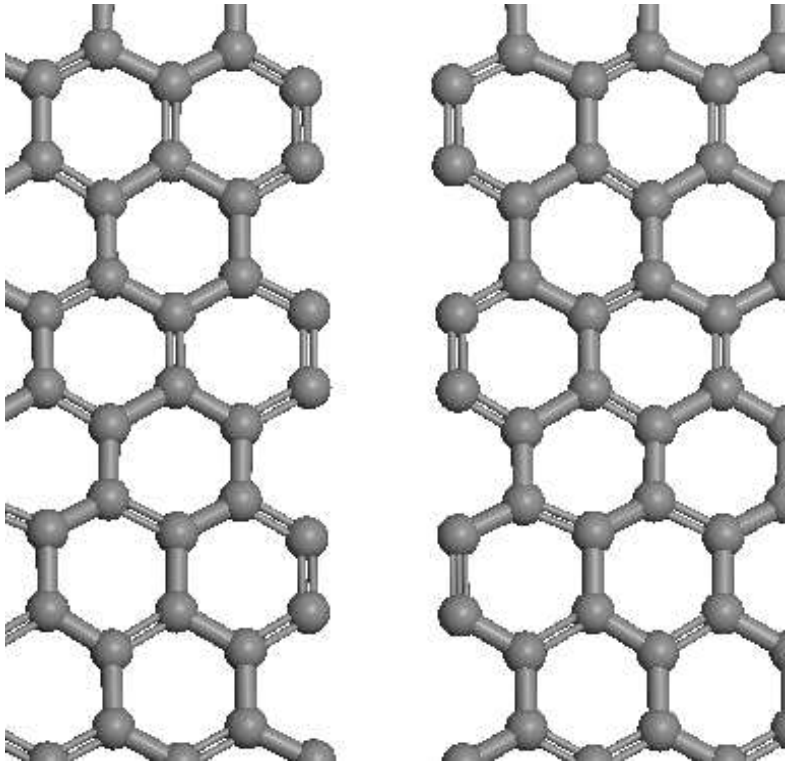

Figure 18 – Model of the gap between two graphene sheets in the coating

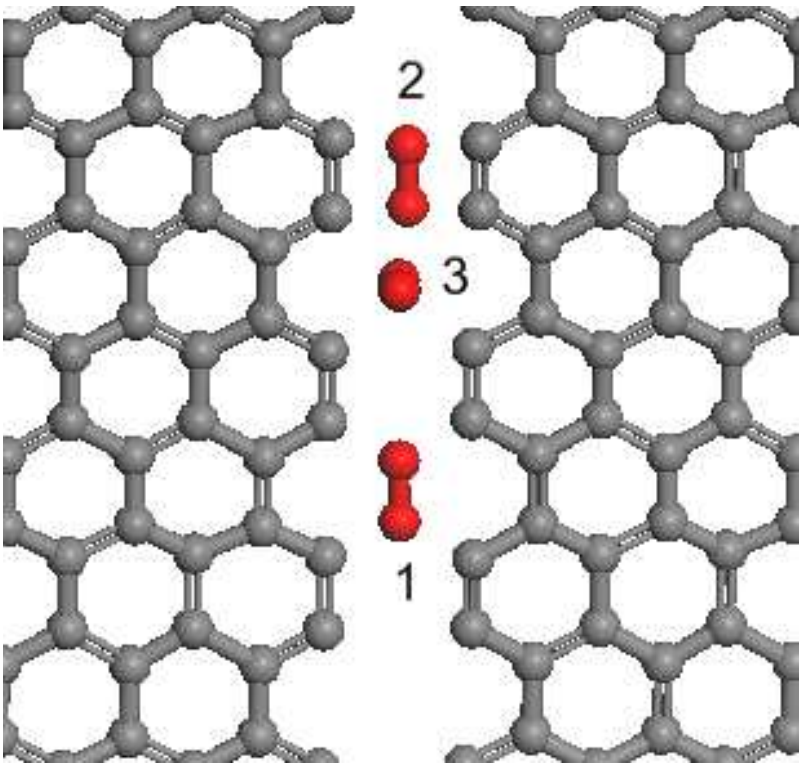

Figure 19 – Computer models of O_2 molecules approaching the gap in the coating. (1) and (2) - O_2 molecule is parallel to the graphene plane; (3) - molecule axis is perpendicular to the graphene plane

Figure 20 presents the electron charge distribution at a density of 10 electrons/nm^3. This density roughly corresponds to the characteristics of the electrons in the conduction band. It is clearly seen that at this density of electrons the gap is almost covered by the electron cloud, which suggests that there is no noticeable effect of deterioration of conductivity properties in the protective coating.

The calculation results in Figure 21 (a, b) show that in this configuration oxygen does not penetrate through the gap in the graphene coating to the protected surface. Figure 21 (b) clearly shows the presence of electronic bridges between the molecule and the edges of the gap. This indicates the formation of a strong bond (the molecule is blocked in the gap). Additionally, a strong covalent bond is formed as a result of chemisorption of oxygen molecules on the edges of the graphene sheets, which helps to prevent further penetration of oxygen molecules through the gap to the protected surface.

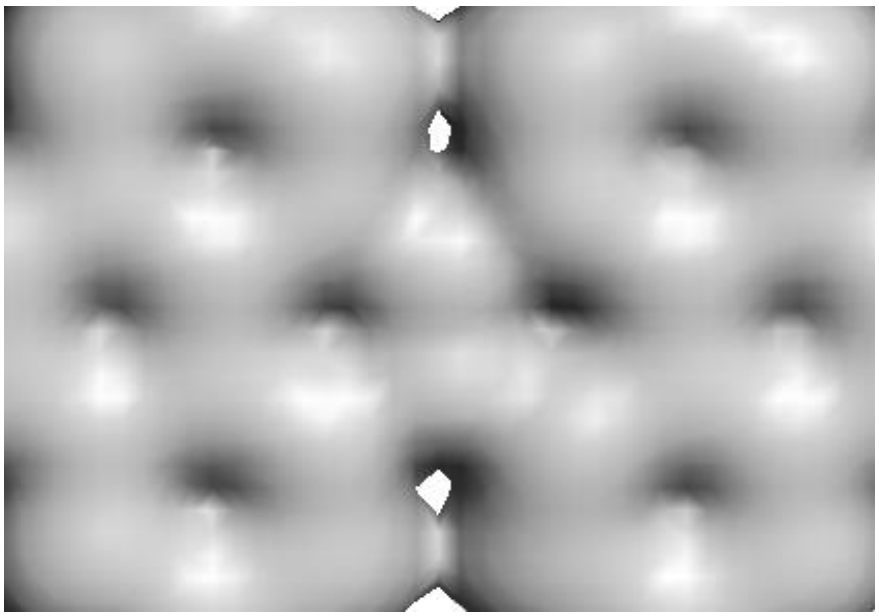

Figure 20 – Calculated electron charge distribution in the region of the gap at a density of 10 electrons/nm^3

The data in Table 2 show that in Configuration 1(figure 19) there is a potential well that captures the molecule at a distance of 0.1 nm before the gap, then a potential barrier that prevents penetration into the slit plane. Configuration 2 (figure 19) shows a high (5 eV) potential barrier at 0.1 nm. Configuration 3 (figure 19) shows the appearance of a potential well in front of the slit and a potential barrier in the graphene plane. These factors indicate the possibility of protection even in the presence of gaps between graphene nanostructures, which can exist in the real situation during the formation of protective coatings based on graphene nanostructures.

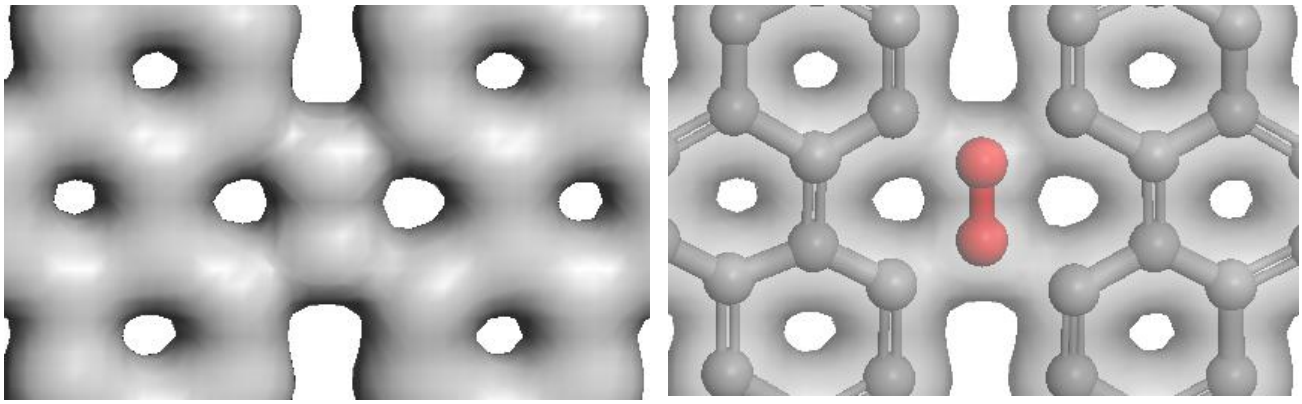

a) b)

Figure 21 – a) Calculated electron charge distribution in the gap region for a charge density of 30 electrons/nm^3, which corresponds to the electrons forming chemical bonds; b) Modified image of the electron charge distribution in the gap region

Table 2 – Calculation of energy characteristics of configurations of oxygen molecules approaching the gap in the coating

Configuration	Distance of the molecule from the plane	Configuration energy
1	2.5	0
	2.0	-1.1
	1.0	-1.7
	0	-1.1
2	2.5	-8
	2	-7
	1	-3
	0	+1
3	0 (center of the bond)	-1
	1.5	-1.65
	2.5	-1.16
	3.5	-1.15

When studying the influence of structural defects on the anticorrosion properties of graphene, computer simulation of graphene containing vacancy (GV) and graphene containing divacancy (GDV) was carried out and potential energy barriers were calculated when O_2 passes through the center of the defective region in graphene. When the O_2 molecule penetrates through graphene, two basic types of molecule orientation were considered, when the axis of the O_2 molecule is perpendicular to the graphene plane (Configuration A) and when the axis of the O_2 molecule is parallel to the graphene plane (Configuration B). Figure 22 (a) shows a computer model of GV-O_2 for Configuration A, Figure 22 (b) shows a computer model of GV-O_2 for Configuration B.

Computer simulation and calculations showed the presence of a high energy barrier when the O_2 molecule penetrates through graphene containing defects. The results of calculations of the energy barrier dependence on the orientation of the O_2 molecule, when the O_2 molecule penetrates through defects in graphene, are presented in Table 3. It was found that the value of the energy barrier strongly depends on the orientation of the O_2 molecule. Figure 23 (a) shows the computer models of GDV-O_2 and Figure 23 (b) shows the computer models of GV-O_2.

Table 3 – Dependence of the energy barrier on the orientation of the oxygen molecule when penetrating through defects in graphene

Configuration	ΔE, eV	
	the axis of the O_2 molecule is perpendicular to the graphene plane	the axis of the O_2 molecule is parallel to the graphene plane
GV	5.5	9
GDV	4.1	7

a) b)

a) The axis of the O_2 molecule is perpendicular to the graphene plane; b) The axis of the O_2 molecule is parallel to the graphene plane

Figure 22 – Computer models of the two basic types of orientation of the molecule during the passage of the O_2 molecule through the GV

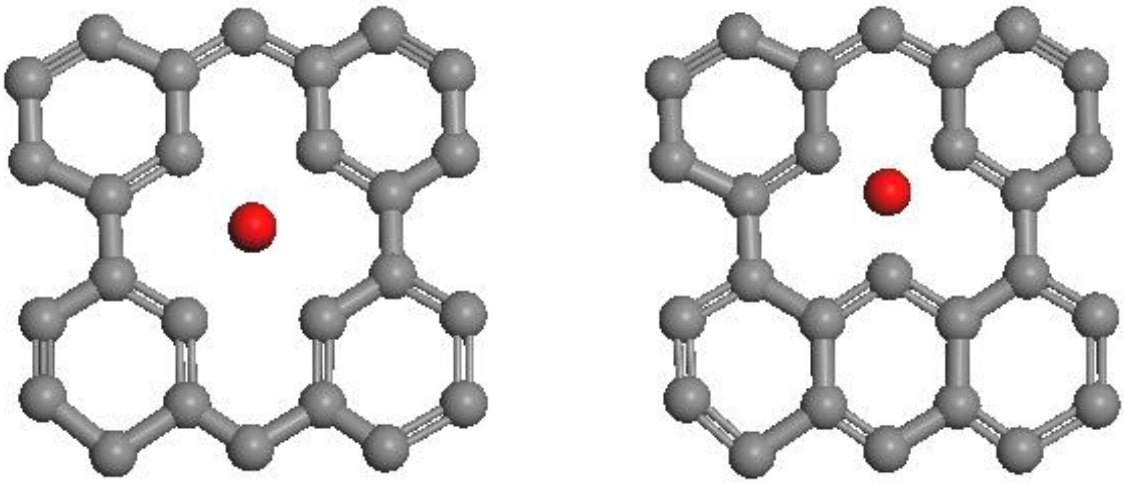

a) GDV-O_2 b) GV-O_2

Figure 23 – Computer models of the passage of the O_2 molecule through defects in graphene

2.3 Computer simulation and calculations of the effectiveness of anticorrosion graphene coating functionalized with gallium

There are a sufficient number of scientific works on anticorrosion graphene coatings, in which graphene is doped with elements of the third and fifth groups, such as boron and nitrogen [227, 228], while doping with gallium has not been studied enough. Based on quantum-mechanical numerical calculations, the functionalization with gallium atoms contributes to the preservation of the high efficiency of the protective effect of the graphene coating, which has a sufficiently large gap (0.45 nm), against oxygen penetration.

All calculations were performed using the DFT method and the energy optimization procedure for structures. Figure 24 shows a computer model of the cluster of 4 gallium atoms that emerged after adsorption on the graphene surface. The cluster's binding energy with graphene is 1.35 eV, and the equilibrium distance from graphene is 0.3 nm. The distance between the gallium atoms in the cluster is approximately 0.27 - 0.3 nm.

The results of the simulations and calculations presented in Figure 25 and 26 show that the bonding of the cluster with the ideal graphene is not strong enough, which is confirmed by the absence of dense electronic bridges between the cluster and graphene at the maximum charge density corresponding to the formation of bonds. Figure 27 shows density of states of the calculated cluster configuration on the graphene protective coating. Figure 28 shows modified image of the possible stable structure of a graphene protective coating element with a gallium cluster with an adsorbed oxygen molecule.

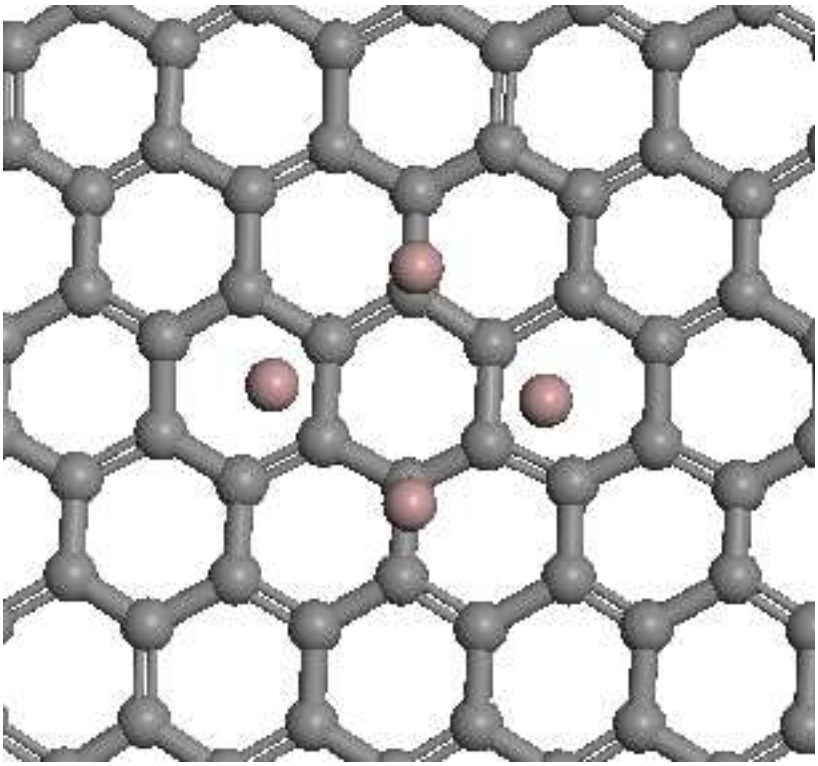

Figure 24 – Computer model of the graphene - 4 Ga system

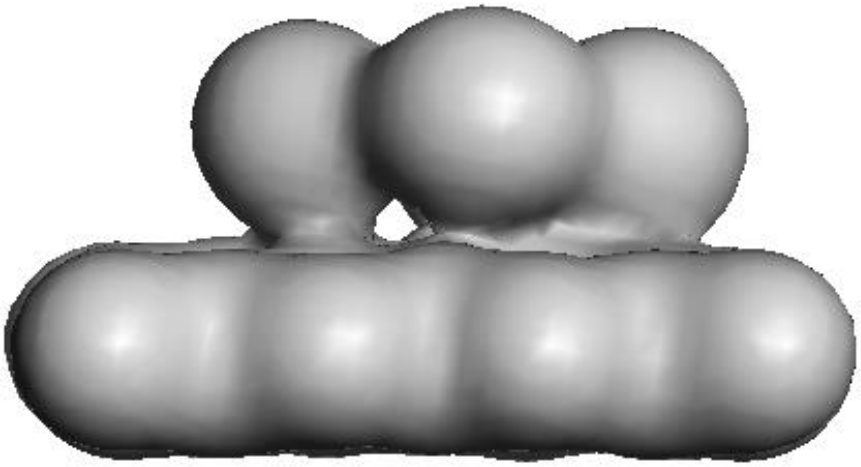

Figure 25 – Electron charge distribution in the graphene - 4 Ga system at a density of 10 el/nm^3

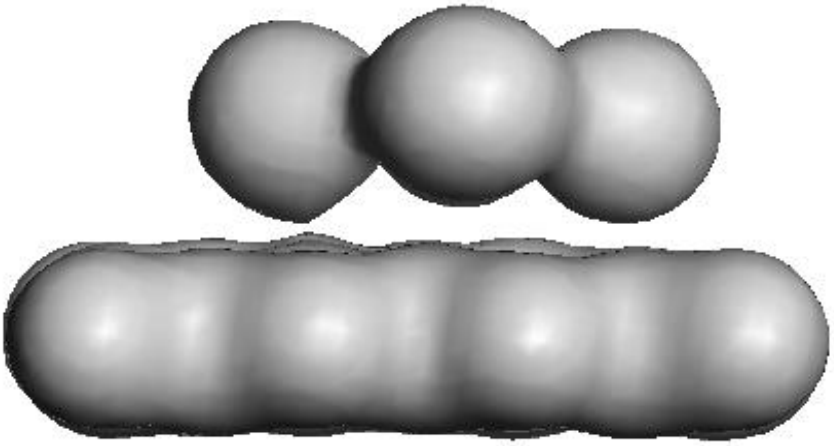

Figure 26 – Electron charge distribution in the graphene - 4 Ga system at a density of 30 el/nm^3

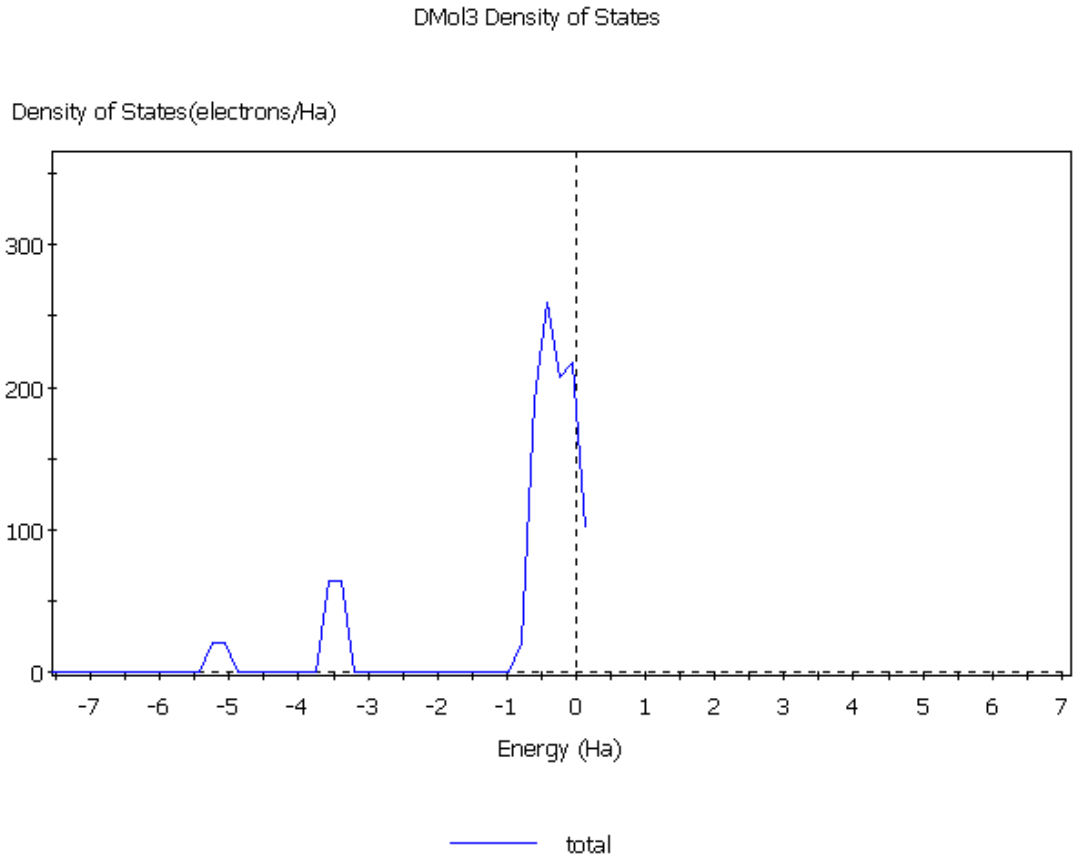

Figure 27 – DOS of the calculated cluster configuration on the graphene protective coating

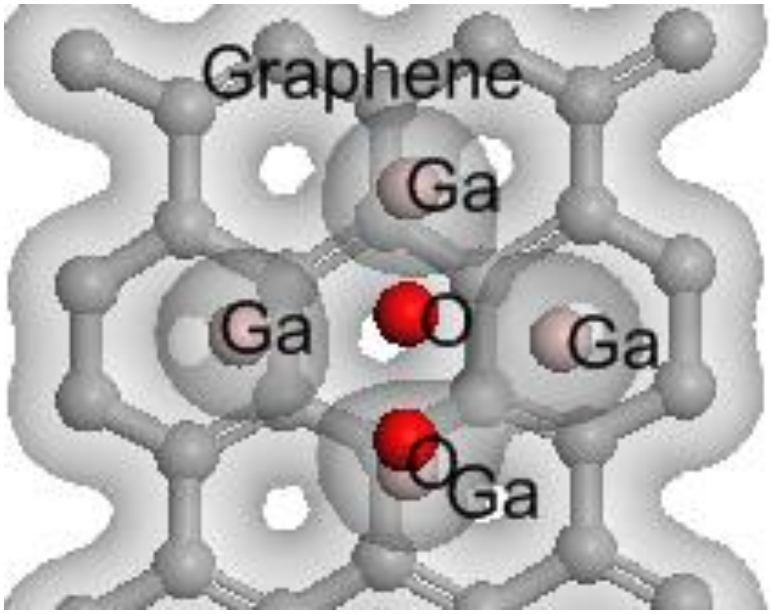

Figure 28 – Possible stable structure of a graphene protective coating element with a gallium cluster with an adsorbed oxygen molecule

In this part of the work, the possibility of maintaining the effectiveness of the protective coating in the presence of a sufficiently large gap in the graphene sheet with a size of 0.45 nm was investigated. The linear structure of Ga atoms is used as blocking elements. Figure 29 illustrates the initial placement of Ga atoms in the gap plane. Subsequently, the calculations used the structures optimization procedure to determine the energy-optimal configuration of the linear structure. After optimization, the linearity of the gallium atom chain was preserved, and the distance between them turned out to be 0.49 nm.

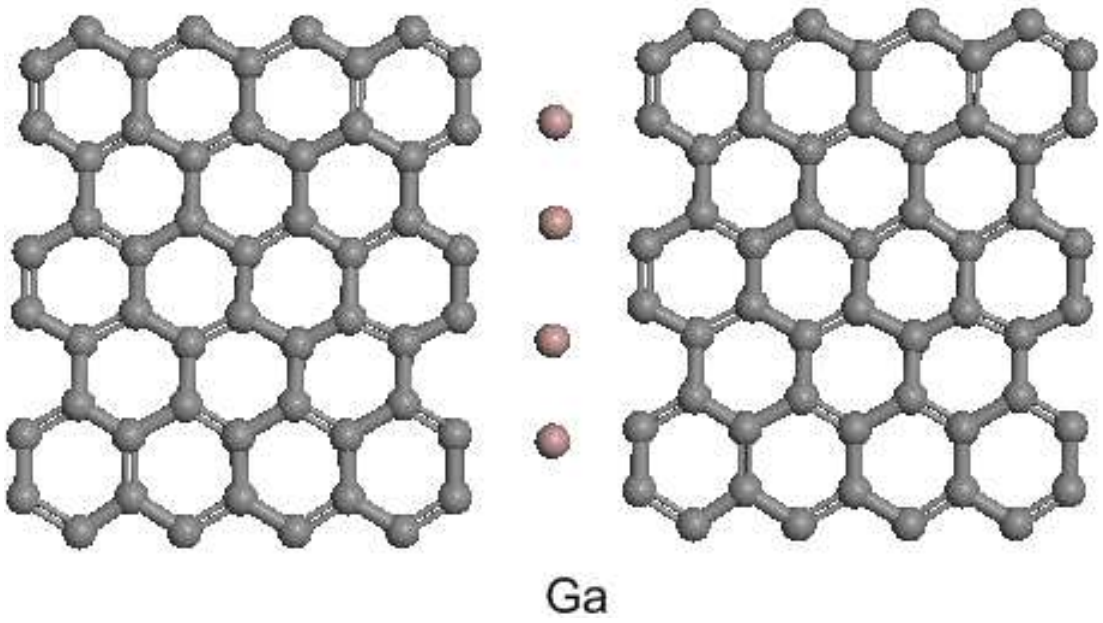

Figure 29 – Linear structure of Ga atoms in the gap plane of the graphene sheet with a size of 0.45 nm. Ga atoms are placed along the midline

Figure 30 and 31 illustrate the results of calculations of the electron charge distribution with configuration optimization for the emerged linear structure of gallium atoms connected with the edges of the graphene protective coatings. It is clearly seen that between the Ga atoms and the graphene sheets at high charge density (density 30 el/nm^3) the electronic bridges appeared, indicating the formation of covalent bonds. The picture of the electron charge distribution shows the preferential transfer to the gallium atoms, which is generally corresponds to the known data on the electron affinity. Ga atoms are in the gap plane at a distance of 0.5 nm between them. The binding energy of the Ga-graphene atoms is 2.6 eV. The atomic structure of the configuration after calculation and application of the optimization procedure is shown. Ga atoms are in the gap plane at a distance of 0.5 nm between them. The width of the gap is 0.45 nm. After calculation and optimization, the oxygen molecule is located at a distance of 0.24 nm from the gap plane. The binding energy of the Ga-graphene atom is 2.6 eV. The calculation gave a rather high value of 1.8 eV for the oxygen adsorption energy. The presented results

indicate the possibility of effective blocking of the gap type defect in the graphene protective coating using the functionalization by gallium atoms. Figure 32 shows computer model of the configuration that occurs when an oxygen molecule adsorbs on a linear structure of Ga atoms.

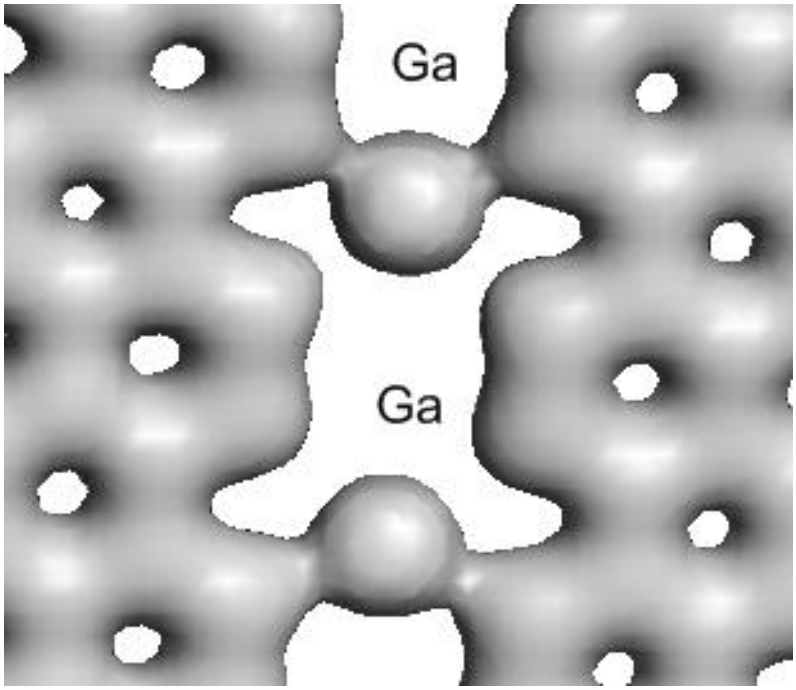

Figure 30 – Electron charge distribution (density 30 el/nm^3) in the gap zone containing Ga atoms. The gap between the graphenes is 0.45 nm. Ga atoms are placed along the midline and connected with the edges of the graphene sheets

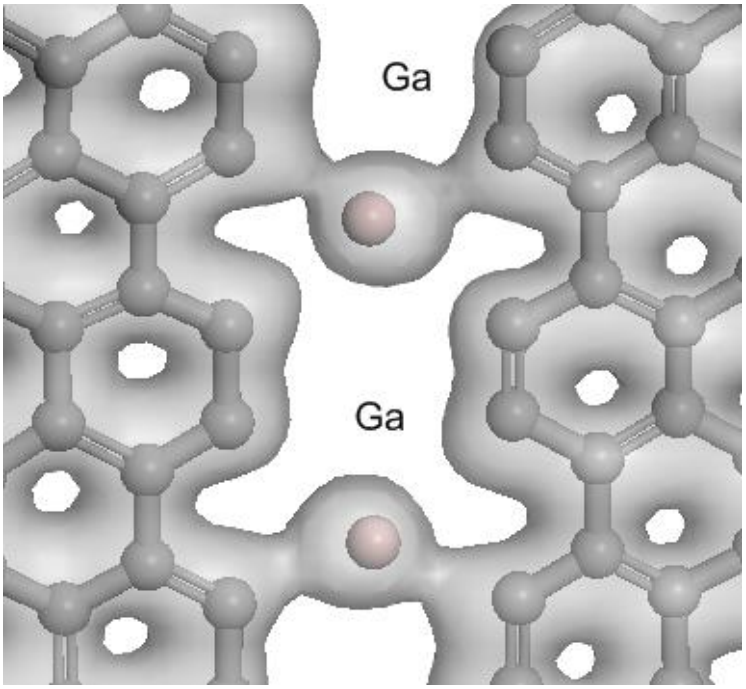

Figure 31 – Modified image of the electron charge distribution in the gap zone. Partial charge transfer to gallium atoms is evident

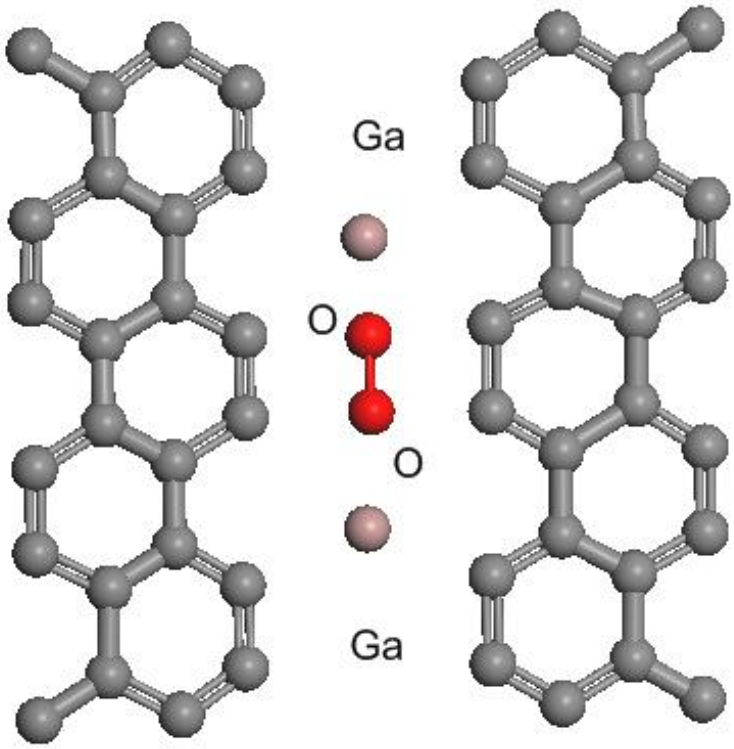

Figure 32 – The configuration that occurs when an oxygen molecule adsorbs on a linear structure of Ga atoms

It was of interest to find out the change in the character of the protective coating gap blocking when the gap size changes. Thus, a decrease in the gap width, as expected, should lead to a change in the structure of the blocking zone, which, in particular, is related to the dimensional effect - the gallium atoms are large and cannot be placed in the plane of the gap. To what extent should the influence of the modified structure on the protective properties of the coating be expected.

The atomic structure of the configuration after calculation and application of the optimization procedure is presented. In the configuration in Figure 33 after optimization, the Ga atoms leave the gap plane and are located at a distance of 0.13 nm from the gap plane with a distance between them of 0.5 nm. The oxygen molecule is adsorbed at a distance of 0.25 nm from the graphene coating plane. The adsorption energy of oxygen is 1.6 eV, which is close to the values obtained for the configuration with a larger gap zone. The binding energy of the Ga - graphene atom is 2.2 eV. The data presented in Figure 34 indicate a significant rearrangement of the configuration blocking the chain gap, but the characteristics of chemisorption capture of oxygen molecules at the gap boundary are actually fully preserved, as evidenced by the electron charge distribution maps and the protective ability of the graphene protective coating remains effective.

It should be noted that functionalization of graphene coatings with gallium is possible in different ways, in particular, by irradiation with a low-energy ion beam directly in the electron microscope chamber.

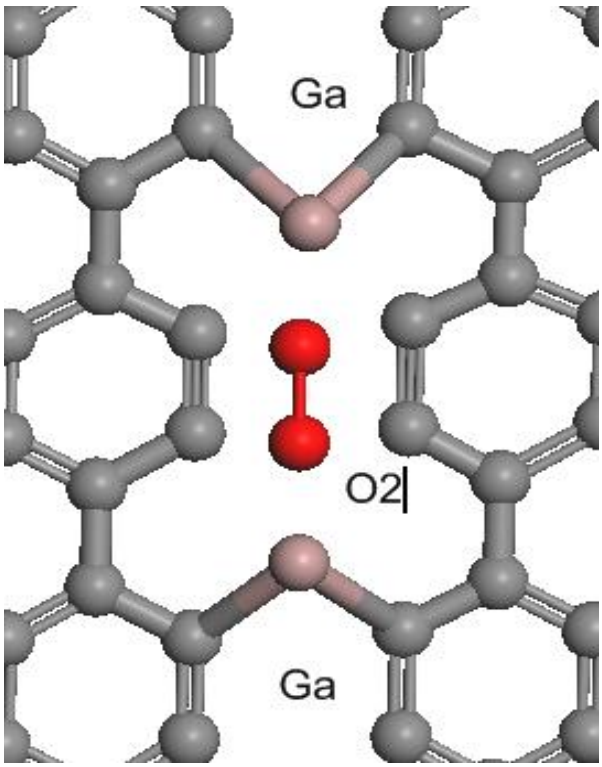

Figure 33 – Computer model of the oxygen molecule adsorption zone element on the blocking chain at a gap width of 0.25 nm

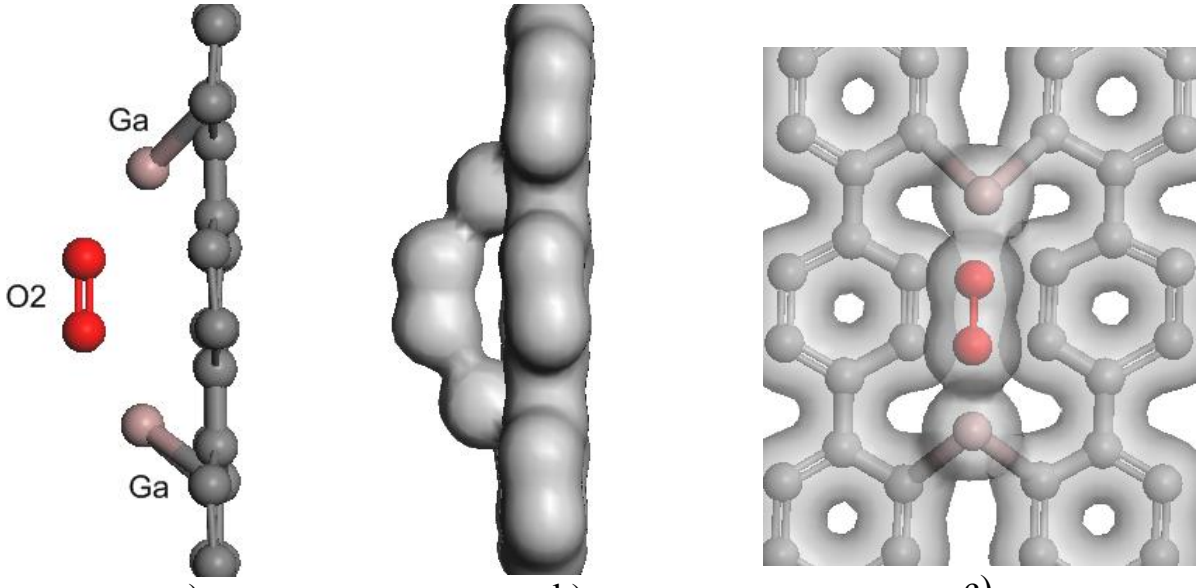

a) b) c)

a) atomic structure (side view); b) electron charge distribution map at a charge density of 30 el/nm^3 (side view); c) modified image (top view)

Figure 34 – View of the structure of the adsorption element of the blocking chain at a gap width of 0.25 nm

Conclusions for section 2

This section is devoted to computer simulation of graphene nanostructures, calculation of the efficiency of their anticorrosion properties using "first-principles" methods. Computer simulation of the investigated nanostructures was carried out using the DMol3 software package, which uses density functional theory (DFT).

In order to theoretically confirm the effectiveness of the protective action of graphene against metal corrosion, two main possibilities for oxygen penetration into the area of the copper surface covered by graphene were simulated: directly through the graphene and through the gap between the substrate and the graphene. Calculations have shown that the energy barrier is very high for the penetration of an oxygen molecule into the area of the copper surface covered by graphene.

Graphene has excellent barrier properties, but in practice it is almost impossible to obtain perfect defect-free graphene. When graphene is synthesized on the surface of the protected metal or when ready grown graphene particles are applied to it, these materials usually contain structural defects, such as vacancies or their complexes, discontinuities in the structure and gaps between graphene sheets. Despite intensive research, this problem, related to the question of the effectiveness of protective coatings containing defects, has not been sufficiently studied. In this part of the work, theoretical studies of the protective properties of a graphene coating containing structural defects (vacancies, divacancies and a small gap in the sheet (0.25 nm)) against oxygen penetration, were carried out. The results of computer simulation and quantum-mechanical numerical calculations suggest that graphene can be a very effective anticorrosion coating, even in the presence of structural defects.

Then the computer models were presented and the quantum-mechanical numerical calculations of the efficiency of the graphene coating functionalized with gallium, which has a sufficiently large gap (0.45 nm), were performed. The presented results indicate the possibility of the effective blocking of the gap-type defect in the graphene protective coating upon the functionalization by the gallium atoms.

3 PRODUCTION AND STUDY OF THE PROTECTIVE PROPERTIES OF GRAPHENE NANOSTRUCTURES

3.1 Synthesis of graphene by chemical vapor deposition (CVD)

Synthesis of high quality graphene is one of the important processes of creating anticorrosion coatings. Graphene synthesis means obtaining graphene of the desired size, purity, crystallinity using various methods.

In the CVD method graphene is synthesized directly on various transition metal substrates such as Ni and Cu by saturating them with carbon under the influence of various gaseous hydrocarbons such as methane, ethylene, acetylene and benzene at high temperature.

In this part the technique of CVD synthesis of the graphene coating [151] in a sealed flow tube (Figure 35 (a)) with the diameter d = 80 mm was developed. A 100 μm-thick nickel plate with purity of 99.99% was used as a catalyst substrate for graphene growth. Argon-hydrogen mixture was passed as a buffer gas and benzene vapor was used as a carbon source.

Argon was passed through the quartz tube of the CVD furnace, with a nickel catalyst substrate pre-installed in it, at normal pressure and a flow rate of about 80 sccm for t = 30 min to displace oxygen and moisture. After this procedure, the furnace heating process was started, the heating rate was set to 35 °C/min, and the previous flow rate mode was maintained with the addition of 20 sccm. When T = 900°C was reached, the temperature of the system stabilized, and annealing was carried out for t = 60 min, this procedure was carried out to increase the average grain size of nickel. After that, at a temperature of T = 900 °C, benzene vapors were introduced into the system with a constant flow of the argon-hydrogen mixture, according to the scheme shown in Figure 35 (b). The hydrocarbon mixture was introduced for 5 minutes. At the end of the synthesis time, the heating of the furnace was turned off, and the system was naturally cooled to T = 80°C in an argon flow, and then the sample was transferred to a cooler part of the tube and then taken out. The general scheme of the synthesis process is shown in Figure 36. Figure 37 shows the photo of nickel plate after synthesis. As the nickel foil cools, folds of graphene sheets are formed on it due to the different thermal expansion coefficients of nickel and graphene. According to these folds we can talk about the presence of ultrathin layers of graphene. Figure 38 shows electron micrographs of nickel foil after graphene synthesis. Analyzing the microphotograph in Figure 38 (a), one can see the boundaries of the nickel grains and estimate their average size (130 μm), which in the growth process determines the average lateral size of graphene.

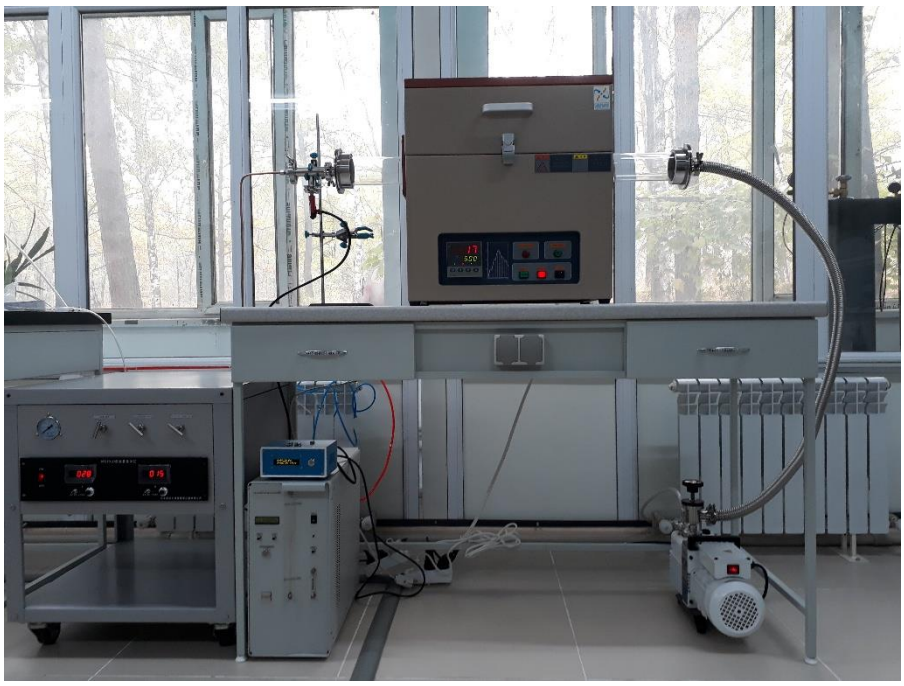

a)

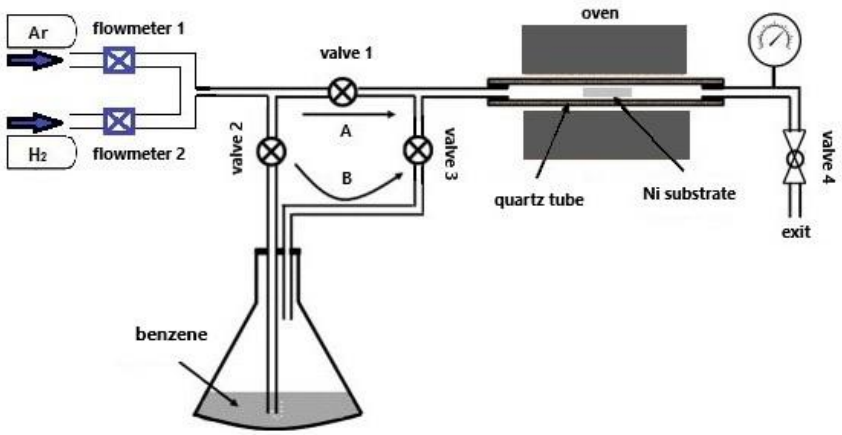

b)

a) appearance; b) scheme

Figure 35 – CVD installation

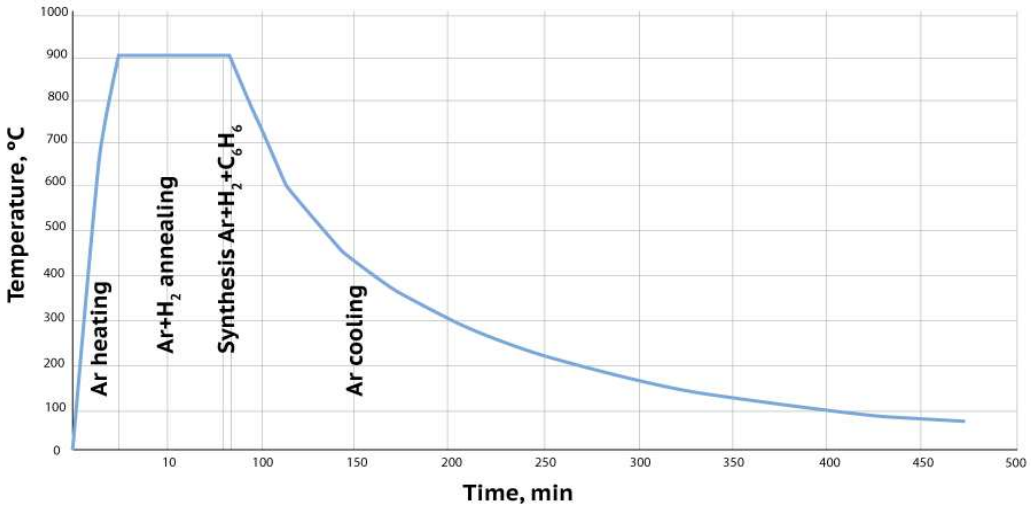

Figure 36 – CVD-graphene synthesis process

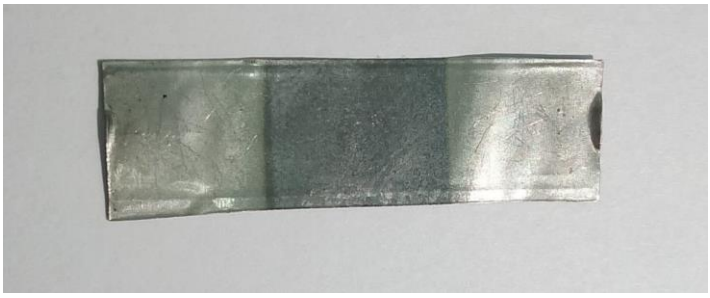

Figure 37 – Nickel plate after synthesis

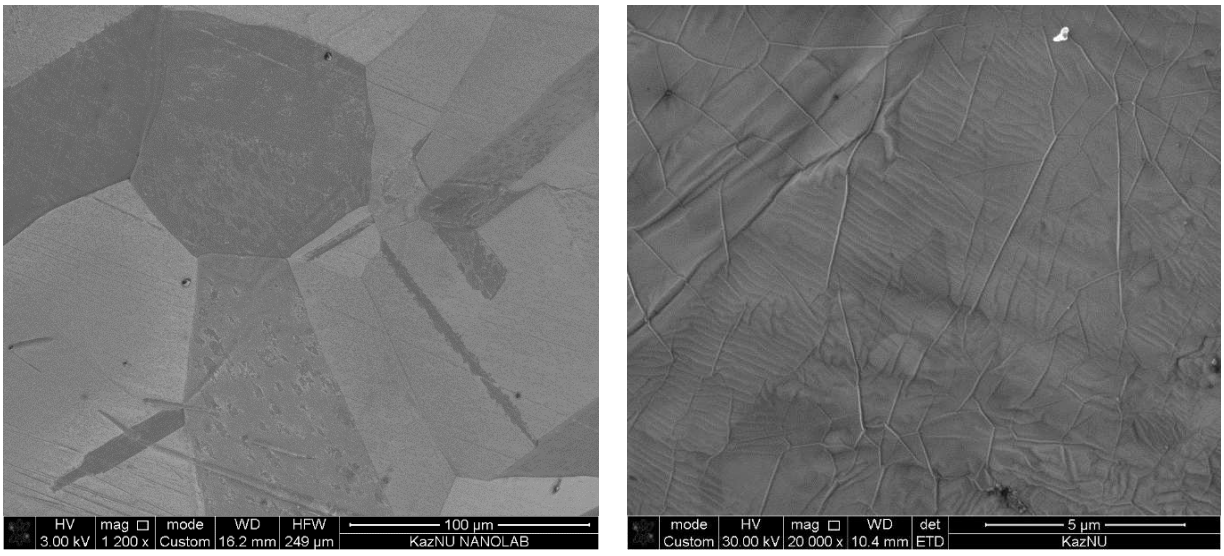

a) b)

Figure 38 – Image of graphene on nickel at different magnifications

The quality of the graphene, as well as the number of layers was estimated from the analysis of Raman spectra taken with the NTEGRA Spectra. Lines were excited by a blue laser with a wavelength of 473nm. Figure 39 shows the Raman spectrum of the graphene coating after transfer by mechanical exfoliation to a dielectric substrate (Si/SiO_2). It can be seen that the spectrum is characterized by a fairly sharp G peak (1581cm^{-1}) and a symmetric 2D peak (2734 cm^{-1}). There is also a small D peak (1360 cm^{-1}) in the spectrum, which indicates the defect density in the CVD-graphene. According to [152] the number of graphene layers is determined by the ratio of I_{2D}/I_G peak intensities. The ratio I_{2D}/I_G ~ 2-3 is typical for monolayer graphene, for two-layer graphene $2>I_{2D}/I_G>1$and for few-layer graphene $I_{2D}/I_G<1$ [152, 153]. Based on the ratio of the intensities of the I_{2D}/I_G Raman spectra peaks, you can conclude that the CVD-graphene obtained on the nickel foil is a monolayer.

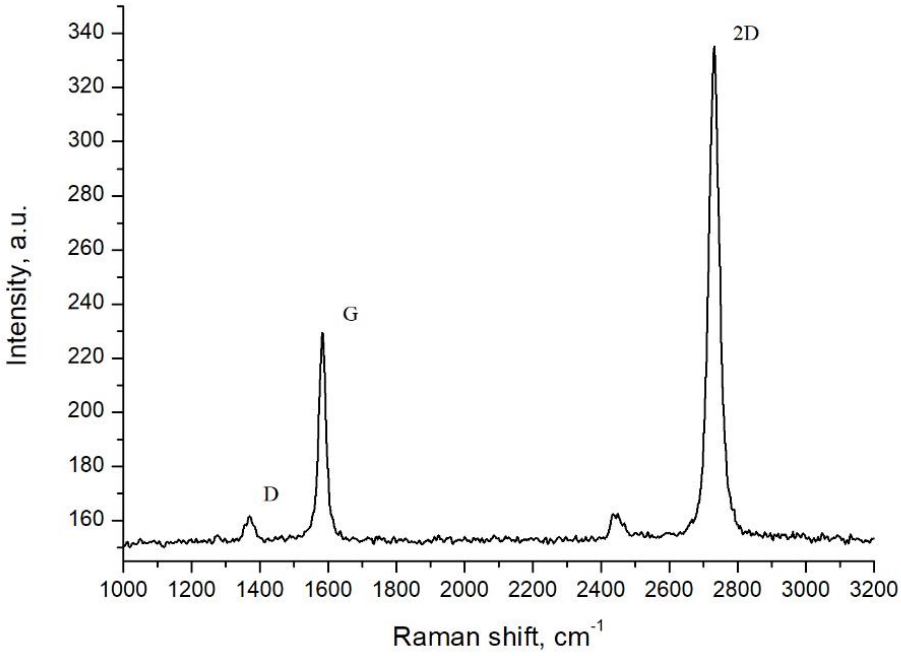

Figure 39 – Raman spectrum of CVD-graphene after transfer by mechanical exfoliation

A method of transferring ultrathin layers of graphite and graphene on the surface of other materials and substrates for research, by wet etching, has also been developed [154]. This method makes it easy to transfer graphene to the desired material surfaces. An aqueous solution of 3 g/ml $FeCl_3$ was used as an etchant. Nickel foil with the side on which graphene was synthesized lowered to the surface of the solution for several hours. After the partial nickel etching process, the remaining part was lifted with tweezers, and a thin, transparent layer of graphene remained on the surface of the etchant for several hours to remove nickel residues. Then these layers were caught on the glass surface and transferred to distilled water to wash the etchant. Figure 40 schematically shows the main steps of the CVD-graphene transfer process. Figure 41 shows the Raman spectrum (smoothed) of graphene after the transfer

process, in which, as we can see from the I_{2D}/I_G peak ratio, the obtained spectrum corresponds to the region of few-layer graphene.

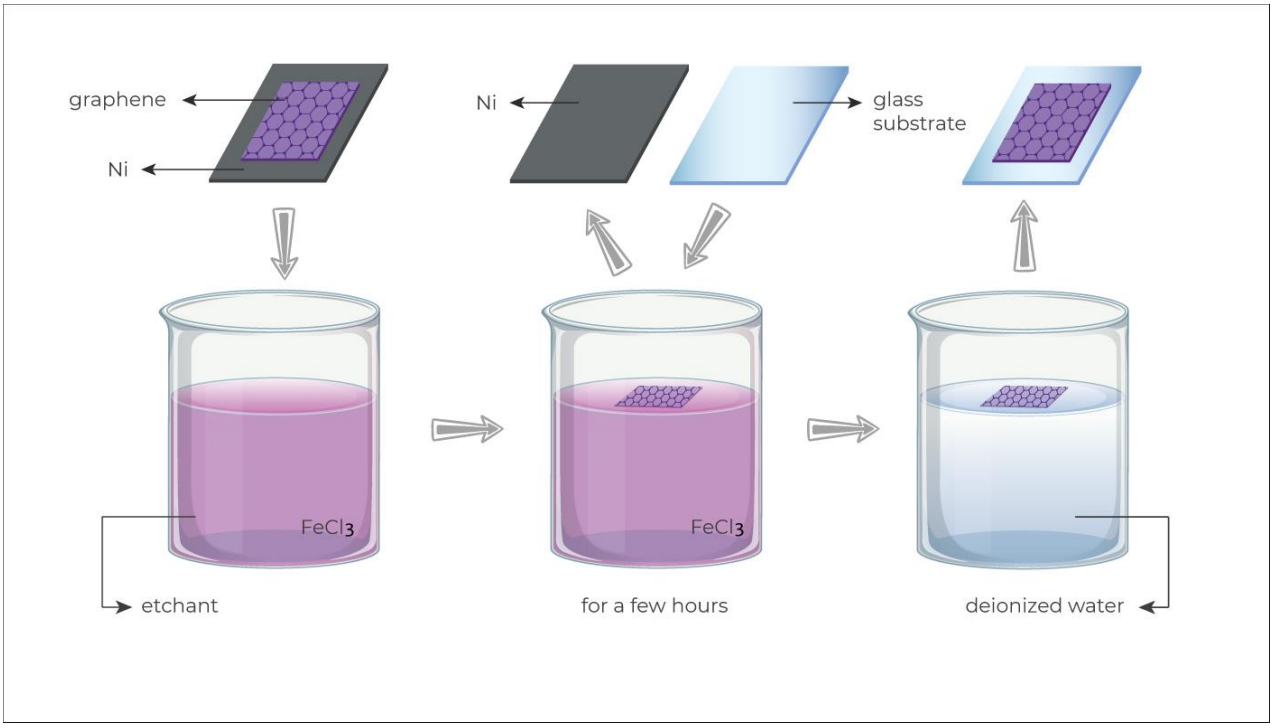

Figure 40 – Illustration of the CVD-graphene transfer process by wet etching

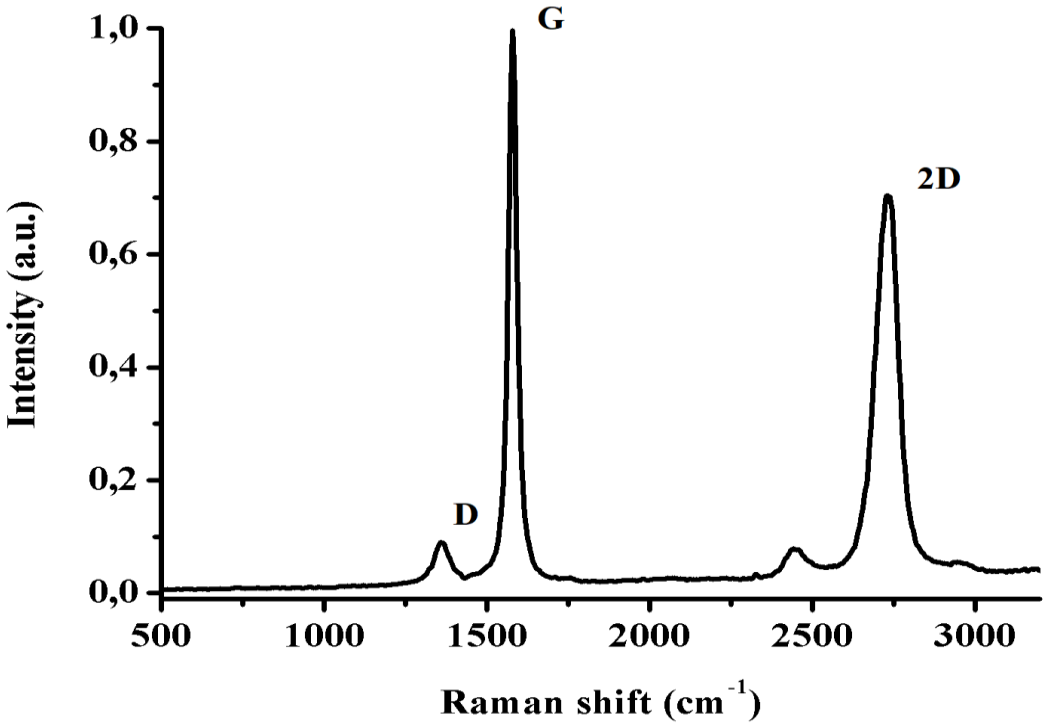

Figure 41 – Raman spectrum of few-layer graphene after transfer process by wet etching

3.2 Obtaining graphene by carbon diffusion through nickel

Graphene and few-layer graphene nanostructures were grown on polycrystalline nickel substrates by carbon diffusion through nickel on a vacuum setup (VUP-5M), the experiment scheme is shown in Figure 42. First, clean (99.99%) 60 μm-thick nickel foil was cleaned in an ultrasonic bath for 10 minutes, then washed with isopropyl alcohol and deionized water and dried under a stream of dry nitrogen. After cleaning, the nickel foil was annealed in a vacuum at a residual pressure of 10^{-4} Pa in order to grow the nickel grains and smooth the surface. Heating was carried out by passing a current (20-30 A) through the nickel foil and the sample temperature was maintained at about 1000 °C for 30 min. After that, highly oriented pyrolytic graphite was pressed tightly onto one side of the already annealed nickel and was also heated with the same vacuum at a rate of about 100 °/min above 1300 °C, the sample temperature was measured with a thermocouple.

For carbon diffusion in nickel $D(T) = D_0 \exp(-E_a/kT)$, where $D_o \approx 2.48 \cdot 10^{-4}$ m^2/s, activation energy $E_a \approx 1.74$ eV. The calculated time of carbon diffusion through the nickel foil of thickness L = 60 μm, at sample temperature T = 900 °C is about $\tau \approx L^2/4 \cdot D\ (1173K) \approx 2$ to reach the surface from the other side. Figure 43 illustrates the traces of the graphite source on the one side of the foil and the appearance of diffused carbon atoms on the other side.

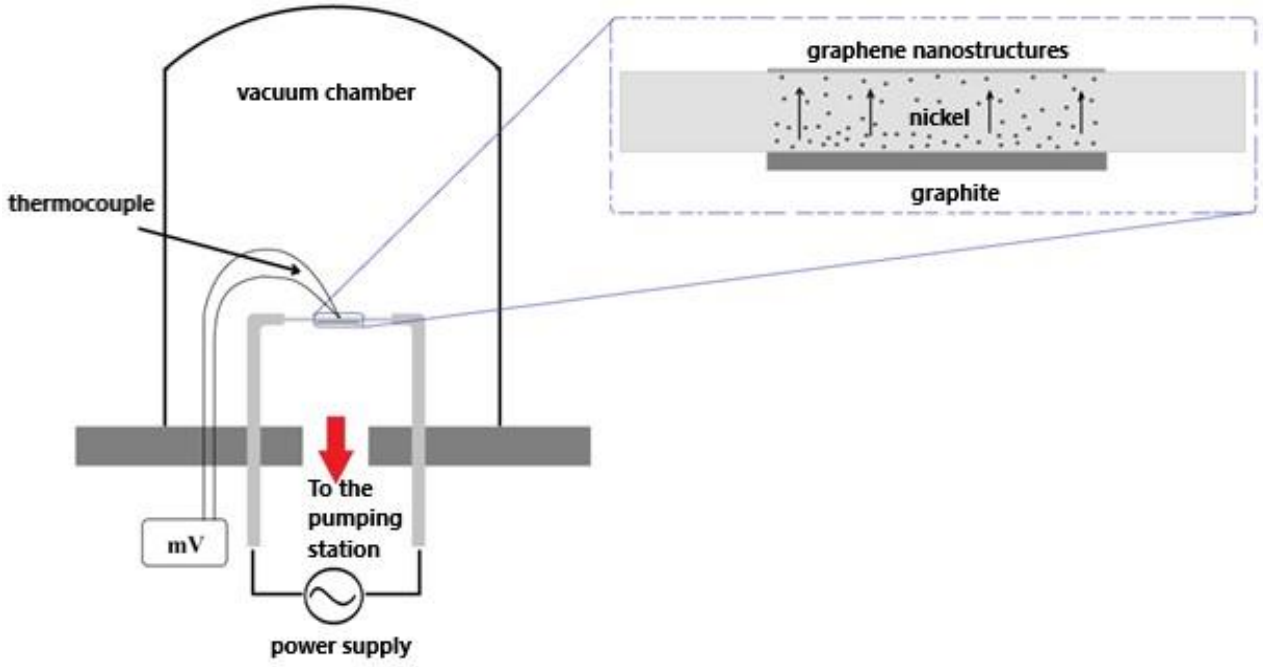

Figure 42 – Scheme of obtaining graphene on nickel by the diffusion method

a) b)

a) the first side; b) the second side

Figure 43 – Nickel after the diffusion process

Graphene on nickel obtained by this method was studied by scanning electron microscope and Raman spectroscopy (Figure 44). The microphotographs (Figure 44 (a)), obtained with a scanning electron microscope, clearly show the folds that form during cooling due to the difference in the thermal expansion coefficients of graphene and nickel, as well as by the CVD method. Figure 44 (b) shows the Raman spectrum of graphene measured under laser excitation (473 nm). The spectrum shows fairly well-defined intense lines: G-peak at ~1581cm^{-1} and the 2D-peak at ~2703 cm^{-1}. It is also seen that the D-peak at 1350 cm^{-1}, which indicates the defectiveness of graphene is completely absent. It is also clear from the ratio of the G and 2D peaks that the obtained graphene is a monolayer. Figure 45 shows an optical micrograph of the graphene obtained by the diffusion method on nickel at 900 °C.

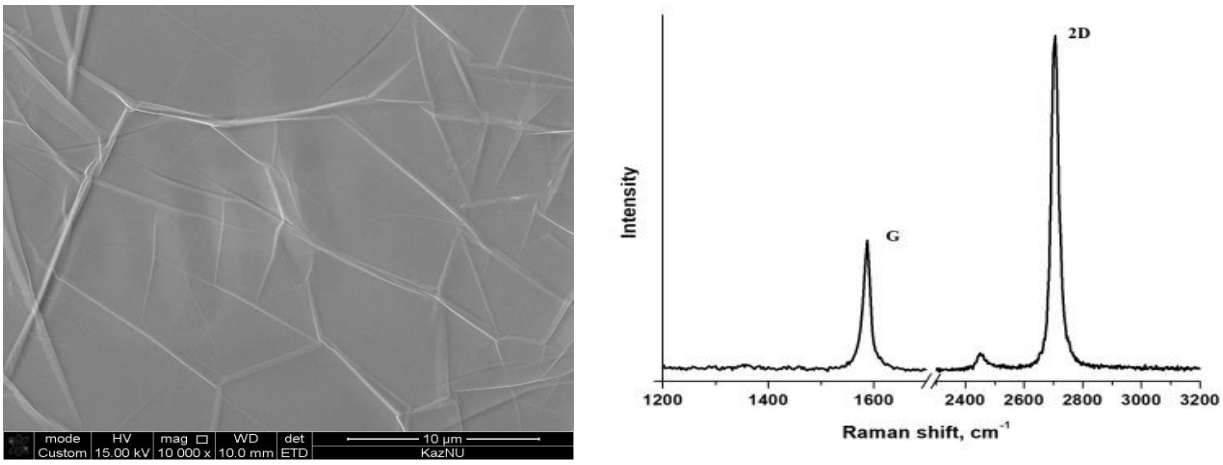

a) b)

a) electron microphotography; b) Raman spectrum

Figure 44 – Graphene grown by carbon diffusion through nickel

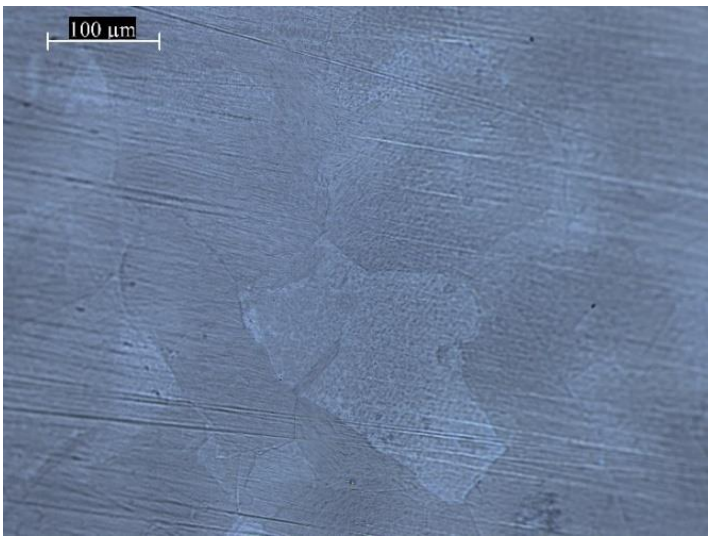

Figure 45 – Optical micrographs of graphene obtained by the diffusion method at 900 °C

The optical micrograph clearly shows the nickel substrate grains and their boundaries, as well as estimate the grain size of the graphene, which was approximately 100*200 μm^2. According to [155] the number of the graphene growth nucleation centers on the Ni (111) surface is extremely small, which is an important factor for the growth of large single-domain graphene crystals. According to the literature data the carbon diffusion in Ni (111) can occur mainly through the grains and their boundaries or in other defective places in the graphene layer [156,157].

3.3 Functionalization of graphene nanostructures

3.3.1 Functionalization of few-layer graphene nanostructures with gallium ions

In this part of the thesis, the functionalization of few-layer graphene nanostructures with low-energy gallium ions was carried out. The few-layer graphene nanostructures were obtained by the process of carbon diffusion through nickel and identified by Raman spectroscopy, as well as micrographs were taken from these samples and energy-dispersion elemental analysis was performed (Figure 46). Next, these samples were irradiated with gallium ions on a dual-beam scanning electron microscope with a built-in gallium gun. The total irradiation area of Ga^+ ions with energy of 2 keV and beam current of ~8.9 pA was 50 μm^2. The radiation dose was $\approx 5 \cdot 10^{13}$ ions/cm^2 with a surface density of carbon atoms in graphene $\approx 3.82 \cdot 10^{15}$ ions/cm^2, which indicates a low dose of radiation. Figure 46 (b) presents the Raman spectra of a few-layer graphene nanostructure before (2) and after (1) the irradiation process. From these spectra can be observed the appearance of additional peaks D, D’ and D+D’, which are responsible for the formation of defects in a few-layer graphene nanostructure. The intensity of the 2D peak decreases with increasing radiation dose. There is also change in the output of secondary electrons which was detected compared to the non-irradiated region (Figure 46 (a)). To detect gallium after

irradiation, elemental analysis was performed at low accelerating stresses in order to enhance the sensitivity of this method to the surface (Figure 46 (c,d)). The energy dispersion spectrum after irradiation demonstrates the appearance of a small peak of gallium.

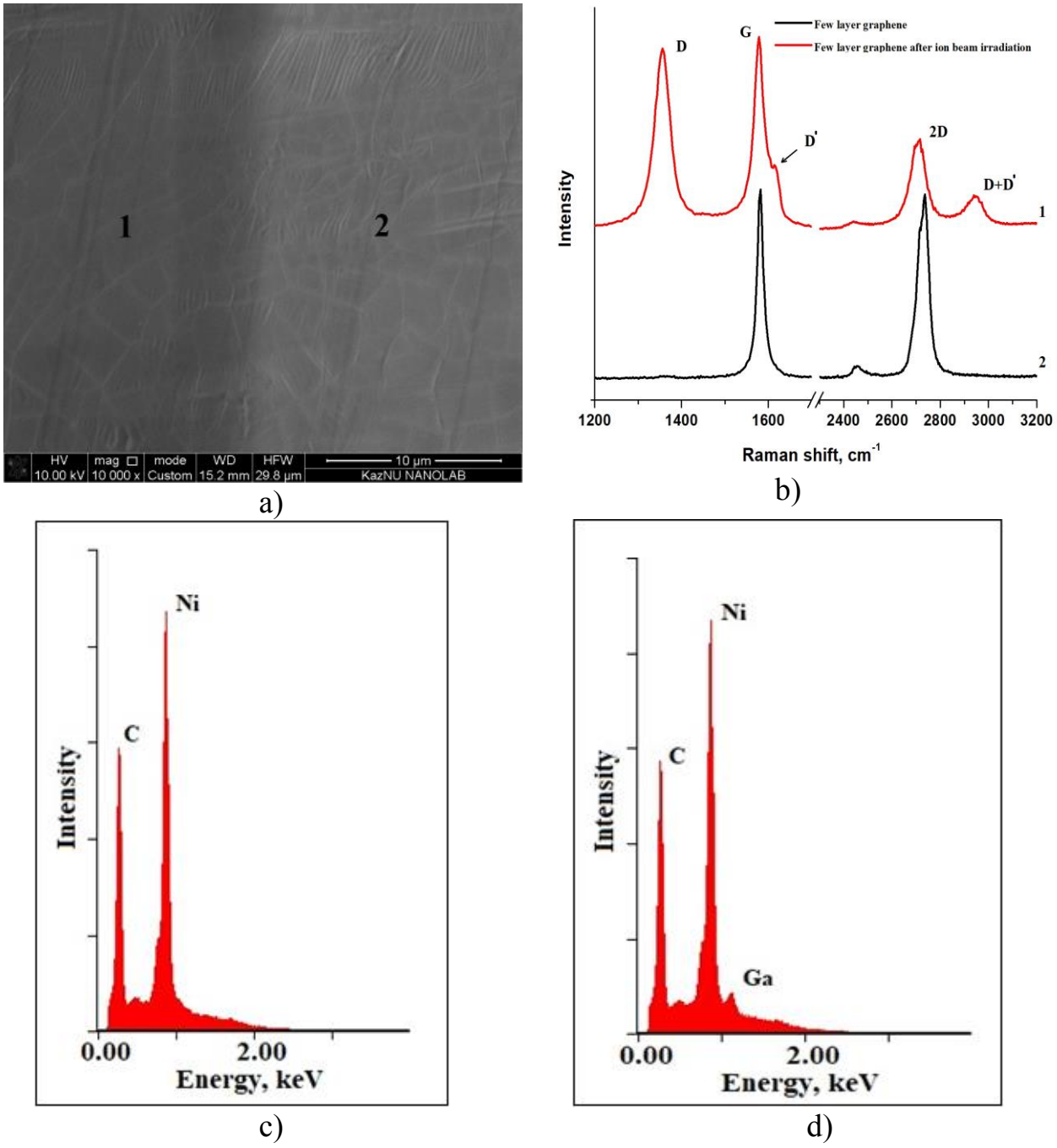

Figure 46 – a) Electronic microphotography of few-layer graphene nanostructures on nickel; left side (1-dark contrast) irradiated by gallium ions; right side (2-light contrast) unirradiated; b) Raman spectra with unirradiated (black line-2) and irradiated (red line-1) parts; c),d) EDS spectra with unirradiated and irradiated parts, respectively

3.3.2 Production of graphene oxide by the modified Hummers' method

One of the most common FGNS representatives is the GO due to its potential applications in various fields of science and technology. For example, the use of GO in humidity sensors can improve its performance [158,159]. In this work, the GO was obtained chemically (modified Hummers' method). The essence of the method is the processing of graphite powder with strong oxidizing agents, the resulting structures are called graphite oxide, and after appropriate treatment with ultrasound, graphene oxide is obtained. Figure 47 shows all the main stages of obtaining GO by the modified Hummers' method. To begin with, an ice bath of 0 °C was prepared on a magnetic stirrer with a temperature controller and a 1000 ml flask was placed in it, with graphite powder weighing 3 g in it. Then 69 ml of concentrated H_2SO_4 was added to graphite powder, after which sodium nitrate ($NaNO_3$) weighing 1.5 grams was added to the measuring flask, and then potassium permanganate weighing 9 grams ($KMnO_4$) was gradually added. The resulting solution was stirred for 3 hours with a temperature below 20 ° C. After stirring the solution for 3 hours, 15 ml of deionized water was added, after which the temperature of the solution was raised to 35 °C and this temperature was maintained for another 30 minutes. Then again deionized water was added and the temperature was raised to 85 °C and this temperature was also maintained for 30 minutes. To complete the reaction, a 30% solution of hydrogen peroxide (H_2O_2) was added to the mixture until the color of the mixture changed to bright yellow and until the evolution of gases ceased. The solution was washed in 5% hydrochloric acid (HCl) to remove metal ions, and then the solution was washed and filtered several times in deionized water using a centrifuge until neutral (pH≈7) was achieved. The resulting solution was sonicated in an ultrasonic bath for one hour. Figure 48(a) shows a photograph of the resulting aqueous dispersion of graphene oxide.

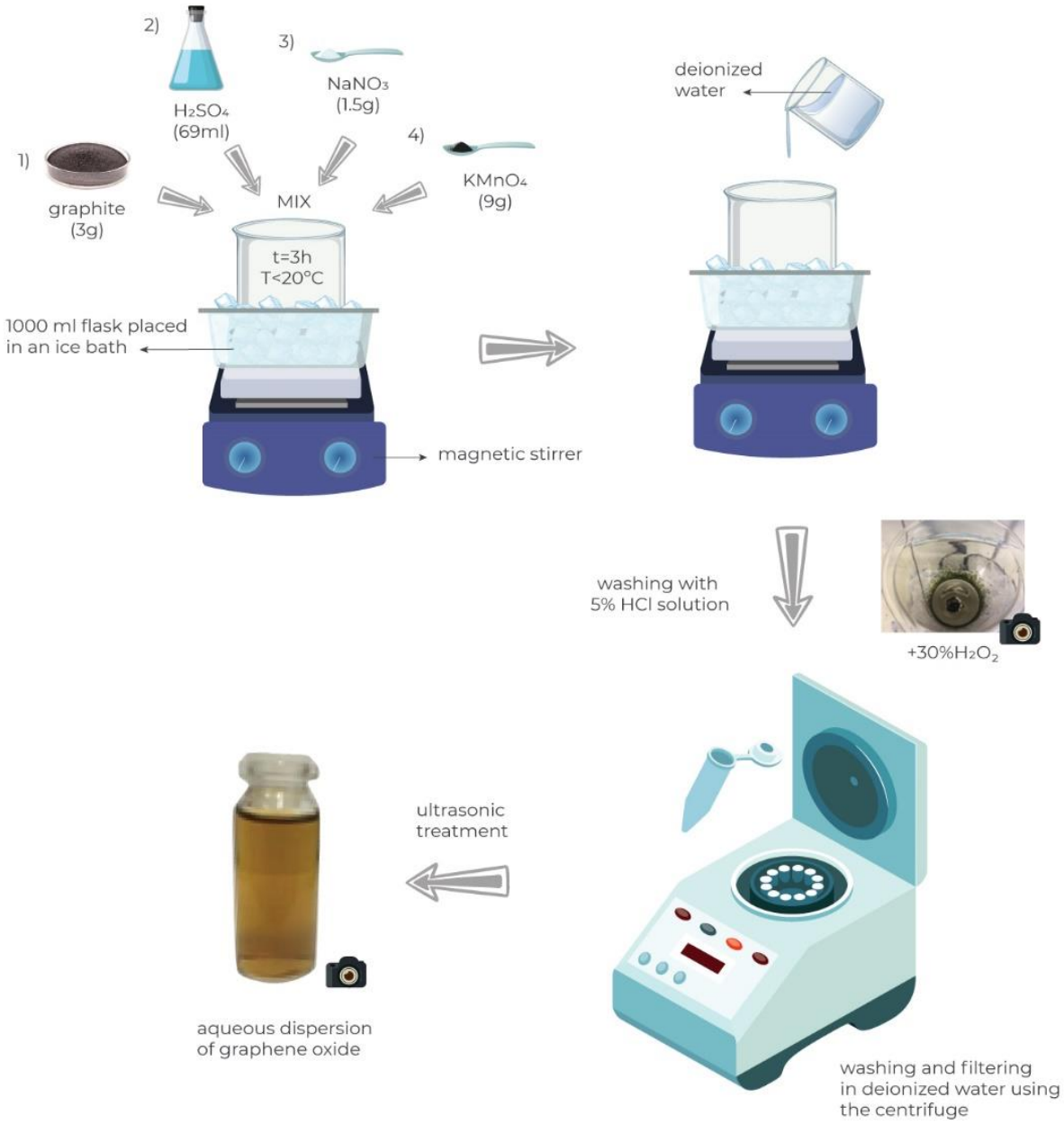

Figure 47 – The process of synthesis of GO by the modified Hummers' method

To obtain graphene oxide films, the resulting aqueous dispersion of graphene oxide was poured into petri dishes and subjected to a temperature effect of 40 °C for 3–4 hours on a magnetic stirrer until dried GO films were obtained. Figure 48 (b) shows the Petri dish with already dried GO films, and figure 48 (c) shows the optical microphotography of the surface of the dried graphene oxide film. The Raman spectrum of graphene oxide (Figure 48 (d)) mainly consists of a broad D peak of ~ 1350 cm^{-1}, corresponding to structural defects, a G peak of ~ 1587 cm^{-1}, corresponding to the vibration of the graphite region, and a wide weak ledge, from

2600 cm^{-1} to 3200 cm^{-1}. D/G is about 0.93, which indicates a large number of defects within the crystal lattice.

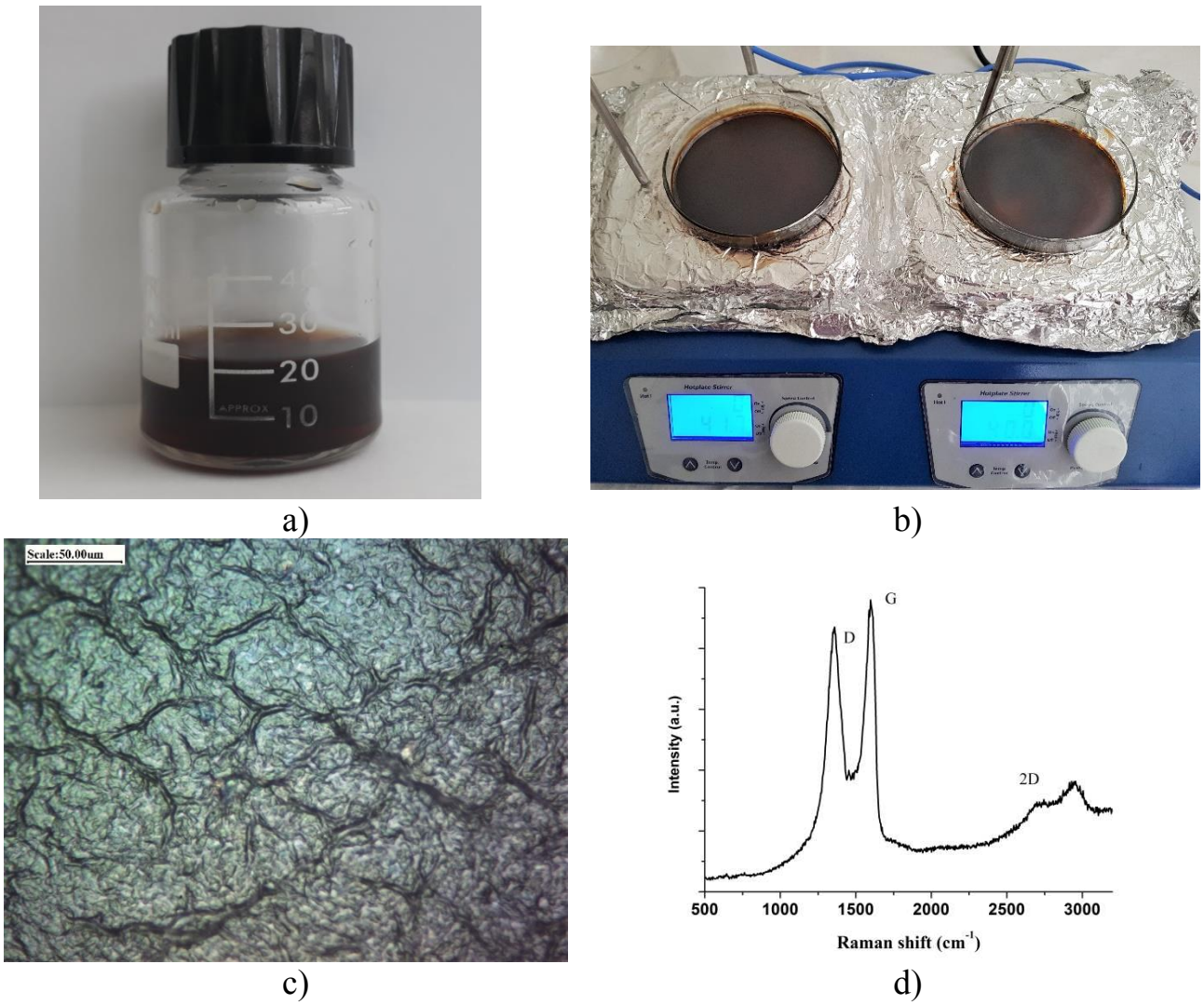

a) b)

c) d)

a) Aqueous dispersion of GO (concentration 1mg/ml); b) Photograph of dried GO films in Petri dish; c) Optical microphotography of GO film surface; d) Raman spectrum of obtained GO

Figure 48 – GO obtained by the modified Hummers' method

Thermogravimetric analysis is performed by measuring the sample mass in the oven with analytical weights as the sample temperature gradually rises. In TGA, mass loss occurs if the heating produces volatile components. Thermogravimetric analysis of the GO sample was performed on the TA Discovery SDT 650. The sample was placed inside a platinum cup and heated in a nitrogen atmosphere at a rate of 10°C per minute to a final temperature of 900°C. Figure 49 shows the TGA curve of the GO sample. The resulting TGA data showed a typical weight loss as a function of temperature. Three areas are distinguished over the entire temperature range. In the temperature range from

room temperature to 180 °C, mass loss occurs, which is associated with the evaporation of adsorbed water. In the range of 180–300 °C, the sample demonstrates a rather sharp mass loss of about 25%, which is explained by the loss of thermally unstable oxygen functional groups. After 300 °C and up to 900 °C, the graphene oxide sample underwent a gradual mass loss of about 12%, which indicates further removal of various functional groups.

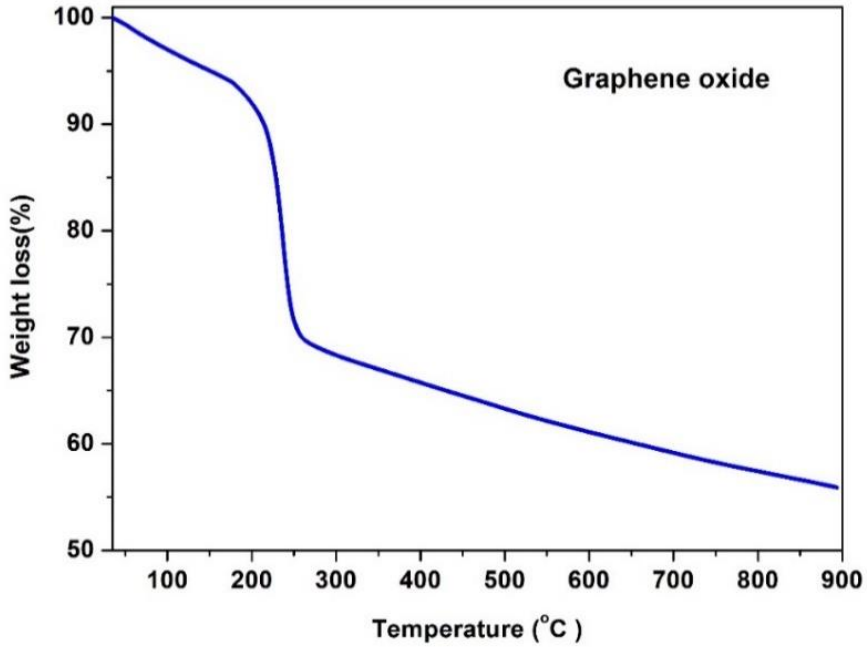

Figure 49 – Thermogravimetric analysis of the GO sample

Next, we evaluated the interplanar distance d of the obtained initial GO and GO after TGA (T-RGO) on a Bruker D8 ADVANCE ECO A25 X-ray diffractometer. X-ray diffractometry (XRD - X-ray diffractometry) refers to common non-destructive methods that characterize the structure and phase composition of crystalline materials. The interpretation of the diffraction patterns made it possible to determine the interplanar spacing (d) of GO (Figure 50 (a)) and T-RGO (Figure 50 (b)), substituting the obtained value of 2θ into the Wulff-Bragg's condition. The interplanar distance of GO decreased from 0.76 nm to 0.34 nm, which indicates that the original GO sample had a decrease in the number of H_2O molecules, oxygen and other functional groups after temperature exposure in a nitrogen atmosphere.

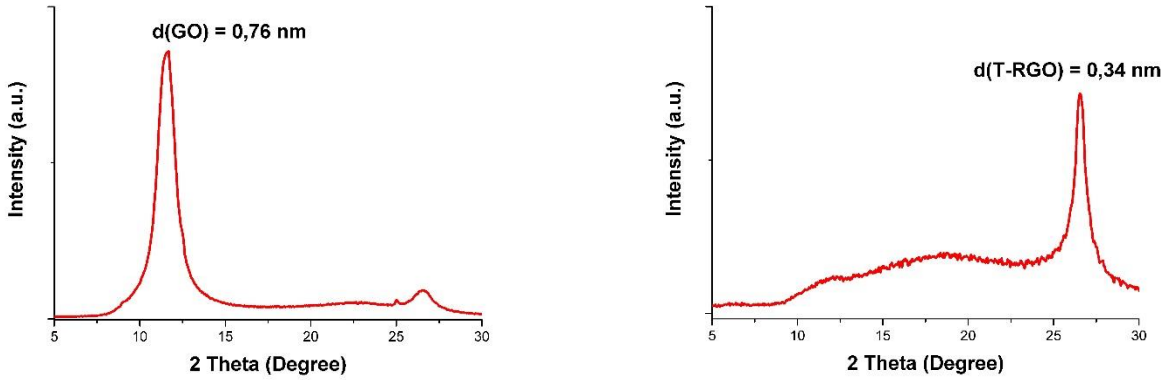

a) GO b) T-RGO

Figure 50 – XRD of GO and thermally reduced GO (T-RGO)

3.4 Electrophoretic deposition of GO on the surface of copper and nickel

The formation of GO-based protective coatings on Cu and Ni surfaces was carried out by electrophoretic deposition, which is one of the promising methods for the deposition of nanostructures with a number of advantages, including the simplicity and low cost of the experimental setup, high productivity, the ability to control the coating thickness, and a wide choice of substrates. Electrophoretic deposition is usually carried out in a two-electrode cell, where the applied electric field can be constant or modulated (Figure 51).

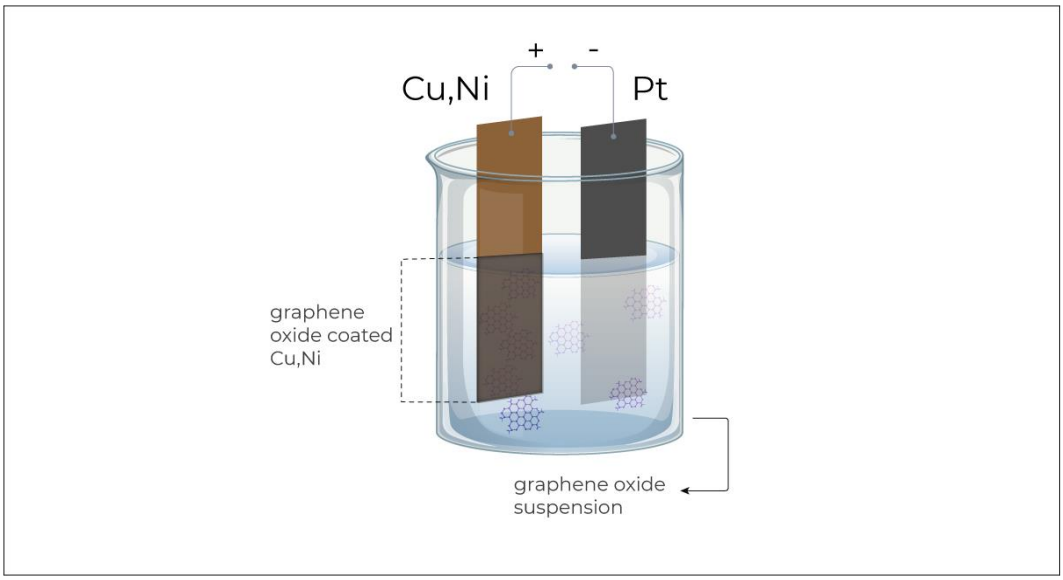

Figure 51– Scheme of a cell for electrophoretic deposition of a graphene oxide film

Electrophoretic deposition is a two-step process. The first stage - particles suspended in the liquid under the action of an electric field move to the electrodes. The second stage - particles accumulate on one of the electrodes and form a layer. Naturally, particles in suspension will be affected by an electric field if they are

charged. In an aqueous solution (deionized water) of graphene oxide, the particles have a negative charge due to the presence of oxygen-containing groups. In this work, the negative electrode is a platinum foil, and the positive electrode, on which a graphene oxide film is formed, is copper and nickel with an applied potential of 100 V. At a distance between the electrodes of 1.5 cm and an oxide aqueous solution concentration of 0.1 mg/ml, the current density was about 1 mA /cm^2. To carry out electrophoretic deposition, graphene oxide obtained by the Hummers' method was dispersed in distilled water using ultrasound for 30 min until a completely homogeneous solution was formed. Copper and nickel electrodes measuring 0.8 cm by 3.5 cm were pre-sonicated in acetone for 5 minutes, followed by washing in isopropyl alcohol. Figure 52 shows the EDS results of initial foils after cleaning.

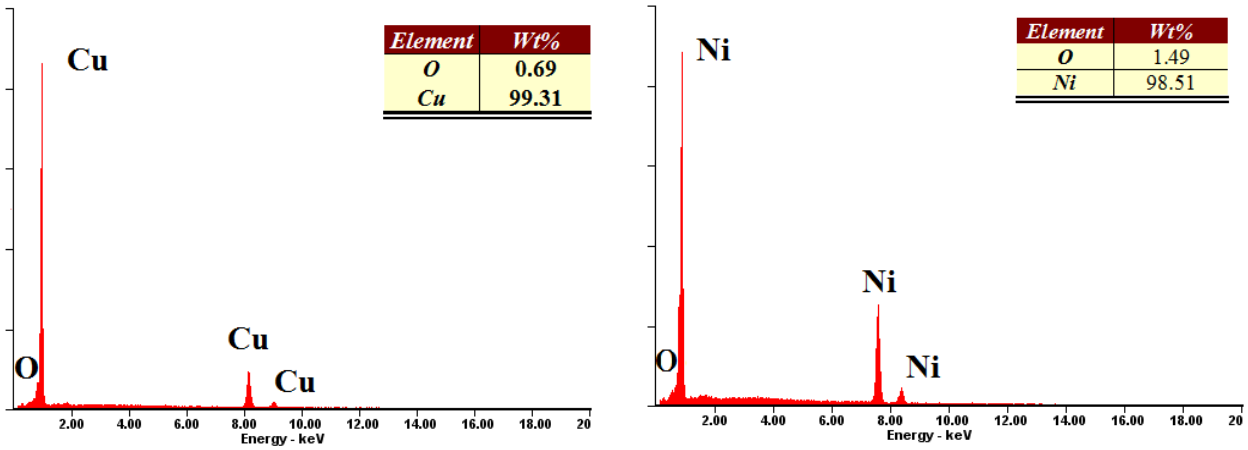

a) copper b) nickel

Figure 52 – Elemental composition of initial foils

Further, graphene oxide films with different growth times were obtained on copper and nickel foils 100 μm thick by electrophoretic deposition (Figure 53): 1 sample - t = 1 second, 2 sample - t = 3 seconds and 3 sample - t = 5 seconds. The study of the uniformity of the coatings was carried out on a scanning electron microscope. Figure 54 (a,d) shows microphotographs of copper and nickel surfaces after cleaning, with observed patterns associated with foil production technology. After one second of deposition, both copper and nickel electrodes showed areas without film, indicating insufficient deposition time (Figure 54 (b,e)). The samples, on which the deposition was carried out for t = 3 seconds or more while maintaining the same growth parameters, the coatings were continuous (Figure 54 (c,f)).

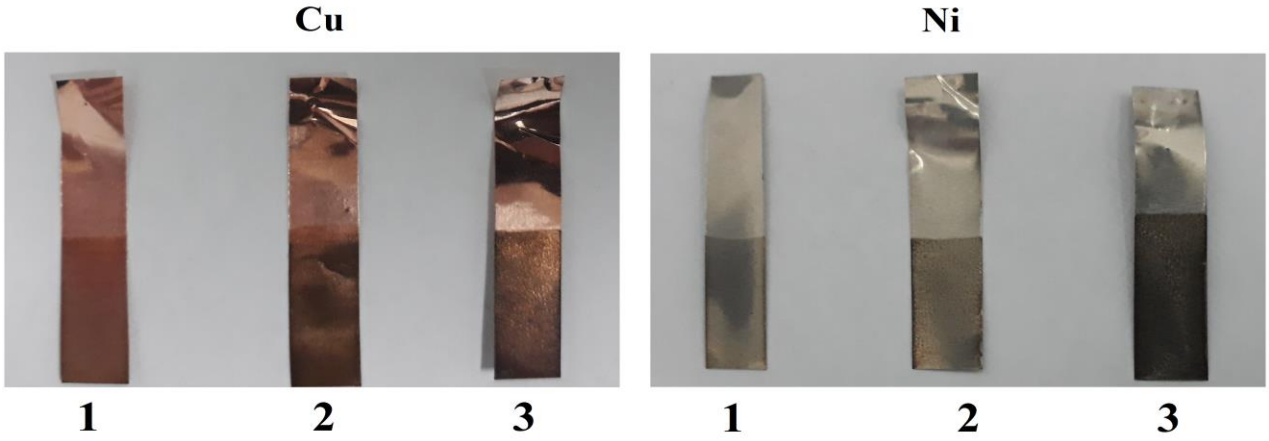

Figure 53 – Photo of copper and nickel electrodes after electrophoretic processing

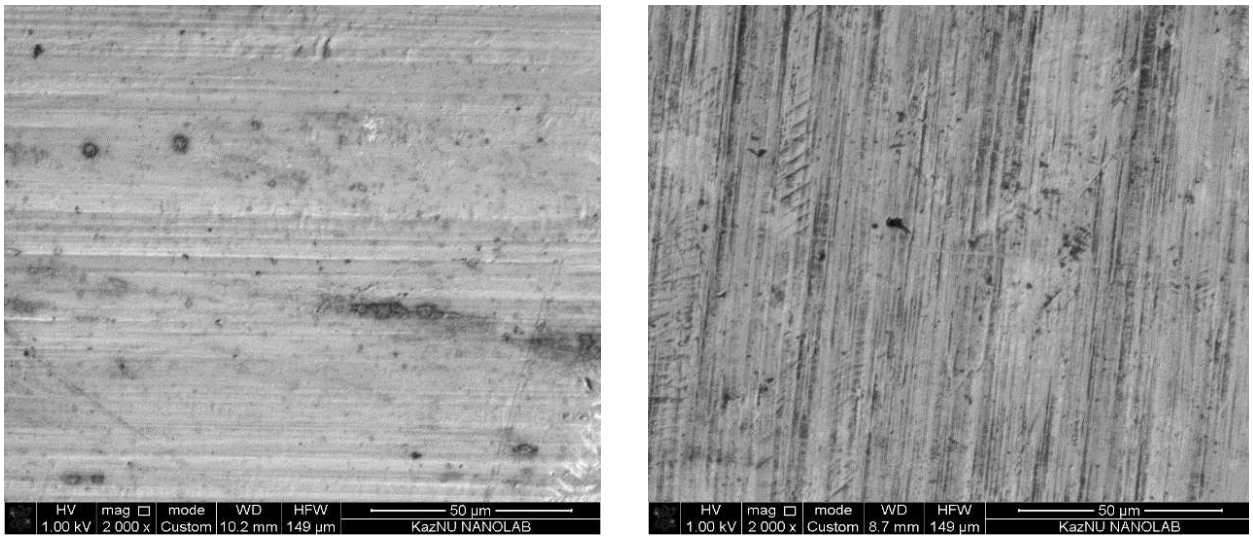

a) d)

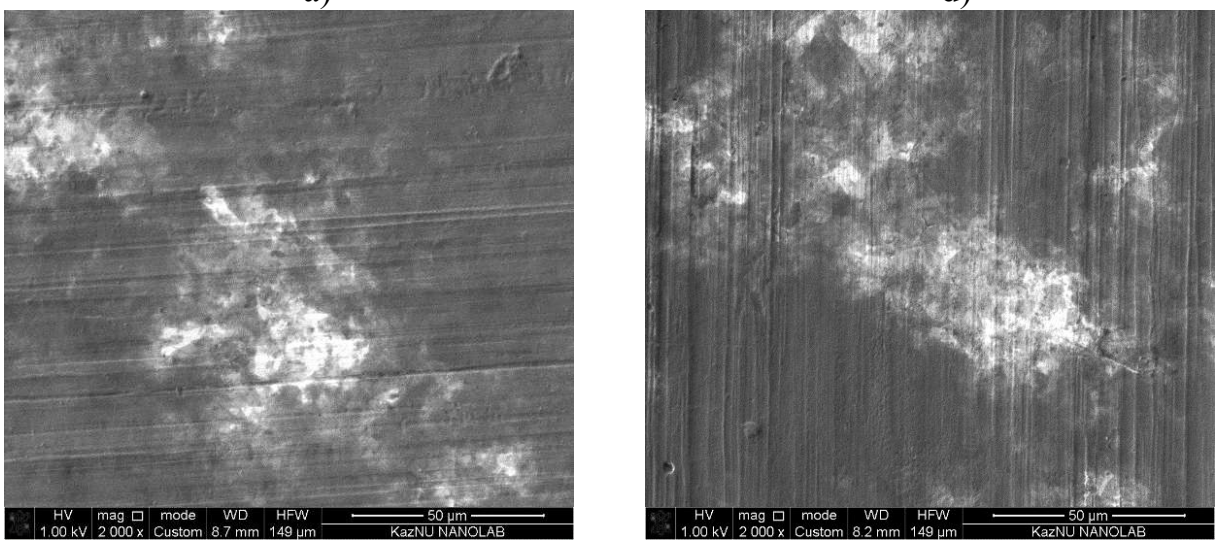

b) e)

Figure 54 – Electron microscopic images of samples before and after coatings, page 1

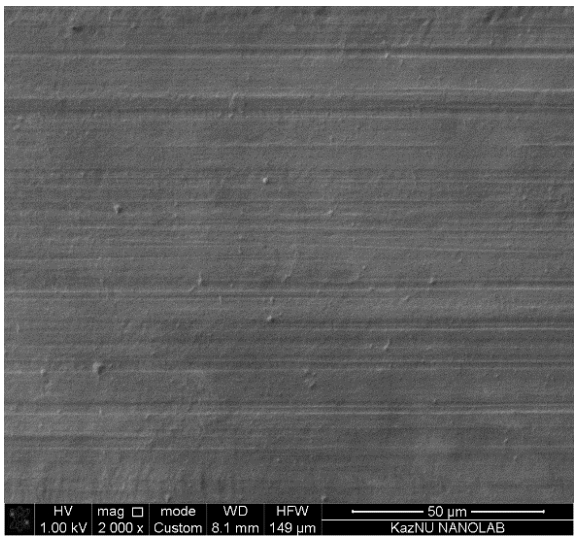

c)

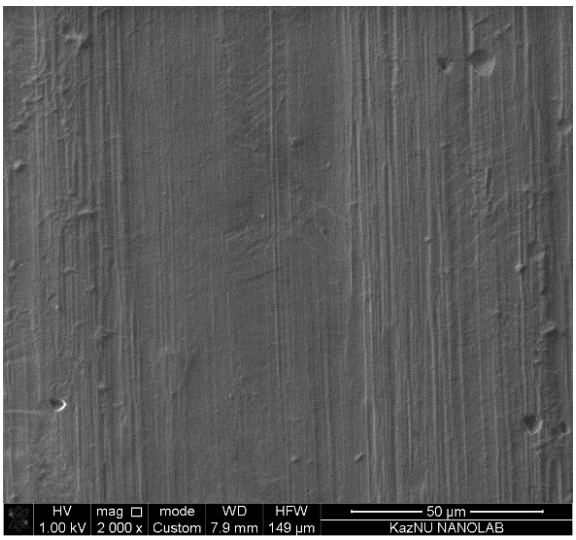

f)

Figure 54, page 2

The composition and thickness uniformity of the coatings were studied by X-ray spectral microanalysis. The results of the analysis are shown in Figure 55. Since the films are quite thin, the characteristic X-ray peaks of the electrodes (copper and nickel) are observed in the spectrum, and the analysis is considered semi-quantitative. Analysis of the distribution curves relative to the weight percentage of elements along the white line in Figure 55 (b, d) allows us to speak about the homogeneity of the composition and the uniformity of the coating thickness for both electrodes. The coating thickness for the deposition time t = 10 seconds at the same process parameters was about 1 μm. After the samples were thermally treated in a flow tube furnace in an argon flow (99.999%) with a set consumption of 50 ml/min and an annealing temperature of 300 °C within 30 minutes. The elemental analysis results are presented in Figure 56. There was a decrease in the oxygen level compared to the original coating compositions presented in Figure 55 (a, c), and, accordingly, a recovery of GO. Reduced GO nanostructures are able to produce corrosion protection of surfaces of copper, nickel and other materials, as the properties become close to graphene.

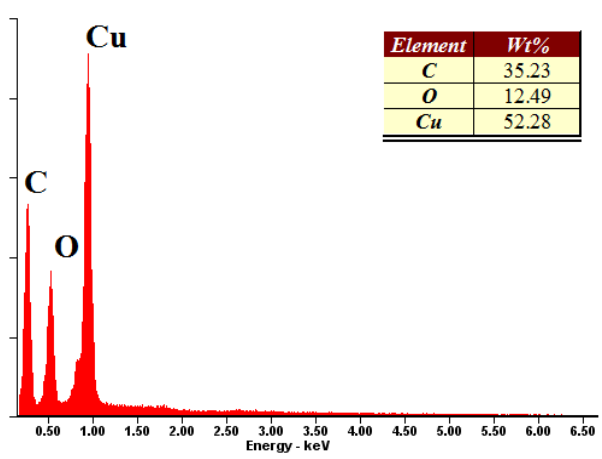

a)

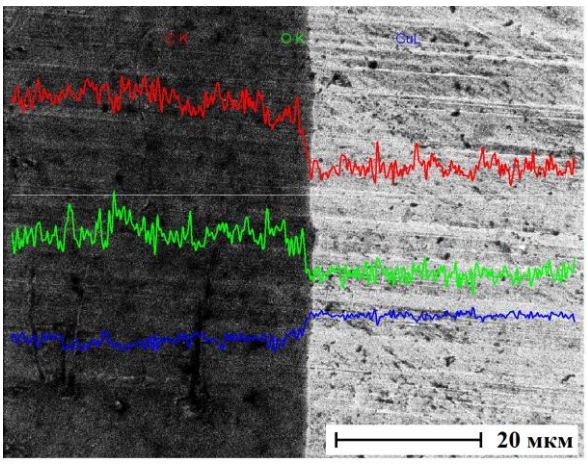

b)

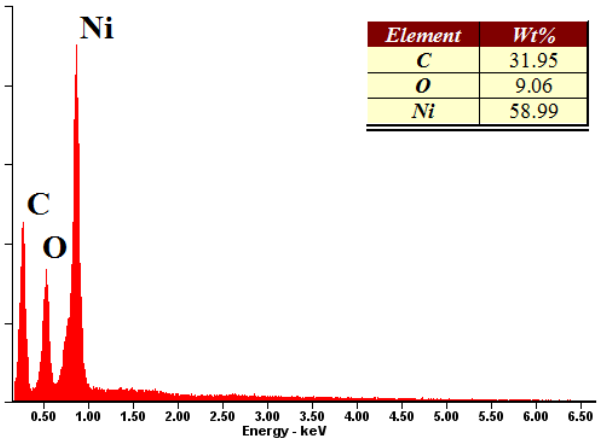

c)

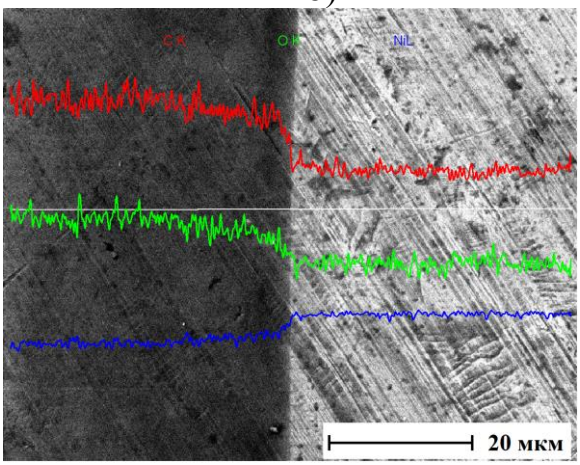

d)

Figure 55 – Elemental analysis of coatings on copper (a) and nickel (c). Element distribution profiles along a horizontal line on copper (b) and nickel (d)

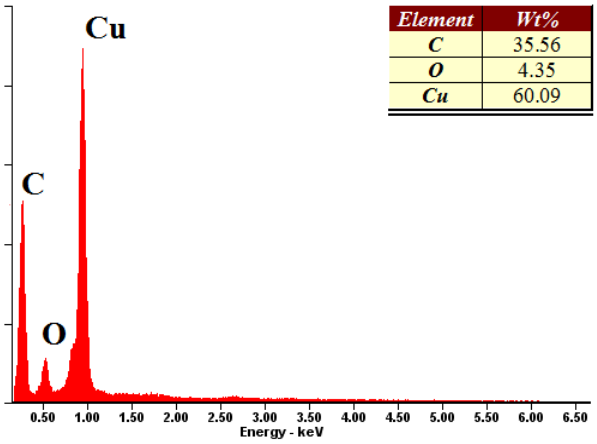

a) copper

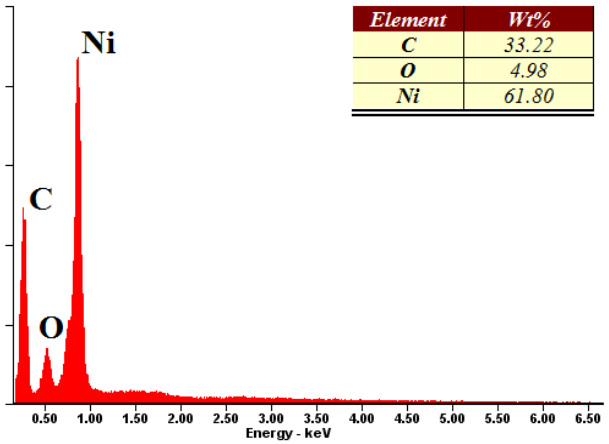

b) nickel

Figure 56 – Elemental composition of coatings after reduction

Experiments have also been conducted to study the adhesion of GO films formed on copper and nickel surfaces by electrophoretic deposition. The resulting

coatings have little adhesion and are easily exfoliated at small bends and partially dissolved in water.

To improve the adhesive properties and water resistance of the coatings, the metal plates with GO coatings were annealed in the flow pipe in the flow of argon-hydrogen mixture (90% Ar + 10% H_2) at a temperature of 200 °C during 2 hours. Figure 57 (a, b) shows microphotographs of the initial surfaces after cleaning copper and nickel respectively. Electrophoretic deposition coatings under the same conditions (U=100V, J=1mA/cm^2, solution concentration 0.1 mg/ml) are shown in figure 57 (c) copper and (d) nickel. Nickel-based coating has more folds than copper. After annealing, the folds at the micro level on both surfaces are smoothed, presumably increasing the interaction surface of the film with the metal surface, with the result that the adhesion properties and durability of anticorrosion protective coatings are improved. Figure 57 (e, f) shows microphotographs of the coatings after annealing and bending to 45°. Thus, this approach provides the necessary adhesion strength of the coating with the metal substrate and can be easily implemented for large-scale use.

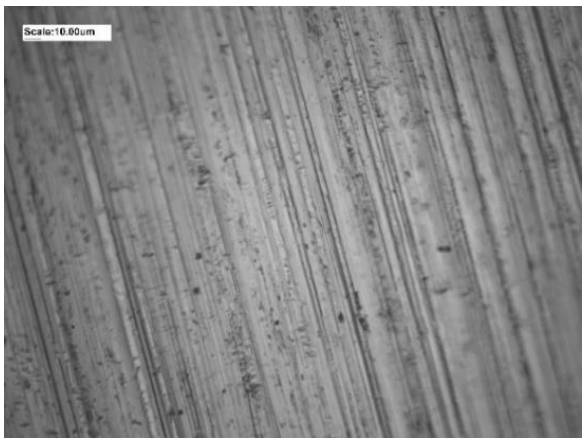

a) the initial surface of the copper foil

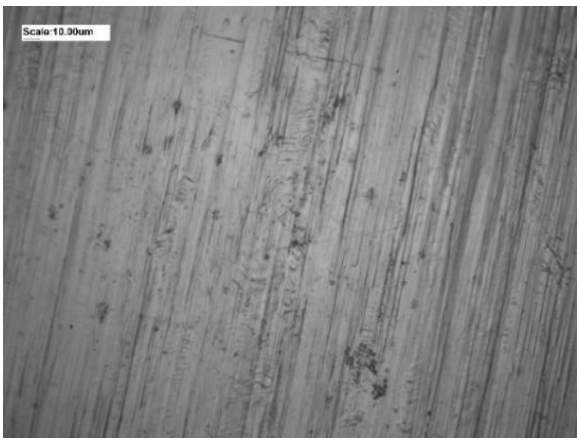

b) the initial surface of the nickel foil

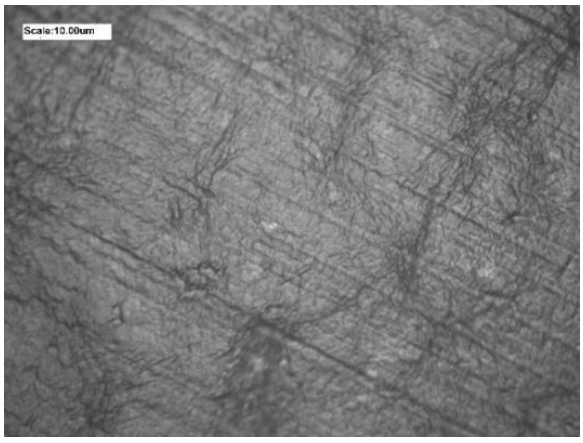

c) graphene oxide coating on copper

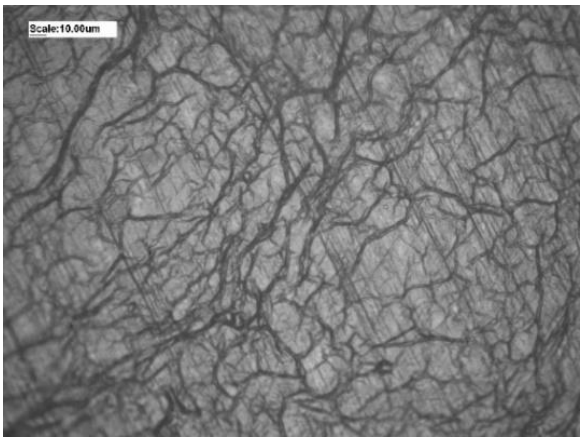

d) graphene oxide coating on nickel

Figure 57 – Optical micrographs of samples before and after application of coatings, page 1

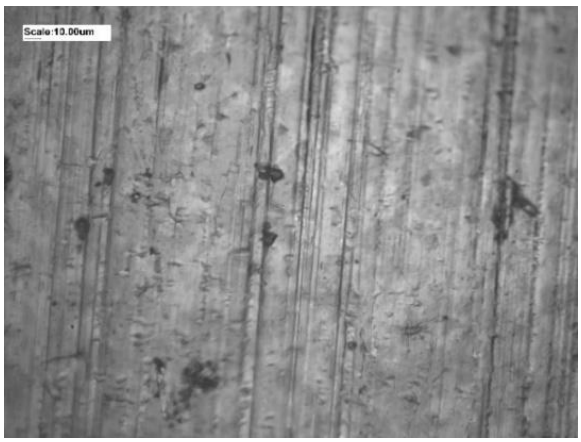

e) graphene oxide coating on copper after annealing and bending

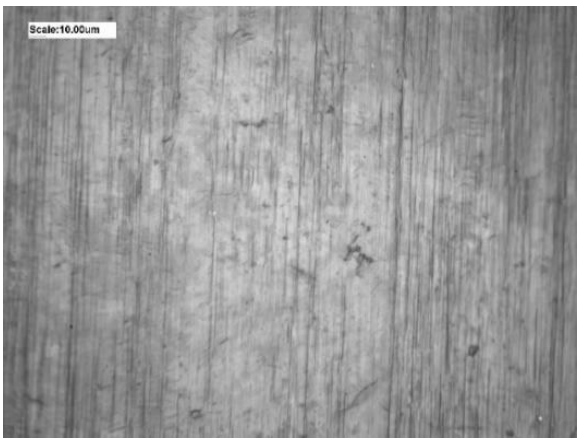

f) graphene oxide coating on nickel after annealing and bending

Figure 57, page 2

3.5 Investigation of the effectiveness of protective coatings based on graphene nanostructures by energy dispersive X-ray spectroscopy (EDS)

Another method of studying the element composition of protective coatings based on graphene nanostructures in our work is the EDS method, which is implemented on the basis of a scanning electron microscope. This method allows to obtain both qualitative and quantitative analysis of the composition of the sample.

The protective properties of graphene coatings formed on copper and nickel plates at temperature (measurement error 1%) were investigated. Before the main work, the copper plates were cleaned in a hydrogen environment. The few-layer graphene nanostructures were then formed on the surface of the copper using the CVD method at T=1000 °C for t=20 min. The D/G ratio can be used to estimate the quality of the obtained coatings [229]. Figure 58 shows the Raman spectrum confirming the presence of few-layer graphene on the copper surface, and has a D/G ≈ 0.08, which indicates a high quality of coatings obtained by CVD method.

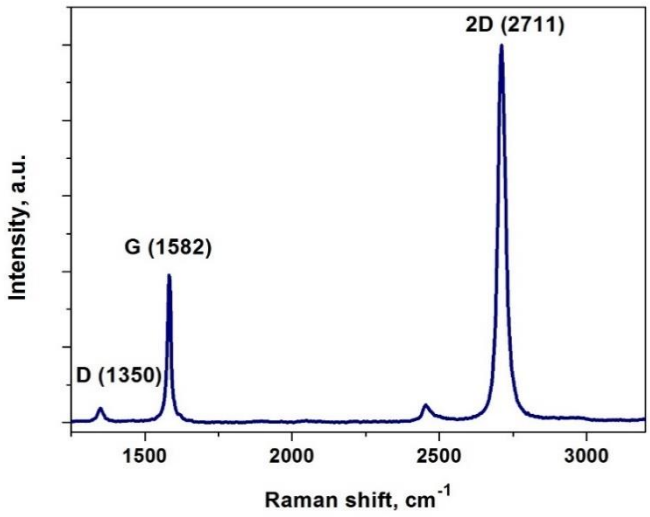

Figure 58 – Raman spectrum of a few-layer graphene on a copper surface

This was followed an elemental analysis by EDS of samples of bare copper (Cu) and graphene-coated copper (G-Cu). The next step was the oxidation of Cu and G-Cu at T=300 °C for 30 minutes in the air atmosphere. The oxidized samples of Cu and G-Cu have been analyzed by EDS. Table 4 shows the results of EDS of Cu and G-Cu before and after oxidation.

Table 4 – EDS results of Cu and G-Cu before and after oxidation

Elements	Cu		G-Cu	
	Before oxidation	After oxidation	Before oxidation	After oxidation
Cu (at. %)	99.93	89.71	67.90	69.70
C (at. %)	0.03	0.02	32.09	30.27
O (at. %)	0.04	10.27	0.01	0.03

Elemental analysis of the obtained samples showed that the graphene film was able to reliably protect the copper plate from oxidation. The oxygen content after oxidation in the Cu sample increased to 10.27 at. % while the amount of oxygen in the G-Cu sample remained almost unchanged. The carbon content of all copper samples has not changed much since oxidation, which allows us to judge that the few-layer graphene coating is temperature-resistant at 300 °C for 30 minutes in the air atmosphere.

We can also confirm the effectiveness of the degree of protection of the graphene coating against oxidation by optically evaluating the differences in color. In Figure 59 we see optical micrographs of Cu and G-Cu after oxidation. Cu, in contrast to G-Cu, acquired a characteristic red-brown color Cu_2O.

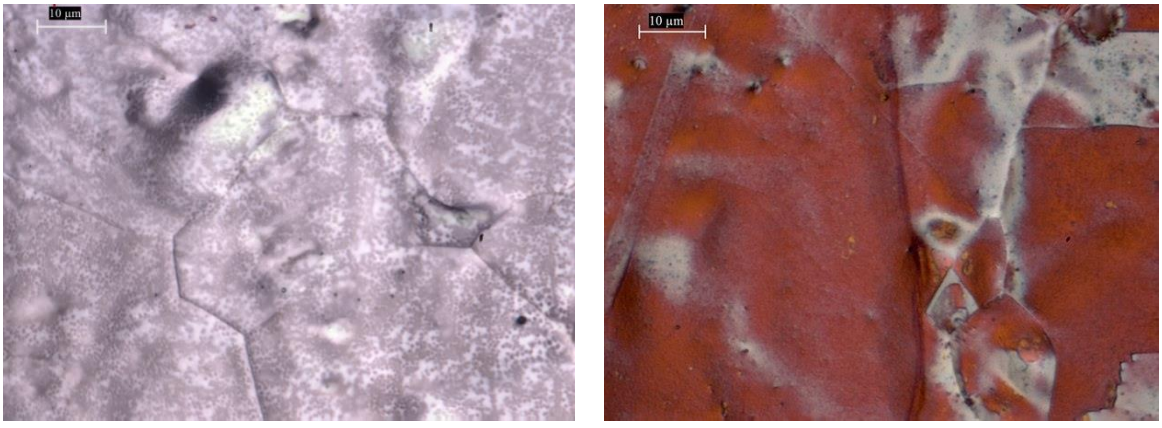

a) G-Cu b) Cu

Figure 59 – Optical micrographs after oxidation

Nickel plates were preliminarily cleaned by vacuum annealing. After that, graphene nanostructures were grown on the nickel surface by the CVD method at T = 1000 °C for 20 min. The Raman spectrum is shown below, confirming the presence of few-layer graphene on the nickel surface (Figure 60).

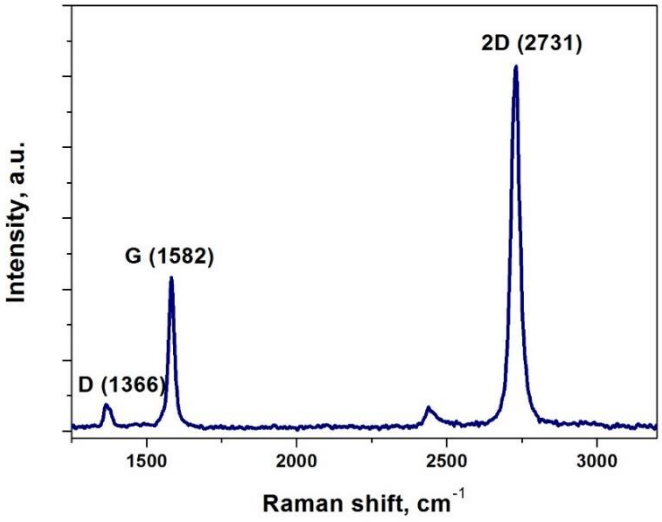

Figure 60 – Raman spectrum of a few-layer graphene on a nickel surface

The next step was the oxidation of bare nickel (Ni) and graphene-coated nickel (G-Ni) at T = 25 °C, 300 °C, 400 °C, 500 °C for t = 10 min in air atmosphere. The obtained samples were analysed by EDS. Based on the quantitative composition of oxygen shown in Figure 61 (a), we determined that G-Ni at T = 25 °C oxidizes 1.2 times slower than Ni, at 300 °C - 1.3 times, at 400 °C - 2.3 times, at 500 °C - 6.0 times. Based on the carbon composition shown in Figure 61(b), we have concluded that as the temperature increases to T = 500°C, a small amount of carbon is burned from the surface of G-Ni. However, the burning of carbon from the G-Ni surface in a given temperature range does not affect the corrosion resistance of the coatings.

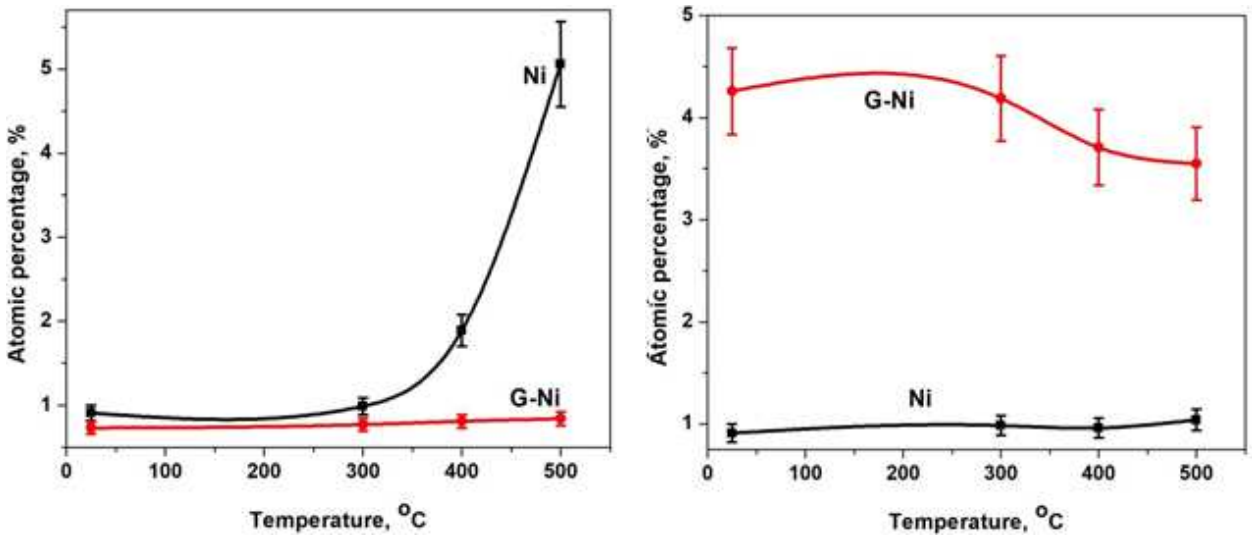

a) quantitative composition of oxygen; b) quantitative composition of carbon

Figure 61– Elemental analysis of Ni and G-Ni

From the optical microphotographs shown in Figure 62, it can be seen that the greatest effect is observed at t = 500 °C, where bare nickel, unlike graphene-coated nickel, has a blue-black color confirming the more intense oxidation of nickel. We can also see an increase in oxidized areas in G-Ni with increasing temperature.

Based on the data obtained, it is clear that the graphene coatings grown directly on copper and nickel plates have excellent protective properties against temperature corrosion in the air atmosphere, which is also presented in our published works [160-165].

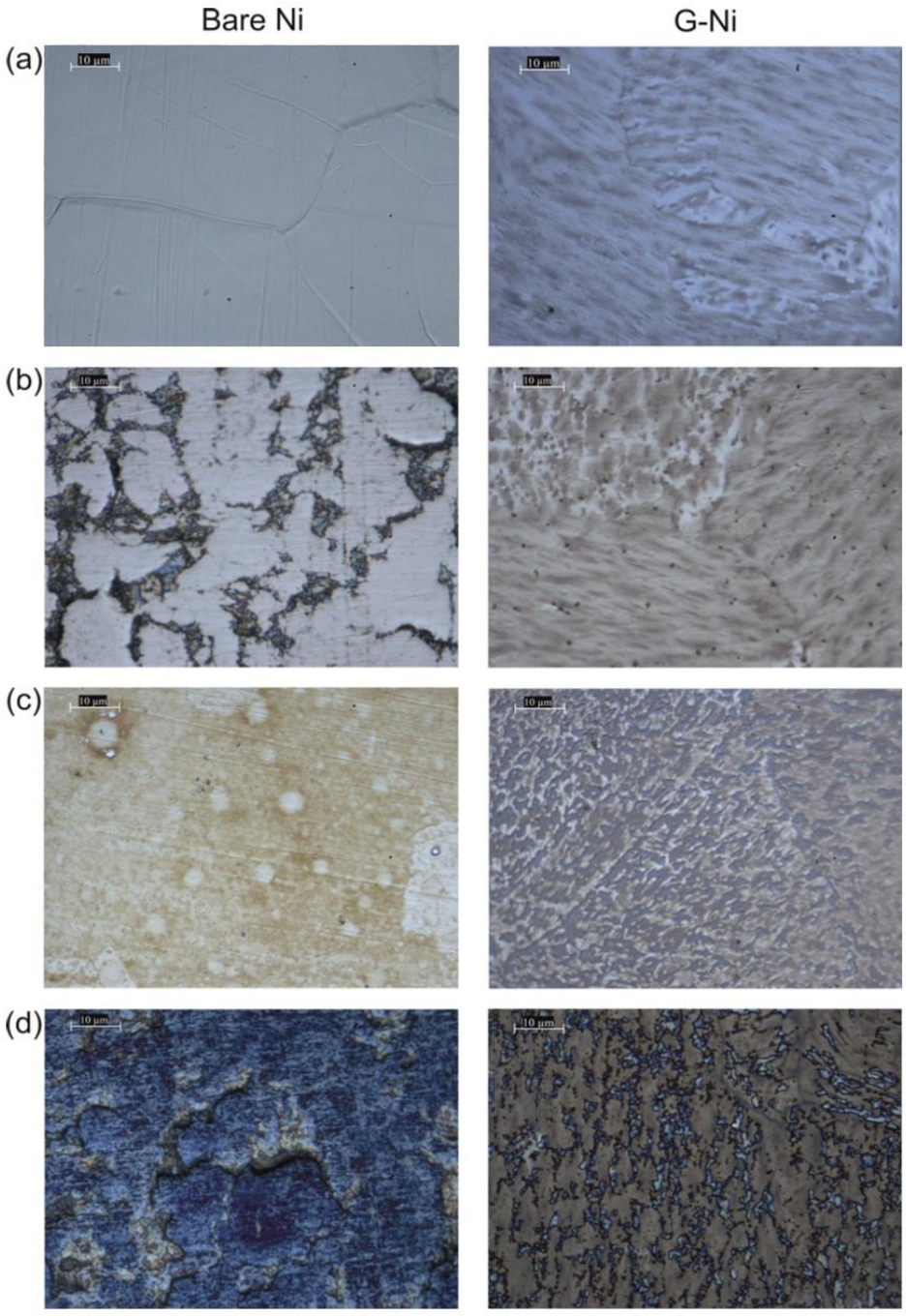

a) t = 25 °C; b) t = 300 °C; c) t = 400 °C; d) t = 500 °C

Figure 62 – Optical micrographs of Ni and G-Ni after oxidation

The effectiveness of the protecting effect of GO against the oxidation of copper and nickel in saline solution was investigated. Prior to the main experimental work and analysis of the EDS spectra, the surface of copper and nickel was pre-cleaned (copper purity: 99.9%, nickel purity: 99.96%) in a 5% nitric acid solution, after which the samples were washed in distilled water and dried. Images of the surface of cleaned copper and nickel plates are shown in electronic microphotographs (Figure 63).

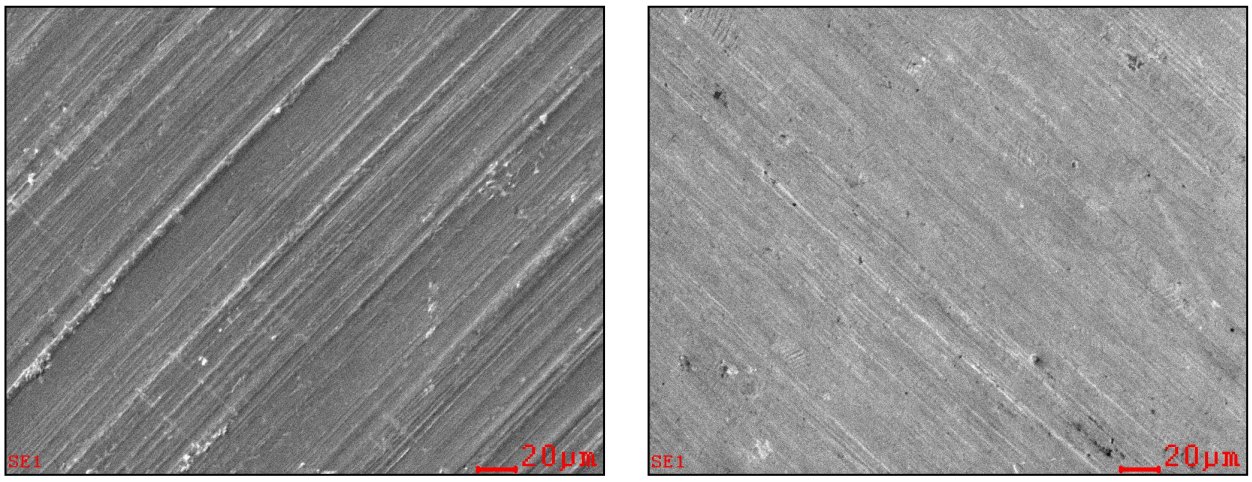

a) b)

a) the surface of copper; b) the surface of nickel

Figure 63 – Electron microscopic images of samples after cleaning

The next stage of the experiment was the deposition of a coating based on GO on the cleaned copper and nickel plates. Protective coatings were applied using GO obtained by functionalization with oxygen-containing functional groups (Hummers' method). The process of obtaining GO, as well as the characterization of the obtained samples, were described earlier.

The obtained protective coatings based on GO were subjected to oxidation in saline solution. To test samples in saline solution, we took water and solution with salt concentration of 3.5%. Copper and nickel plates, as well as copper and nickel plates protected by anticorrosion GO coatings, were exposed to water and 3.5% saline solution for 1 week. The elemental composition of the obtained samples exposed to corrosion was studied by the EDS method. In order to assess the degree of protective effect of GO-coatings against corrosion in water and saline solution, the ratio of the amount of oxygen of the protected surface of copper and nickel plates to the unprotected surface of copper and nickel plates (P Cu,Ni / UP Cu,Ni) was used. The ratio of P Cu,Ni / UP Cu,Ni less than 1 means protective effect. Table 5 shows the results of EDS analysis.

Table 5 – The ratio of quantity of oxygen P Cu,Ni / UP Cu,Ni

Ratio, Oat.%/Oat.%	water	3,5% saline solution
P Cu / UP Cu	0.63	0.77
P Ni / UP Ni	0.89	0.89

As can be seen from the table above, copper and nickel plates coated with dried GO have a protective effect against corrosion in water and 3.5% saline solution.

3.6 Conical Face-Field Electrostatic Energy Analyzer. Experimental study of few-layer graphene by Auger electron spectroscopy (AES)

Among the effective methods for analyzing the composition of nanomaterials, including graphene nanostructures, are methods of surface electron spectroscopy. In this work, for the synthesis of graphene and the subsequent study of the composition and structure under the influence of temperature, a special analytical complex was developed based on the principle of electron spectroscopy of the surface.

Modern electron spectroscopy techniques are widely and effectively used for solving technological and scientific problems in the fast growing area of nanotechnologies [166-184], materials science [185-193], biology[194, 195] plasma and space applications [196-209] etc. Electrostatic energy analyzers are instruments of primary importance for realization of the electron spectroscopy powerful possibilities in different areas and there are many types of them, which were developed for solving various problems. Well known cylindrical mirror systems with modifications [210-217] as well as the numerous types of hemispherical analyzers [218-224], are being the widely used in laboratory conditions when studying surfaces of solid objects with high enough energy and lateral resolution and a certain exact location of them is required. Requirements for energy analyzers are growing and stimulating the creation of new devices. This work presents main design points of calculated models of conical face-field analyzers, with a cone electrostatic field, which have simple design and control, combined with high energy resolution and are practically free of fringing-field distortion effects. They can allow to get almost universal capabilities for the elemental and chemical analysis of objects of different size and forms.

Figure 64 (a,b) presents calculated models of analyzers, with point-to-point focusing. But the analyzer shown on Figure 64 (b) has the point source and focus on the axis of symmetry and focusing length F is equal to the distance SF. The calculated structure of equipotential lines doesn’t show any noticeable fringing-field effect between electrodes. System shown in Figure 64 (a) allows to analyze surface of any remote object and to get the averaged data over some surface area. System shown in Figure 64 (b) allows the point probe application for exploration of a remote object or scanning some small area. As one can see from Figure 64 the focusing field is restricted by the coaxial inner cylinder and truncated-cone electrode with two boundaries, which are perpendicular to the axis of symmetry.

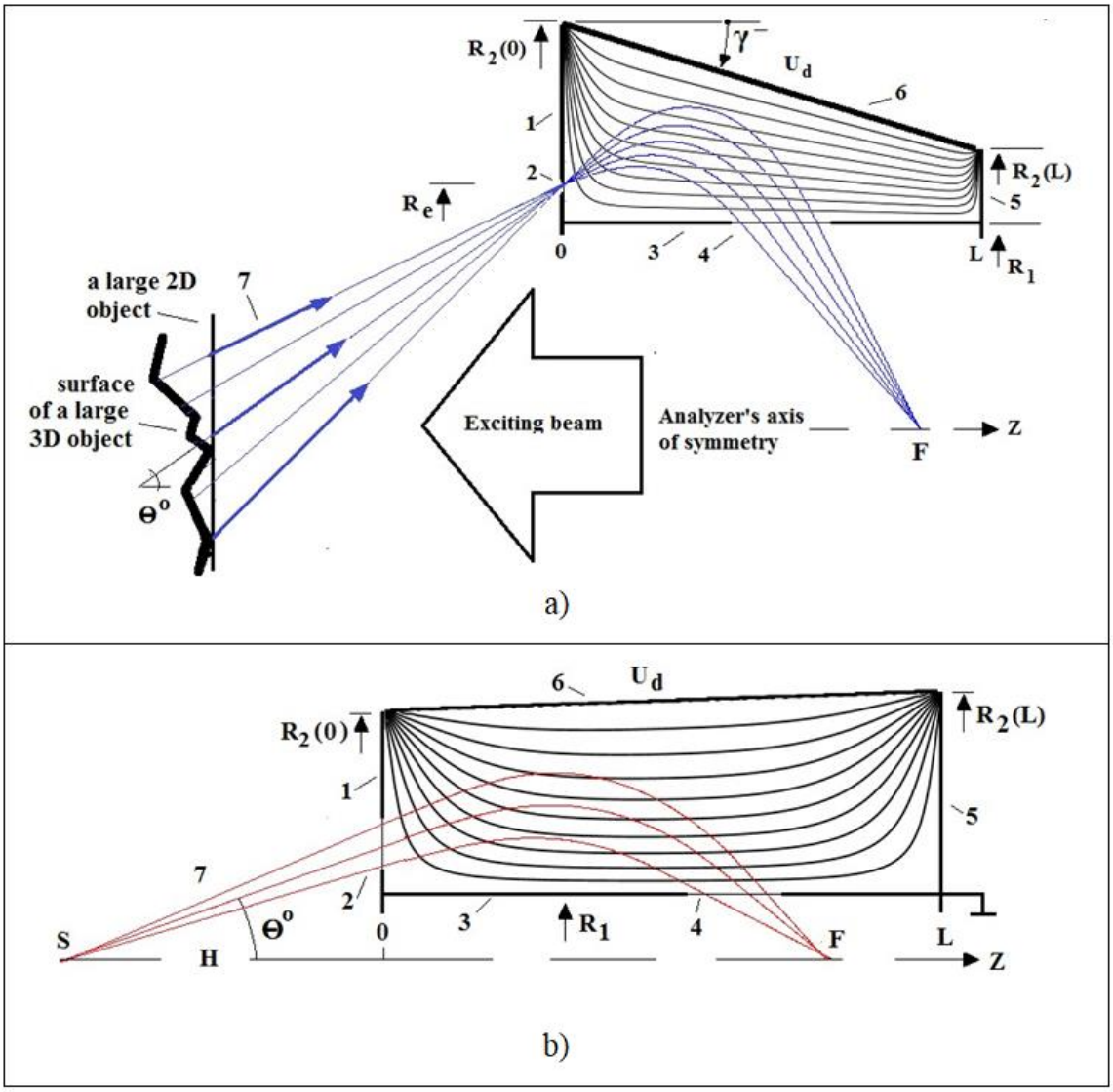

a) The analyzer with a taper conical electrode ($\gamma < 0$). 1 - the front boundary electrode with an entrance annular narrow slit (2), 3- the inner cylindrical electrode with exit slit 4, 5- the rear electrode electrically connected with the inner cylinder, 6 - the outer conical electrode ($\gamma < 0$) with a scanning deflecting potential U_d, 7 - the secondary electrons emitted from different objects; b) 1,2,3, 4,5,7 - the same as that for the (a) configuration, 6 - the conical electrode with $\gamma > 0$

Figure 64 – The schematic typical view of the analyzer's cross section (the upper part) with equipotential lines of the electrostatic focusing field

Mathematically, the generated field is a solution of the Laplace Eq. $\Delta U(R,Z) = 0$, with the boundary conditions $U(R_1, Z) = U(R,0) = U(R,L) = 0$, $U(R_2(Z)) = U_d$, where

$$R_2(Z) = R_2(0) + \gamma Z \qquad (15)$$

In (15) γ - the conicity factor, which can have different signs depending on the direction of the cone. The use of the (15) is justified by well known small angle approximation: tg γ ≈ γ, which is true up to values of about 0.173-0.207 radian (~ 10-12 deg). The radius R_1 of the cylindrical electrode is taken as a unit of length: r = R/R_1 , h = H/R_1 , z = Z/R_1 , l = L/R_1, etc.

$$
\begin{gathered}
U(r,z) = \frac{4 \cdot U_d}{\pi} \cdot \sum_{m=0}^{\infty} \sin(2m+1) \frac{\pi \cdot z}{l} \frac{F_m(r)}{F_m(r_2(z)) \cdot (2m+1)} \\
F_m(r) = I_0(k_m r) K_0(r) - I_0(r) K_0(k_m r) \\
F_m(r_2) = I_0(k_m r_2(z)) K_0(r_2(z)) - I_0(r_2(z)) K_0(k_m r_2(z)) \\
r_2(z) = r_2(0) + \gamma \cdot z \\
k_m = (2m+1)\frac{\pi}{l}
\end{gathered}
\tag{16}
$$

I_0 and K_0 are modified Bessel and Hankel functions, respectively.

In this work some focusing properties for two configurations of the analyzers that use an electrostatic conical field are considered (16), which schematically presented in the Figure 64. An investigations of focusing properties was performed by numerical calculations of trajectories and determining the crossing points. The non- relativistic classical equations of motion in the field (16) are given by (17):

$$
\begin{aligned}
\ddot{z} &= -\frac{e}{m} \cdot \partial U(r,z)/\partial z \\
\ddot{r} &= -\frac{e}{m} \cdot \partial U(r,z)/\partial r
\end{aligned}
\tag{17}
$$

In equations (17) e and m are the charge and mass at rest of a particle. Calculations were performed by using the Runge - Kutta 4th order method with absolute accuracy of the final coordinate about 0.005. The technical details of the numerical computer calculations were basically the same as in the papers published by our team [167, 215, 225].

Here and down the dimensionless parameter G = E_0/eU_d is used, where E_0 - the kinetic energy of charged particles. Typical aberration figures presented in Figure 65 shown the second-order focusing for both analyzer configurations. In Figure 65 (b) data calculated for a cylindrical FFA (γ=0) are also presented (graph 1).

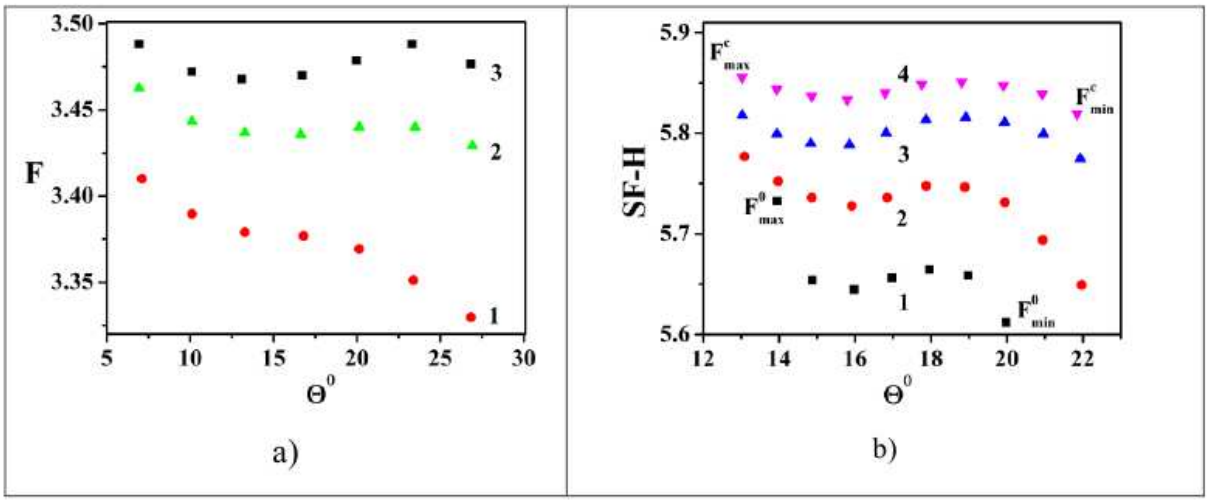

Figure 65 – Aberration figures shown the second order focusing for a set of conicity factors above analyzers. a) G = 2.35, γ< 0, *l* = 5; r_2 (0) = 1.9; 1: γ = -0.076; 2: γ = - 0.045, 3: γ = - 0.04; b) G= 3.42, γ> 0, *l* = 7.0, r_2 (0) = 3.0, h = 4.3; 1: γ=0; 2: γ = 0.012; 3: γ = 0.016, 4: γ=0.020. SF -H is the projection of the part of the trajectory between the first face-electrode and F on the z -axis. Therefore, the analyzer for a remote point source has the focusing length SF = 10.1 for γ=0.020

One can see, that effect of the field conicity allows to improve focusing characteristics. For example, aberration blur for γ = 0.016 and γ = 0.02 is several times less than for γ=0 (cylindrical FFA). Possibly, this is due compensation of the contributions of high-order aberrations in the field (17). It is known that the resolution generally improves with less aberration blur. The parameter K, characterizing the improvement in resolution in comparison with the cylindrical FFA can be written in the form (18) [167].

$$K = \frac{F^0{}_{max} - F^0{}_{min}}{F^c_{max} - F^c_{min}} \tag{18}$$

Figure 66 presents the results of model calculations of energy transmission functions for both analyzer configurations. Light asymmetry is possibly coased with a complicate shape of these electrostatic fields, which is more related to the configuration presented in Figure 64 (b).

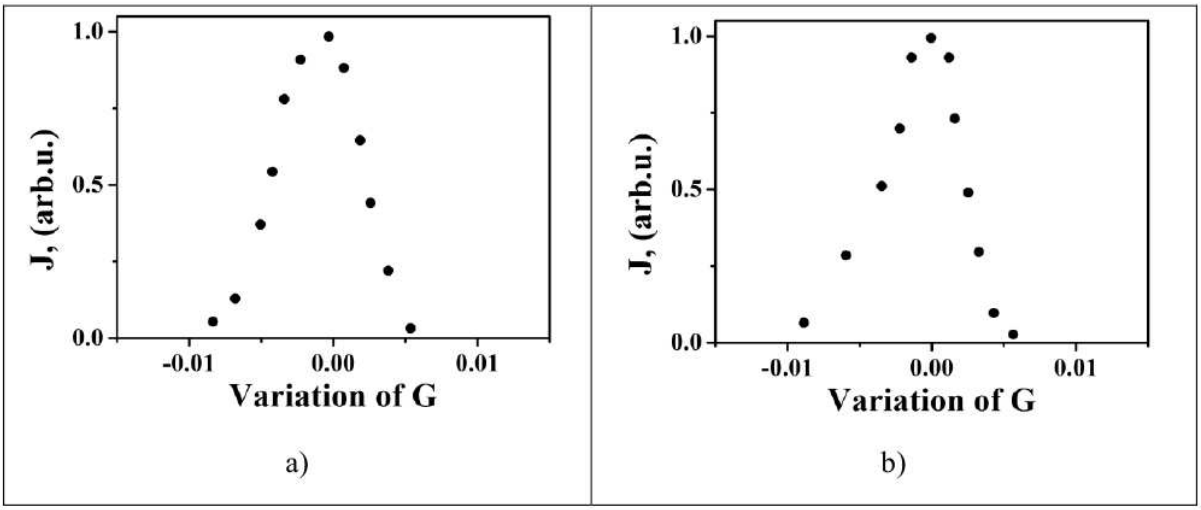

a) See Figure 64 (a): γ = - 0.045, G = 2.35; b) Figure 64 (b): γ = 0.020, G = 3.42

Figure 66 – The energy transmission functions J of the presented analyzers

The dispersion of these systems were calculated by using the expression (19).

$$D_E = (\frac{\Delta z}{\Delta E}) \cdot E \tag{19}$$

where Δz were the finite segments obtained by trajectory for the small energy shift ΔE. According to (19) D_E was estimated to be on average as large as 5.1 for the Figure 64 (a) - configuration and nearly 5.3 for the 64 (b) - configuration. For numerical calculations the energy resolution is commonly defined as $R_E = (D_E/\Delta z)^{-1}$ where Δz is a projection of the part of the aberration figure around a central point on the F axis. For example, the typical value of resolution for the analyzer Fig. 64 (a) may be estimated from the data in Figure 65 (a) (graph 3): $R_E \approx 0.71$ %. For the analyzer Fig. 64 (b): Fig. 65 (b) (graph 4) $R_E \approx 0.60$ %.

The focusing properties of a new type electrostatic energy analyzers on the base of a conical face-field, were numerically calculated. Results demonstrated the sharp enough second-order focusing as well as the good acceptance characteristics by analyzing remote objects of different shape and size and indicate the absence of fringing-fields. Analyzers allow to obtain the data averaged over the irradiated area or to perform a point analysis of the object surface [226]. Figure 67 shows the appearance of an energy analyzer for nanomaterials research.

Composition measurement by Auger method (C,N,S and Ni) has a sensitivity of about 0.1%. Figure 68 shows a typical experimental Auger spectrum obtained when testing a new energy analyzer on a stainless-steel substrate, which indicates the high resolution of the analyzer, the fine structure of the carbon Auger peak is clearly visible.

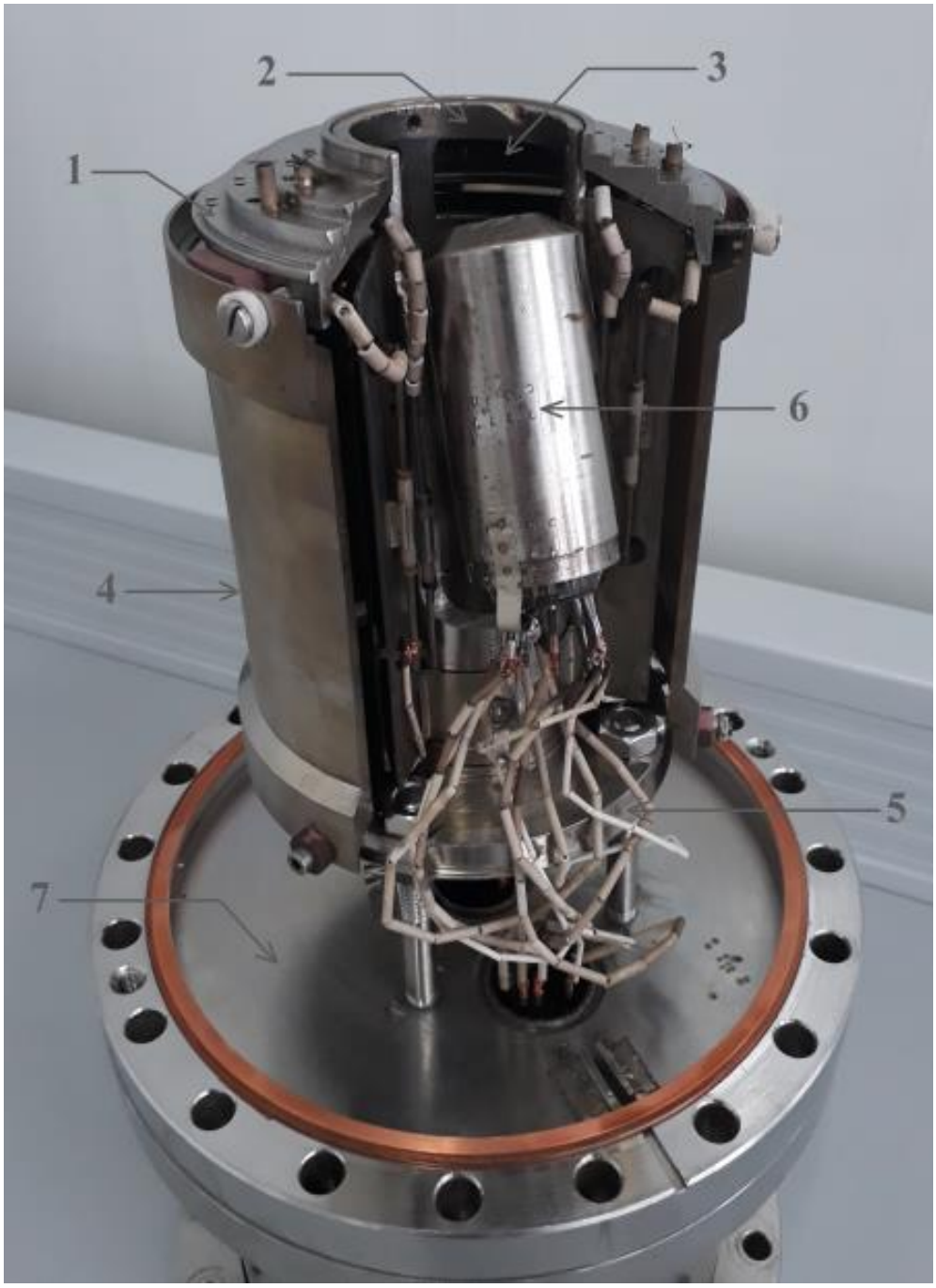

1- face electrode, 2- inner cylindrical electrode, 3- inlet window, 4- external cylindrical electrode, 5- back electrode, 6- electron gun, 7- high vacuum flange

Figure 67 – External view of the energy analyzer

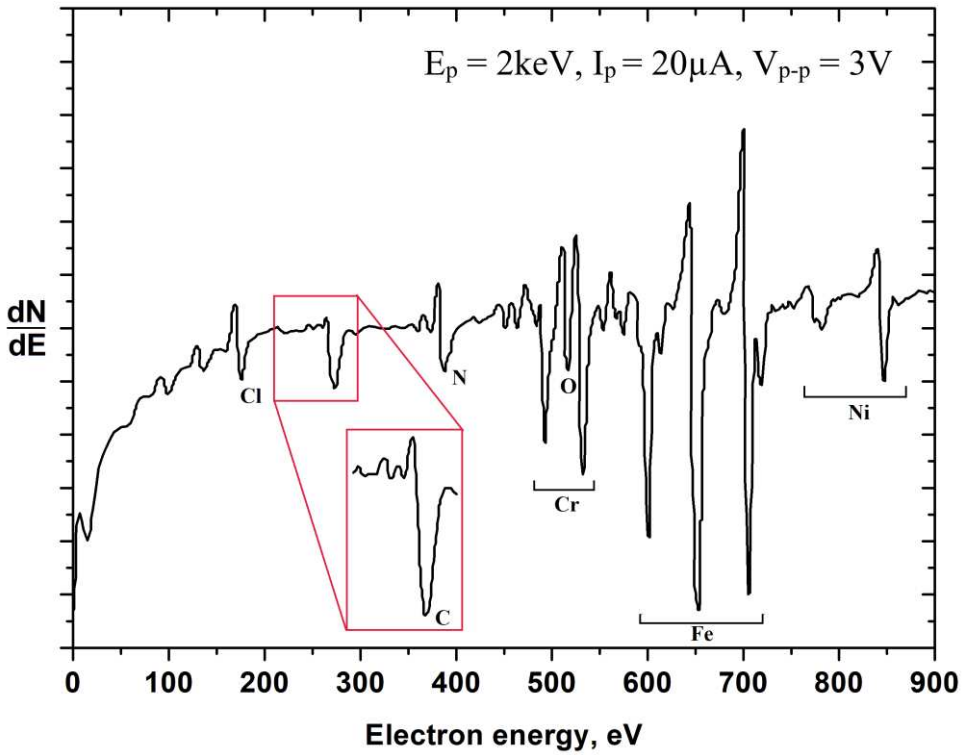

Figure 68 – Typical experimental Auger spectrum

Figure 69 shows the practical results obtained by using the useful properties of the analyzer, in particular, the possibility of modifying the front electrode. A system for growing graphene nanostructures was implemented in the analytical ultrahigh-vacuum chamber of the Auger spectrometer. Growth was carried out by diffusion of carbon through nickel foil (purity 99.99%), 100 μm thick, followed by controlled formation of few-layer graphene nanostructures from the side of the analyzed surface. The carbon source was a flat sample of HOPG, which was tightly pressed to the nickel foil from the reverse side. The sample with the foil was heated to a temperature of ≈ 1100 °C, which was maintained for the time required for the formation of atomically thin layers of graphene at a chamber pressure of 10^{-5} Pa. Further, after cooling the system and restoring the vacuum to the level of 10^{-7} Pa, the Auger spectrum was recorded.

Figure 69 (a) shows the Auger spectrum obtained from nickel foil after annealing in an ultrahigh vacuum chamber, the spectrum shows that sulfur segregation is observed on the surface (a-black curve). (a-red curve) - Auger spectrum obtained from nickel foil after the formation of few-layer graphene nanostructures, where an intense carbon peak appeared in the form of few-layer graphene against the background of a series of nickel peaks and a sulfur peak. The presence of nickel peaks in the spectrum (a-red curve) indicates the formed atomically thin layers of graphite. Figure 69(b) shows the Raman spectrum of the same sample, which confirms the presence of few-layer graphene structures. The presence of the D peak indicates the imperfection of the obtained structures, including due to the possible functionalization of graphene nanostructures with sulfur.

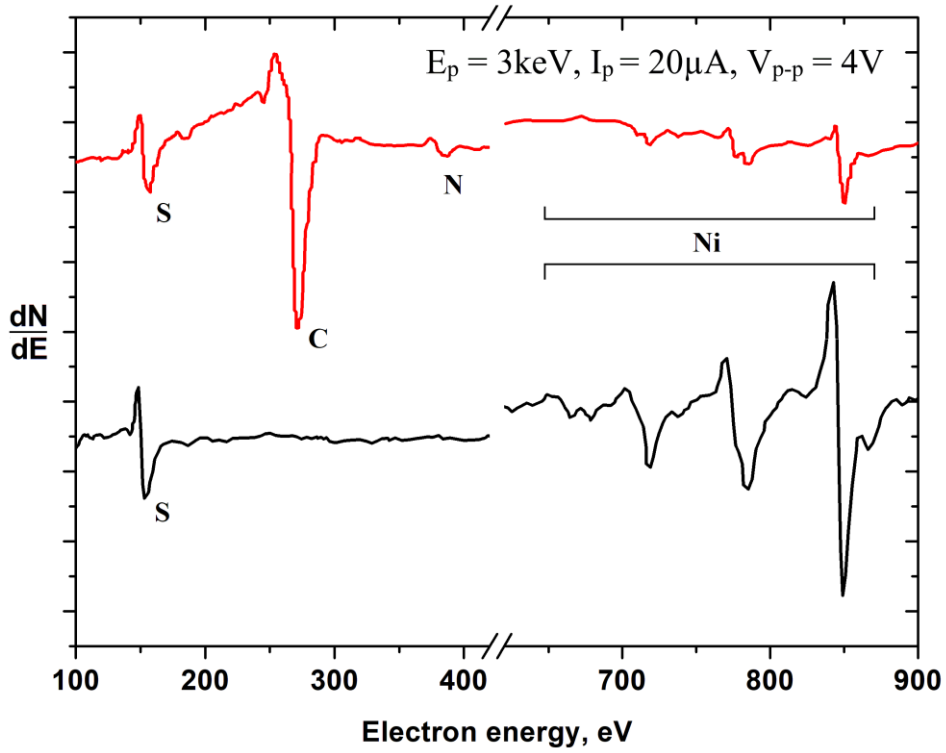

a)

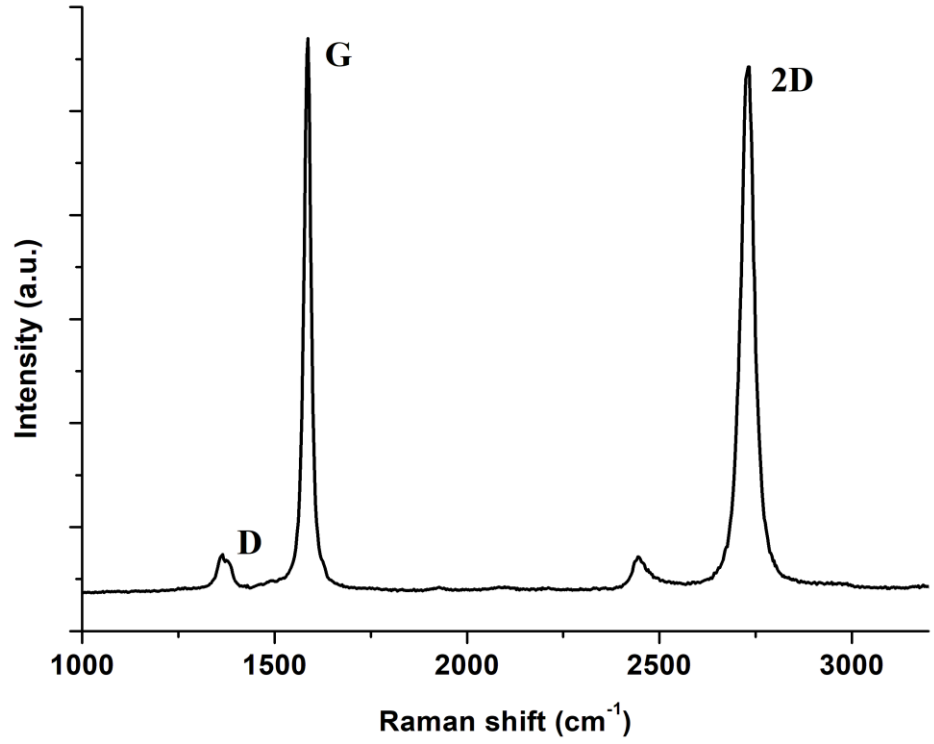

b)

Figure 69 – a) Auger spectrum obtained from nickel foil after annealing in a UHV chamber; b) Raman spectrum of the same sample, which confirms the presence of few-layer graphene nanostructures

According to the results of the thesis work, it was found that under the conditions of ultrahigh vacuum at the USU-4 unit it is possible to synthesize graphene by diffusion method and in situ control their composition and structure using the created Conical Face-Field Electrostatic Energy Analyzer.

Conclusions for section 3

As the main methods of obtaining graphene in this thesis were chosen: CVD and diffusion method. Obtaining graphene coating by CVD method was carried out in a sealed flow tube with the diameter of 80 mm. A 100 μm-thick nickel plate of 99.99% purity was used as a catalyst substrate for graphene growth. Argon-hydrogen mixture was passed as a buffer gas and benzene vapor was used as a carbon source. Method for transferring ultrathin layers of graphite and graphene to the surface of other materials and substrates was also developed by wet etching. This method makes it easy to transfer graphene to the desired surfaces of various materials. Graphene and few-layer graphene nanostructures were grown on polycrystalline nickel substrates by the method of carbon diffusion through nickel on the vacuum setup (VUP-5M).

Experiments on obtaining FGNS were carried out in this work. One of the methods of functionalization of graphene is irradiation. Few-layer graphene nanostructures obtained in the process of carbon diffusion through nickel were irradiated with low-energy gallium ions on a dual-beam scanning electron microscope with a built-in gallium gun. The energy dispersive spectrum after irradiation shows the appearance of a small gallium peak. One of the most prominent representatives of FGNS is GO due to its potential applications in various fields of science and technology. In this work, GO was obtained chemically (modified Hummers' method).

Formation of protective coatings based on GO on Cu and Ni surfaces was carried out by electrophoretic deposition. In this work the negative electrode is a platinum foil, and the positive electrode, on which the graphene oxide film is formed, is copper and nickel with an applied potential of 100 V. Also, experiments were carried out to study the adhesive properties of GO films formed on copper and nickel surfaces by electrophoretic deposition. The coatings obtained this way have insignificant adhesion and easily peel off at small bends and partially dissolve in water. To improve the adhesion properties and water resistance of the coatings, metal plates with GO coatings were annealed in a flow tube in a stream of argon-hydrogen mixture (90% Ar + 10% H_2) at 200 °C for 2 hours.

In this part of the work were carried out experiments to study the effectiveness of anticorrosion protective coatings based on graphene nanostructures under the influence of external factors. Protective properties of graphene coatings, formed on copper and nickel plates by CVD method were investigated under the temperature influence. Elemental analysis of obtained samples showed the effectiveness of the protection of copper and nickel plates from thermal oxidation. The effectiveness of the protective action of GO against oxidation of copper and nickel in saline solution was also investigated. Copper and nickel plates coated with GO have a protective effect against corrosion in water and 3.5% saline solution.

This thesis presents main design points of calculated models of conical face-field analyzers, with a cone electrostatic field, which have simple design and control, combined with high energy resolution and are practically free of fringing-field distortion effects. They can allow to get almost universal capabilities for the elemental and chemical analysis of objects of different size and forms. It was found that under the conditions of ultrahigh vacuum at the USU-4 unit it is possible to synthesize graphene by diffusion method and in situ control their composition and structure using the created Conical Face-Field Electrostatic Energy Analyzer.

CONCLUSION

1. As the thesis work was carried out, the computer models were created and the calculations of the barrier properties of graphene against oxygen penetration were performed using the commercial software package DMol3, which uses the DFT method. The computer simulations and calculations showed the presence of a high potential barrier for the oxygen molecule penetration through the graphene, even in the presence of structural defects (vacancy, divacancy and small gap) in it. The results of computer simulation suggests that graphene is a very effective anticorrosion coating.

2. Computer models and quantum-mechanical calculations show that the functionalization by gallium atoms of the graphene coating, which has a sufficiently large gap between the sheets (0.45 nm), retains the ability of effective protection due to a significant reconfiguration of the gap-blocking chain of gallium atoms and their high chemisorption ability to capture oxygen molecules.

3. During the implementation of thesis work, ways of production of graphene nanostructures by different methods, including obtaining graphene by CVD and carbon diffusion through nickel, obtaining graphene oxide by Hummers' method, functionalization of few-layer graphene with gallium ions at low energy and low doses were worked out. The results of a comprehensive study of the obtained samples of graphene nanostructures using Raman spectroscopy, electron microscopy, EDS and optical microscopy show the high quality of graphene nanostructures. The graphene transfer technique was also developed.

4. A technique of electrophoretic deposition of graphene oxide on copper and nickel surfaces at the same deposition mode, but at different times in order to control the coating thickness was developed. It has been found that GO films deposited by electrophoretic deposition on copper and nickel substrates have low adhesion strengths and solubility in water. To increase the adhesive strength and reduce the solubility in water, annealing of metal plates with GO coatings in an argon-hydrogen medium was implemented.

5. The results of the study of the elemental composition of the obtained CVD-graphene samples show reliable protection against temperature corrosion. The oxygen content after oxidation at T = 300 °C for 30 minutes in the air atmosphere in the Cu sample increased significantly, while for G-Cu it changed insignificantly. According to the elemental composition results, G-Ni at T = 25 °C oxidized 1.2 times slower than Ni, at 300 °C - 1.3 times, at 400 °C - 2.3 times, at 500 °C - 6.0 times for a temperature exposure time of 10 min in the air atmosphere. A study of the effects of water and 3.5% saline solution for 1 week on the corrosion resistance of copper and nickel substrates coated with GO showed a protective effect.

6. Numerical calculations of focusing properties of a new type electrostatic energy analyzers on the base of a conical face-field were carried out. The results demonstrated sharp enough second-order focusing, as well as the good acceptance characteristics by analyzing remote objects of different shape and size. Due to the simple and convenient design this energy analyzer allows to analyze the graphene

nanostructures directly in the growth chamber. During the testing of a new specialized Auger-analyzer in the work were obtained Auger spectra of nickel foil after the formation on it the anticorrosion protective coatings based on few-layer graphene nanostructures. Thanks to the proposed unique AES method in this thesis work became possible the sensitive analysis to light elements of thin near-surface layers of various materials, which can become an indispensable method of analysis in nanotechnology and materials science.

REFERENCES

1 Jones D.A. Principles and Prevention of Corrosion. – 2nd Edition. – Publisher: Prentice Hall, 1996. – 572 p.

2 Lyon S. Shreir's Corrosion / Edited by Richardson T., Cottis B., Lindsay R, Scantlebury D., Stott H., Graham M. – 4th Edition. – Publisher: Elsevier BV, 2010. – 3450 p.

3 Web-Resource, Wet and Dry Corrosion. https://www.unsw.edu.au/science/our-schools/materials/engage-with-us/high-school-students-and-teachers/online-tutorials/corrosion/introduction/wet-and-dry-corrosion 02.09.2022.

4 Hansson C.M. The Impact of Corrosion on Society // Metallurgical and Materials Transactions A. – October 2011. – Vol. 42, № 10. – P.2952-2962.

5 Marcus P., Maurice V. The Structure of Passive Films on Metals and Alloys. In Passivity of Metals and Semiconductors / Edited by Ives M.B., Luo J.L., Rodda J.R. – The Electrochemical Society, Jasper Park Lodge, Canada, 1999. – P. 30-64.

6 Örnek C., et al. In-situ synchrotron GIXRD study of passive film evolution on duplex stainless steel in corrosive environment // Corros. Sci. – 2018. – Vol. 141. – P. 18-21.

7 Schmuki P., Böhni H. Metastable pitting and semiconductive properties of passive films // J. Electrochem. Soc. – 1992. – Vol. 139. – P. 1908-1913.

8 Koch G., Varney J., Thompson N., Moghissi O., Gould M., Payer J. International Measures of Prevention, Application, and Economics of Corrosion Technologies Study // NACE International – 2016. – P. 3.

9 Witcher T.R. From Disaster to Prevention: The Silver Bridge // Civil Engineering Magazine. – 2017. – Vol. 87, № 11. – P. 44-47.

10 Eckerman I. The Bhopal gas leak: Analyses of causes and consequences by three different models // Journal of Loss Prevention Process Industry. – 2005. – Vol. 18, № 2. – P. 213-17.

11Kumar S. India: the second Bhopal tragedy // The Lancet. – 1993. – Vol. 341, № 8854. – P. 1205-06.

12 Broughton E. The Bhopal disaster and its aftermath: a review // Environ Health. – 2005. – Vol. 4, № 1. – P. 1-6.

13 Web-Resource, Bhopal Plant Disaster – Situation Summary. https://www.umass.edu/sts/pdfs/Bhopal_Complete.pdf 03.09.2022.

14 Web-Resource, Union Carbide fabriek Giframp 3 december 1984 (Bhopal). http://wikimapia.org/319979/nl/Union-Carbide-fabriek-Giframp-3-december-1984 04.09.2022.

15 Davis J.R. The Effects and Economic Impact of Corrosion // In: Corrosion: Understanding the Basics. – Publisher: ASM International, 2000. – P. 1-20.

16 Sørensen P.A., et al. Anticorrosive coatings: a review // Journal of Coatings Technology and Research. – 2009. – Vol. 6, № 2 – P. 135-176.

17 Revie R.W., Uhlig H.H. Corrosion and Corrosion Control: An Introduction to Corrosion Science and Engineering. – 4th Edition. – Publisher: John Wiley & Sons, 2008. – 490 p.

18 Kesavan D., Gopiraman M., Sulochana N. Green inhibitors for corrosion of metals: A Review // Chemical Science Review and Letters. –2012. – Vol. 1, № 1. – P. 1-8.

19 Juchniewicz R, Jankowski J, Darowicki K. Cathodic and Anodic Protection // Materials Science and Technology: A Comprehensive Treatment: Corrosion and Environmental Degradation. – 2000. – P. 453.

20 Chen X.B., Birbilis N., Abbott T.B. Review of Corrosion-Resistant Conversion Coatings for Magnesium and Its Alloys // Corrosion. – 2011. – Vol. 67, № 3. – P. 035005.

21 Presuel-Moreno F., Jakab M.A., Tailleart N., Goldman M., Scully J.R. Corrosion-resistant metallic coatings // Materials Today. – 2008. – Vol. 11. – P. 14-23.

22 Podchernyaeva I.A., Panasyuk A.D., Teplenko M.A., Podol'skii V.I. Protective Coatings on Heat-Resistant Nickel Alloys // Powder Metallurgy and Metal Ceramics. – 2000. – Vol. 39, № 9-10– P. 434-444.

23 Taylor S.R., Shiflet G.J., Scully J.R., Buchheit R.G., VanOoij W.J., Sieradzki K., Diaz R.E., Brinker C.J., Moran A.L. Corrosion Reviews. – Publisher: De Gruyter, 2007. –Vol. 25, № 5-6 – P. 491.

24 Wallace P.R. The band theory of graphite // Phys. Rev. – 1947. – Vol. 71. – P. 622-634.

25 McClure J.W. Diamagnetism of graphite // Phys. Rev. – 1956. – Vol. 104. – P. 666-671.

26 Slonczewski J.C., Weiss P.R. Band structure of graphite // Phys. Rev. – 1958. – Vol. 109. – P. 272-279.

27 Semenoff G.W. Condensed-matter simulation of a three-dimensional anomaly // Phys. Rev. Lett. – 1984. – Vol. 53. – P. 2449-2452.

28 Fradkin E. Critical behavior of disordered degenerate semiconductors // Phys. Rev. B – 1986. – Vol. 33. – P. 3263-3268.

29 Haldane F.D.M., Model for a quantum Hall effect without Landau levels: Condensed-matter realization of the “parity anomaly”. // Phys. Rev. Lett. – 1988. – Vol. 61. – P. 2015-2018.

30 Geim A.K., Novoselov K.S. The rise of graphene // Nat. Mater. – 2007. – Vol. 6.– P. 183-191.

31 Novoselov K.S., Geim A.K., Morozov S.V., Jiang D., Zhang Y., Dubonos S.V., Grigorieva I.V., Firsov A.A. Electric field effect in atomically thin carbon films // Science. – 2004. – Vol. 306 – P. 666-669.

32 Novoselov K.S., Jiang D., Schedin F., Booth T.J., Khotkevich V.V., Morozov S.V., Geim A.K. Two-dimensional atomic crystals // Proc. Natl. Acad. Sci. USA. – 2005. – Vol. 102. – P. 10451-10453.

33 Zhu H. Graphene Fabrication, Characterizations, Properties and Applications. – 1st Edition. – Publisher: Elsevier, 2017. – 272 p.

34 Allen M.J., Tung V.C., Kaner R.B. Honey comb graphene: A review of graphene // Chem. Rev. – 2010. – Vol. 110. – P. 132-145.

35 Web-Resource, Graphene: The Sustainable Technology of the Future. https://thecatalystnews.com/2013/10/11/graphene-the-sustainable-technology-of-the-future/ 20.10.2022.

36 Web-Resource, Graphene Overview. https://avadaingraphene.com/graphene-overview/ 20.10.2022.

37 Lee C., Wei X., Kysar J.W., Hone J. Measurement of the elastic properties and intrinsic strength of monolayer graphene // Science – 2008. – Vol. 321. – P. 385-388.

38 Balandin A.A., Ghosh S., Bao W., Calizo I., Teweldebrhan D., Miao F., Lau C.N. Superior thermal conductivity of single-layer graphene // Nano Lett. – 2008. – Vol. 8. – P. 902-907.

39 Bolotin K.I., Sikes K.J., Jiang Z., Klima M., Fudenberg G., Hone J., Kim P., Stormer H.L. Ultrahigh electron mobility in suspended graphene // Solid State Commun. – 2008. – Vol. 146. – P. 351-355.

40 Stoller M.D., Park S., Zhu Y., An J., Ruoff R.S. Graphene-based ultracapacitors // Nano Lett. – 2008. – Vol. 8. – P. 3498-3502.

41 Zhang Y., Tan Y.-W., Stormer H.L., Kim P. Experimental observation of the quantum Hall effect and Berry's phase in graphene // Nature. – 2005. – Vol. 438. – P. 201-204.

42 Geim A.K. Nobel lecture: random walk to graphene // Rev Mod Phys. – 2011. – Vol. 83, № 3. – P. 851-862.

43 Hernandez Y., Nicolosi V., Lotya M., Blighe F.M., Sun Z., De S., et al. High-yield production of graphene by liquid-phase exfoliation of graphite // Nat Nanotechnol. – 2008. – Vol. 3. – P. 563-8.

44 Niu L., Coleman J.N., Zhang H., Shin H., Chhowalla M., Zheng Z. Production of two-dimensional nanomaterials via liquid-based direct exfoliation // Small. – 2016. – Vol. 12, № 3. – P. 272-93.

45 Munuera J.M., Paredes J.I., Enterría M., et al. Electrochemical exfoliation of graphite in aqueous sodium halide electrolytes toward low oxygen content graphene for energy and environmental applications // ACS Applied Materials & Interfaces. – 2017. – Vol. 9, № 28. – P. 24085-24099.

46 Hossain S.T., Wang R. Electrochemical exfoliation of graphite: Effect of temperature and hydrogen peroxide addition // Electrochimica Acta. – 2016. – Vol. 216. – P. 253-260.

47 Singh R., Tripathi C.C. Electrochemical exfoliation of graphite into graphene for flexible supercapacitor application // Materials Today-Proceedings. – 2018. – Vol. 5, № 1. – P. 1125-1130.

48 Wang H., Wei C., Zhu K., et al. Preparation of graphene sheets by electrochemical exfoliation of graphite in confined space and their application in transparent conductive films // ACS Applied Materials & Interfaces. –2017. – Vol. 9, № 39. – P. 34456-34466.

49 Stankovich S., Dikin D.A., Piner R.D., Kohlhaas K.A., Kleinhammes A., Jia Y., et al. Synthesis of graphene-based nanosheets via chemical reduction of exfoliated graphite oxide // Carbon. – 2007. – Vol. 45, № 7. – P. 1558-65.

50 Chen W., Yan L., Bangal P. Chemical reduction of graphene oxide to graphene by sulfur-containing compounds // J Phys Chem C. – 2010. – Vol. 114, № 47. – P. 19885-90.

51 Aunkor M.T.H., Mahbubul I.M., Saidur R., et al. The green reduction of graphene oxide // RSC Advances. – 2016. – Vol. 6, № 33. – P. 27807-27828.

52 Ortega-Amaya R., Matsumoto Y., Díaz-Torres E., et al. Green routes for graphene oxide reduction and self-assembled graphene oxide micro- and nanostructures production. Graphene Materials - Structure, Properties and Modifications / Edited by Kyzas G.Z., Mitropoulos A.C. – Chapter 6. – Publisher: InTechOpen – 2017. – P. 129-151.

53 De Silva K.K.H., Huang H.H., Joshi R.K., et al. Chemical reduction of graphene oxide using green reductants // Carbon. – 2017. – Vol. 119. – P. 190-199.

54 Куанышбеков Т.К., Тулегенова М.А., Гусейнов Н.Р., Билл Г., Ильин А.М. Получение графена диффузией графита // Вестник КазНИТУ. – 2018. - № 3 (127). – С. 152-158.

55 Srivastava A., Galande C., Ci L., Song L., Rai C., Jariwala D., et al. Novel liquid precursor-based facile synthesis of large-area continuous, single, and few-layer graphene films // Chem Mater. – 2010. – Vol. 22, № 11. – P. 3457-61.

56 Dong X., Wang P., Fang W., Su C.-Y., Chen Y.-H., Li L.-J., et al. Growth of large-sized graphene thin-films by liquid precursor-based chemical vapor deposition under atmospheric pressure // Carbon. – 2011. – Vol. 49, № 11. – P. 3672-8.

57 Bae S., Kim H., Lee Y., Xu X., Park J.-S., Zheng Y., et al. Roll-to-roll production of 30-inch graphene films for transparent electrodes // Nat Nanotechnol. – 2010. – Vol. 5, № 8. – P. 574-8.

58 Fauzi F.B., Ismail E., Ani M.H., et al. A critical review of the effects of fluid dynamics on graphene growth in atmospheric pressure chemical vapor deposition // Journal of Materials Research. – 2018. – Vol. 33, № 9. – P. 1088-1108.

59 Raccichini R., Varzi A., Passerini S., Scrosati B. The role of graphene for electrochemical energy storage // Nat Mater. – 2015. – Vol. 14, № 3. – P. 271-9.

60 Tour J.M. Top-down versus bottom-up fabrication of graphene-based electronics // Chem Mater. – 2014. – Vol. 26, № 1. – P. 163-71.

61 Gao W. Graphene Oxide: Reduction Recipes, Spectroscopy, and Applications. – 1st Edition. – Publisher: Springer, 2015. – 147 p.

62 Pendolino F., Armata N. Graphene Oxide in Environmental Remediation Process // In: Springer Briefs in Applied Sciences and Technology. – Publisher: Springer, 2017. – 52 p.

63 Tkachev S., Buslaeva E., Naumkin A., Kotova S., Laure I., Gubin S. Reduced graphene oxide // Inorganic Materials. – 2012. – Vol. 48, № 8. – P. 796-802.

64 Gomez-Navarro C., Weitz R.T., Bittner A.M., Scolari M., Mews A., Burghard M., Kern K. Electronic transport properties of individual chemically reduced graphene oxide sheets // Nano Lett. – 2007. – Vol. 7, № 11. – P. 3499-3503.

65 De Silva K.K.H., Huang H.-H., Yoshimura M. Progress of reduction of graphene oxide by ascorbic acid // Applied Surface Science. – 2018. – Vol. 447. – P. 338-346.

66 Pei S., Cheng H.M. The Reduction of Graphene Oxide // Carbon. – 2012. – Vol. 50, №. 9 – P. 3210-3228.

67 Bai H., Li C., Shi G. Functional Composite Materials Based on Chemically Converted Graphene // Adv. Mater. – 2011. – Vol. 23, № 9. – P. 1089–1115.

68 Brodie B.C. On the Atomic Weight of Graphite // Philos. Trans. R. Soc. London. – 1859. – Vol. 149. – P. 249-259.

69 Staudenmaier L. Verfahren zur Darstellung der Graphitsäure // Ber. Dtsch. Chem. Ges. – 1898. – Vol. 31. – P. 1481-1487.

70 Hummers W.S., Offeman R.E. Preparation of Graphitic Oxide // J. Am. Chem. Soc. – 1958. – Vol. 80. – P. 1339.

71 Dreyer D.R., Park S., Bielawski C.W., Ruoff R.S. The chemistry of graphene oxide // Chem. Soc. Rev. – 2010. – Vol. 39, № 1. – P. 228-240.

72 Kuanyshbekov T.K., Tulegenova M.A., Baigarinova G.A., Guseinov N.R., Ilyin A.M. Investigation of temperature influence on the process of reduction of graphene oxide // VESTNIK KazNU. – 2017. – Vol. 2, № 61. – P. 18-23.

73 Chua C.K., Pumera M. Chemical reduction of graphene oxide: a synthetic chemistry viewpoint // Chem. Soc. Rev. – 2014. – Vol. 43, № 1. – P. 291-312.

74 Williams G., Seger B., Kamat P.V. Tio2-graphene nanocomposites. uv-assisted photocatalytic reduction of graphene oxide // ACS nano. – 2008. – Vol. 2, № 7. – P. 1487-1491.

75 Fan X., Peng W., Li Y., Li X., Wang S., Zhang G., Zhang F. Deoxygenation of exfoliated graphite oxide under alkaline conditions: A green route to graphene preparation // Advanced Materials (FRG). – 2008. – Vol. 20, № 23. – P. 4490-4493.

76 Wang X., Zhi L., Mullen K. Transparent, Conductive Graphene Electrodes for Dye-Sensitized Solar Cells // Nano Lett. – 2008. – Vol. 8, № 1. – P. 323-327.

77 Li X., Wang H., Robinson J.T., Sanchez H., Diankov G., Dai H. Simultaneous Nitrogen Doping and Reduction of Graphene Oxide // J. Am. Chem. Soc. – 2009. – Vol. 131. – P. 15939-15944.

78 Wu Z.-S., Ren W., Gao L., Zhao J., Chen Z., Liu B., Tang D., Yu B., Jiang C., Cheng H.-M. Synthesis of graphene sheets with high electrical conductivity and good thermal stability by hydrogen arc discharge exfoliation // ACS Nano. – 2009. – Vol. 3, № 2– P. 411-417.

79 Becerril H.A., Mao J., Liu Z., Stoltenberg R.M., Bao Z., Chen Y. Evaluation of solution-processed reduced graphene oxide films as transparent conductors // ACS Nano. – 2008. – Vol. 2, № 3. – P. 463-470.

80 Su Y., Kravets V.G., Wong S.L., Waters J., Geim A.K., Nair R.R. Impermeable barrier films and protective coatings based on reduced graphene oxide // Nature Communications. – 2014. – Vol. 5. – P 4843.

81 Go S.-H., Kim H., Yu J., You N.-H., Ku B.-C., Kim Y.-K. Synergistic effect of uv and l-ascorbic acid on the reduction of graphene oxide: Reduction kinetics and

quantum chemical simulations // Solid State Sciences. – 2018. – Vol. 84. – P. 120-125.

82 Gao J., Liu F., Liu Y., Ma N., Wang Z., Zhang X. Environment-friendly method to produce graphene that employs vitamin c and amino acid // Chemistry of Materials. – 2010. – Vol. 22, № 7. – P. 2213-2218.

83 Wang Y., Shi Z., Yin J. Facile synthesis of soluble graphene via a green reduction of graphene oxide in tea solution and its biocomposites // ACS Applied Materials & Interfaces. – 2011. – Vol. 3, № 4. – P. 1127-1133.

84 Guo Y., Sun X., Liu Y., Wang W., Qiu H., Gao J. One pot preparation of reduced graphene oxide (rgo) or au (ag) nanoparticle-rgo hybrids using chitosan as a reducing and stabilizing agent and their use in methanol electrooxidation // Carbon. – 2012. – Vol. 50, № 7. – P. 2513-2523.

85 Song P., Zhang X.-Y., Sun M., Cui X.-L., Lin Y. Synthesis of graphene nanosheets via oxalic acid-induced chemical reduction of exfoliated graphite oxide // RSC Advances. – 2012. – Vol. 2, № 3. – P. 1168-1173.

86 Тулегенова М.А., Гусейнов Н.Р., Ильин А.М., Билл Г., Қуанышбеков Т.Қ. Образование композита Ga-графен путем низкоэнергетического Ga+-ионного облучения // Вестник КазНИТУ. – 2019. – № 2(132). – Стр. 160-166.

87 Kirkland N.T., Schiller T., Medhekar N., Birbilis N. Exploring graphene as a corrosion protection barrier // Corros. Sci. – 2012. – Vol. 56. – P. 1-4.

88 Prasai D., Tuberquia J.C., Harl R.R., Jennings G.K., Bolotin K.I. Graphene: corrosion-inhibiting coating // ACS Nano – 2012. – Vol. 6. – P. 1102-1108.

89 Chen S., Brown L., Levendorf M., Cai W., Ju S.Y., Edgeworth J., Li X., Magnuson C.W., et al. Oxidation resistance of graphene–coated Cu and Cu/Ni alloy // ACS Nano – 2011. – Vol. 5. – P. 1321-1327.

90 Hsieh Y.P., Hofmann M., Chang K.-W., Jian G.J., Li Y.Y., Chen K.Y., Yang C.C., Chang W.S., Chen L.C. Complete corrosion inhibition through graphene defect passivation // ACS Nano. – 2014. – Vol. 8 – P. 443-8.

91 Ji H.P., Park J.M. Electrophoretic deposition of graphene oxide on mild carbon steel for anti-corrosion application // Surf. Coating. Technol. – 2014. – Vol. 254. – P. 167-174.

92 Jiang K., Li J., Liu J. Electrochemical codeposition of graphene platelets and nickel for improved corrosion resistant properties // RSC Adv. – 2014. – Vol. 4. – P. 36245-36252.

93 Liu J., Lei H., Li S., Yu M. Graphene dip coatings: an effective anticorrosion barrier on aluminum // Appl. Surf. Sci. – 2015. – Vol. 327. – P. 241-245.

94 Liu Y., Zhang J., Li S., Wang Y., Han Z., Ren L. Fabrication of a superhydrophobic graphene surface with excellent mechanical abrasion and corrosion resistance on an aluminum alloy substrate // RSC Adv. –2014. – Vol. 4. – P. 45389-45396.

95 Marimuthu M., Veerapandian M., Ramasundaram S., Hong S.W., Sudhagar P., Nagarajan S., Raman V., Ito E., Kim S., Yun K. Sodium functionalized graphene oxide coated titanium plates for improved corrosion resistance and cell viability // Appl. Surf. Sci. – 2014. – Vol. 293. – P. 124-131.

96 Mogera U., Kurra N., Radhakrishnan D., Narayana C., Kulkarni G.U. Low cost, rapid synthesis of graphene on Ni: an efficient barrier for corrosion and thermal oxidation // Carbon. – 2014. – Vol. 78. – P. 384-391.

97 Nayak P.K., Hsu C.J., Wang S.C., Sung J.C., Huang J.L. Graphene coated Ni films: a protective coating // Thin Solid Films. – 2013. – Vol. 529. – P. 312-316.

98 Selvam M., Saminathan K., Siva P., Saha P., Rajendran V. Corrosion behavior of Mg/graphene composite in aqueous electrolyte // Mater. Chem. Phys. – 2016. – Vol. 172. – P. 129-136.

99 Ren Y.J., Anisur M.R., Qiu W., He J.J., Al-Saadi S., Raman R.K.S. Degradation of graphene coated copper in simulated proton exchange membrane fuel cell environment: electrochemical impedance spectroscopy study // J. Power Sources. – 2017. – Vol. 362. – P. 366-372.

100 Roy R.K., Lee K.R. Biomedical applications of diamond-like carbon coatings: a review // J. Biomed. Mater. Res. Part B Appl. Biomater. – 2007. – Vol. 83, № 1. – P. 72-84.

101 Podila R., Moore T., Alexis F., Rao A.M. Graphene coatings for enhanced hemocompatibility of nitinol stents // RSC Adv. – 2013. – Vol. 3. – P. 1660-1665.

102 Li J., Wang G., Geng H., Zhu H., Zhang M., Di Z., Liu X., Chu P.K., Wang X. CVD growth of graphene on NiTi alloy for enhanced biological activity // ACS Appl. Mater. Interfaces. – 2015. – Vol. 7. – P. 19876-19881.

103 Ye X., Long J., Lin Z., Zhang H., Zhu H., Zhong M. Direct laser fabrication of large–area and patterned graphene at room temperature // Carbon. – 2014. – Vol. 68. – P. 784-790.

104 Ye X., Lin Z., Zhang H., Zhu H., Liu Z., Zhong M. Protecting carbon steel from corrosion by laser in situ grown graphene films // Carbon. – 2015. – Vol. 94. – P. 326-334.

105 Zhu M., Du Z., Yin Z., Zhou W., Liu Z., Tsang S.H., Teo E.H.T. Low-temperature in situ growth of graphene on metallic substrates and its application in anticorrosion // ACS Appl. Mater. Interfaces. – 2016. – Vol. 8. – P. 502-510.

106 Zhao Y., Xie Y., Hui Y.Y., Tang L., Jie W., Jiang Y., Xu L., Shu P.L., Chai Y. Highly impermeable and transparent graphene as an ultra-thin protection barrier for Ag thin films // J. Mater. Chem. C. – 2013. – Vol. 1. – P. 4956-4961.

107 Nair R.R., Wu H.A., Jayaram P.N., Grigorieva I.V., Geim A.K. Unimpeded permeation of water through helium-leak-tight graphene-based membranes // Science. – 2012. – Vol. 335. – P. 442-444.

108 Joshi R.K., et al. Precise and Ultrafast molecular sieving through graphene oxide membranes // Science. – 2014. – Vol. 343. – P. 752-754.

109 Kim H. W., et al. Selective gas transport through few-layered graphene and graphene oxide membranes // Science. – 2013. – Vol. 342. – P. 91-95.

110 Li H., et al. Ultrathin molecular sieving graphene oxide membranes for selective hydrogen separation // Science. – 2013. – Vol. 342. – P. 95-98.

111 Kang D., et al. Oxidation resistance of iron and copper foils coated with reduced graphene oxide multilayers // ACS Nano. – 2012. – Vol. 6. – P. 7763 -769.

112 Yamaguchi H., et al. Reduced graphene oxide thin films as ultrabarriers for organic electronics // Adv. Energy Mater. – 2014. – Vol. 4 – P. 1300986.

113 Yoo B.M., Shin H.J., Yoon H.W., Park H.B. Graphene and graphene oxide and their uses in barrier polymers // J. Appl. Polym. Sci. – 2014. – Vol. 131. – P. 39628.

114 Huang H.-D., et al. High barrier graphene oxide nanosheet/poly(vinyl alcohol) nanocomposite films // J. Membrane Sci. – 2012. – Vol. 409. – P. 156-163.

115 Yang J., et al. Thermal reduced graphene based poly(ethylene vinyl alcohol) nanocomposites: enhanced mechanical properties, gas barrier, water resistance, and thermal stability // Ind. Eng. Chem. Res. – 2013. – Vol. 52. – P. 16745-16754.

116 Yang Y.H., Bolling L., Priolo M.A., Grunlan J.C. Super gas barrier and selectivity of graphene oxide-polymer multilayer thin films // Adv. Mater. – 2013. – Vol. 25. – P. 503-508.

117 Pei S., Zhao J., Du J., Ren W., Cheng H.-M. Direct reduction of graphene oxide films into highly conductive and flexible graphene films by hydrohalic acids // Carbon. – 2010. – Vol. 48. – P. 4466-4474.

118 Moon I.K., Lee J., Ruoff R.S., Lee H. Reduced graphene oxide by chemical graphitization // Nat. Commun. – 2010. – Vol. 1, Article number 73. – P. 1-6.

119 Zhang J., et al. Reduction of graphene oxide via L-ascorbic acid // Chem. Commun. – 2010. – Vol. 46. – P. 1112-1114.

120 Fernandez-Merino M.J., et al. Vitamin C is an ideal substitute for hydrazine in the reduction of graphene oxide suspensions // J. Phys. Chem. C. – 2010. – Vol. 114, №14. – P. 6426-6432.

121 Harris D.C., Bertolucci M.D. Symmetry and spectroscopy: An Introduction to Vibrational and Electronic Spectroscopy. – 1st ed. – Publisher: Oxford University Press, New York, 1978. – 550 p.

122 Zingarelli J.C. Detection of Residual Stress in SiC MEMS Using μ-Raman Spectroscopy // Theses and Dissertations. – 2005. – P. 25.

123 Das R.S., Agrawal Y.K. Raman spectroscopy: Recent advancements, techniques and applications // Vib. Spectrosc. – 2011. – Vol. 57. – P. 163-176.

124 Mercier B. Density fluctuations measurement by rayleigh scattering using a single photomultiplier // Aiaa. J. – 2018. – Vol. 56. – P. 1310-1316.

125 Smekal A. Zur quantentheorie der dispersion // Naturwissenschaften. – 1923. – Vol. 11. – P. 873-875.

126 Raman C.V., Krishnan K.S. A new type of secondary radiation // Nature. – 1928. – Vol. 121. – P. 501-502.

127 Gogotsi Y., Domnich V. High-Pressure Surface Science and Engineering. – 1st Edition. – 2004. – P. 349-365.

128 Otto A.K., Rechtsteiner G.A., Felix C., Hampe O., Jarrold M.F., Van Duyne R.P. Raman spectra and calculated vibrational frequencies of size-selected C16, C18, and C20 clusters // Chem. Phys. – 1998. – Vol. 109. – P. 9651-9655.

129 Tian Z.Q., Yang Z.L., Ren B., Li J.F., Zhang Y., Lin X.F., Hu J.W., Wu D.Y. Surface-enhanced Raman scattering from transition metals with special surface

morphology and nanoparticle shape // Faraday Discuss. – 2006. – Vol. 132. – P. 159-170.

130 Kurouski D., Van Duyne R.P. In situ detection and identification of hair dyes using surface-enhanced Raman spectroscopy (SERS) // Anal. Chem. – 2015. – Vol. 87. – P. 2901-2906.

131 Wang K.H., Huang M.Z., Chen J., Lin L.L., Kong L.L., Liu X., Wang H., Lin M.S. A “drop-wipe-test” SERS method for rapid detection of pesticide residues in fruits // Raman. Spectrosc. – 2018. – Vol. 49. – P. 493-498.

132 Sharma B., Frontiera R.R., Henry A.I. SERS: Materials, applications, and the future // Mater. Today. – 2012. – Vol. 15. – P. 16-25.

133 Букалов С.С. Исследование строения графитов и некоторых других sp2 углеродных материалов методами микро-спектроскопии КР и рентгеновской дифрактометрии // Рос. Хим. Ж. – 2006. – С. 83-91.

134 Ferrari A.C., Meyer J.C., Scardaci V., Casiraghi C., Lazzeri M., Mauri F., Piscanec S, Da Jiang, Novoselov K.S., Roth S., Geim A.K. The Raman Fingerprint of Graphene // [Electronic resource] - Access mode: arXiv:condmat/0606284. – P. 1-5.

135 Xu Z., He Z., Song Y., Fu X., Rommel M., Luo X., Hartmaier A., Zhang J., Fang F. Topic Review: Application of Raman Spectroscopy Characterization in Micro/Nano-machining // Micromachines. – 2018. – Vol. 9, № 7. – P. 1-23.

136 Web-Resource, Electron Beam/Specimen Interactions. https://www.mse.iastate.edu/research/microscopy/how-does-the-sem-work/college-electron-microscope/beam-interactions/ 02.09.2022.

137 Рид С., Дж Б. Электронно-зондовый микроанализ и растровая электронная микроскопия в геологии. – Издание: Техносфера, Москва, 2008. – 232 с.

138 Levitin V. Simulation of Solids Starting from the First Principles (“ab initio” Models) // Interatomic Bonding in Solids: Fundamentals, Simulation, and Applications. – 2014. – P. 109-130.

139 Hollingsworth S.A., Dror R.O. Molecular Dynamics Simulation for All // Neuron. – 2018. – Vol. 99, № 6. – P. 1129-1143.

140 Muralidhar K. Monte Carlo Simulation // Encyclopedia of Information Systems. – 2003. – Vol. 3. – P. 193-201.

141 Kohn W. Nobel lecture: electronic structure of matter–wave functions and density functionals // Rev. Mod. Phys. – 1999. – Vol. 71, № 5. – P. 1253-1266.

142 Rubinstein R.Y. Simulation and the Monte Carlo method. – Publisher: John Wiley and Sons, Inc, 1981. – 278 p.

143 Web-Resource, DMol3. https://ru.abcdef.wiki/wiki/DMol3 10.09.2022.

144 Bunch J.S., Verbridge S.S., Alden J.S., Van der Zande A.M., Parpia J.M., Craighead H.G., McEuen P.L. Impermeable atomic membranes from graphene sheets // Nano Lett. – 2008. – Vol. 8, № 8. – P. 2458-2462.

145 Ilyin A.M., Guseinov N.R., Tsyganov I.A., Nemkaeva R.R. Computer Simulation and Experimental Study of Graphane-Like Structures, Formed by Electrolytic Hydrogenation // Physica E. – 2011. – Vol. 43, № 6. – P. 1262-1265.

146 Ilyin A.M., Beall G.W., Tsyganov I.A. Simulation and Study of Bridge-Like Radiation Defects in the Carbon Nano-Structures // Journal of Computational and Theoretical Nanoscience. – 2010. – V. 7, № 10. – P. 2004-2007.

147 Ilyin A.M., Beall G.W. Computer Simulation of Graphene-Metal Composite Induced by Radiation // Proceedings "Composite Materials"of NanoTech Conference & Expo. – Boston, USA, 2011. – Vol. 1, Ch.5. – P. 574-576.

148 Ilyin A.M., Guseinov N.R., Kuanyshbekov T.K., Beall G.W., Tulegenova M.A. Computer Simulation and First Principles Study of Ga-Doped Graphene Nanostructures // Journal of Computational and Theoretical Nanoscience. – 2019. – Vol. 16. – P. 39-41.

149 Tulegenova M., Ilyin A., Guseinov N., Beall G., Kuanyshbekov T. Computer Simulation of the Effect of Structural Defects on the Effectiveness of the Graphene's Protective Properties // Journal of Computational and Theoretical Nanoscience. – 2019. – Vol. 16, № 1. – P. 351-354.

150 Banhart F., Kotakoski J., Krasheninnikov A.V. Structural Defects in Graphene // ACS Nano. – 2010. – Vol. 5. – P. 26-41.

151 Li X., Cai W., An J.H., Kim S., Nah J., Yang D., Piner, R., et. al. Large-area synthesis of high-quality and uniform graphene films on copper foils // Science. – 2009. – Vol. 324. – P. 1312-1314.

152 Ferrari A.C., Meyer J.C., Scardaci V., Casiraghi C., Lazzeri M., Mauri F., Piscanec S., Jiang D., Novoselov K.S., Roth S., Geim A.K. Raman Spectrum of Graphene and Graphene Layers // Phys. Rev. Lett. – 2006. – Vol. 97. – P. 187401.

153 Nguyen V.T., Le H.D., Nguyen V.C., Ngo T.T.T., Le D.Q., Nguyen X.N., Phan N.M. Synthesis of multi-layer graphene films on copper tape by atmospheric pressure chemical vapor deposition method // Adv. Nat. Sci.: Nanosci. Nanotechnol. – 2013. – Vol. 4. – P. 035012.

154 Ren Y., Zhu C., et. al. An improved method for transferring grapheme grown by chemical vapor deposition // Brief Reports and Reviews. – 2012. – Vol. 7, № 1. – P. 1150001.

155 Odahara G., Otani S., Oshima C., Suzuki M., Yasue T., Koshikawa T. In-situ observation of graphene growth on Ni(111) // Surface Science. – 2011. – Vol. 605. – P. 1095-1098.

156 Fogarassy Z., Rümmeli M.H. Dominantly epitaxial growth of graphene on Ni (111) substrate // Surface Science. – 2014. – Vol. 314. – P. 490-499.

157 Gierz I., Suzuki T., Weitz R.T., Lee D.S., Krauss B., Riedl C., Starke U., Höchst H., Smet J.H., Ast C.R., Kern K. Electronic decoupling of an epitaxial graphene monolayer by gold intercalation // Physical Reveiw B. – 2010. - Vol. 81. – P. 235408.

158 Kuanyshbekov T.K., Ilyin A.M., Beall G.W., Guseinov N.R. Creation of a Humidity Sensor Based on Functionalized Graphene Nanostructures // Sensors & Transducers. 2019. – Vol. 229, № 1. – P. 39-46.

159 Kuanyshbekov T.K., Iliyn A.M., Beall G.W., Guseinov N.R., Tulegenova M.A. Sensitive humidity sensor based on functionalized graphene // Abstract proceedings of 4th International Conference on Sensors Engineering and Electronics

Instrumentation Advances “SEIA' 2018”. – Amsterdam, The Netherlands, 2018. – P. 45-46.

160 Tulegenova M., Ilyin A., Beall G., Guseinov N. Anticorrosive coatings based on few-layer graphene // Journal of Materials Science and Engineering B. – 2018. – Vol. 8, № 7-8. – P. 179-184.

161 Тулегенова М.А., Куанышбеков Т.К., Ильин А.М., Гусейнов Н.Р. Защита поверхности меди от температурной коррозии с помощью малослойных графеновых наноструктур // Вестник КазНИТУ. – 2018. - № 2 (126). – С. 262-267.

162 Tulegenova M.A., Kuanyshbekov T.K., Guseinov N.R., Ilyin A.M., Beall G.W. Laboratory technology of copper surface protection by means of few-layer graphene nanostructures // Abstract proceedings of 5th Global Conference on Polymer and Composite Materials “PCM 2018”. – Kitakyushu, Japan, 2018. – P. 54.

163 Тулегенова М.А., Куанышбеков Т.К., Ильин А.М., Гусейнов Н.Р. Защита поверхности никеля от температурной коррозии с помощью малослойных графеновых наноструктур // Сборник трудов Международной научной конференции студентов и молодых ученых «Фараби әлемі». – Алматы, Казахстан, 2018. – С. 229.

164 Тулегенова М.А., Қуанышбеков Т.Қ., Гусейнов Н.Р., Ильин А.М. Антикоррозионные защитные покрытия на основе малослойных графеновых наноструктур // Сборник трудов V международной научной конференции «Современные проблемы физики конденсированного состояния, нанотехнологии и наноматериалов (Сарсембиновские чтения)». – Алматы, Казахстан, 2018. – С. 120-125.

165 Tulegenova M.A., Guseinov N.R., Ilyin A.M., Beall G.W. Few-layer graphene as an anticorrosive coating for copper // Белая книга по нанотехнологиям. – 2018. – С. 313-317.

166 Hourani W., Gorbenko V., Barnes J.-P., Guedj C., Cipro R., Moeyaert J., David S., Bassani F., Baron T., Martinez E. 3D Auger quantitative depth profiling of individual nanoscaled III - V heterostructures // J. Electron Spectrosc. Relat. Phenom. – 2016. – V.213. – P. 1-10.

167 Guseinov N.R., Ilyin A.M. Electrostatic energy analyzer for nanotechnology applications // J. Electron Spectrosc. Relat. Phenom. – 2021. – Vol. 246. – 147031.

168 Shard A.G. A straightforward method for interpreting XPS data from core–shell nanoparticles // J. Phys. Chem. C. – 2012. – Vol. 116, № 31. – P. 16806-16813.

169 Ilyin A.M. Auger Electron Spectroscopy. In: Microscopy Methods in Nanomaterials Characterization / Edited by Thomas S., Thomas R., Zachariah A.K., Mishra R.K. – Publisher: Elsevier, 2017. – P. 363-381.

170 Guseinov N.R., Ilyin A.M. Subthreshold radiation damage in few-layer graphene nanostructures due to low-energy electron irradiation // New Approaches in Engineering Research. – 2021. – Vol. 10, Ch. 4. – P. 32-40.

171 Cant D.J.H., Wang Y.-C., Castner D.G., Shard A.G. A technique for calculation of shell thicknesses for core-shell nanoparticles from XPS data // Surf. Interface Anal. – 2016. – Vol. 48, № 5. – P. 274-282.

172 Ecke G., Cimalla V., Tonish K., Lebedev V., Romanus H., Ambacher O., Liday J. Analysis of nanostructures by means of Auger electron spectroscopy // J. Electr. Eng. – 2007. – Vol. 58, № 6. – P. 301-306.

173 Rades S., Wirth T., Unger W. Investigation of Silica Nanoparticles by Auger Electron Spectroscopy // Surf. Interface Anal. – 2014. – Vol. 46, № (10-11). – P. 952-956.

174 Xu M., Fujita D., Gao J., Hanagata N. Auger Electron Spectroscopy: A Rational Method for Determining Thickness of Graphene Films // ACS Nano. – 2010. – Vol.4, № 5. – P. 2937-2945.

175 Raman S.N., Paul D.F., Hammond J.S., Bomben K.D. Auger Electron Spectroscopy and its Application to Nanotechnology // Microscopy Today. – 2011. – Vol. 19, № 2. – P.12-15.

176 Kalaga K., Shkrob I.A., Haash R.T., Peebles C., Bareno J., Abraham D.P. Auger Electrons as Probes for Composite Micro- and Nanostructured Materials: Application to Solid Electrolyte Interphases in Graphite and Silicon-Graphite Electrodes // J. Phys. Chem. C. – 2017. – Vol. 121, № 42. – P. 33332-33346.

177 Baer D.R., Gaspar D.J., Nachimuthu P., Techane S.D., Castner D.G. Application of Surface Chemical Analysis Tools for Characterization of Nanoparticles // Anal. Bioanal. Chem. – 2010. – Vol. 396, № 3. – P. 983-1002.

178 Kaciulis S., Mezzi A., Calvani P., Trucchi D.M. Electron spectroscopy of the main allotropes of carbon // Surface and Interface analysis. – 2014. – Vol. 46, № 10-11. – P. 966-969.

179 Zha X., Walker C.G.H., El-Gomati M. Auger Electron Spectroscopy in high vacuum: nanocharacterization in the Scanning Electron Microscope // Journal of Physics: Conference Series. – 2014. – Vol. 522, № 1. – P. 012027.

180 Xu M., Fujita D., Hanagata N. Monitoring Electron-beam Irradiation Effects on Graphene by Temporal Auger Electron Spectroscopy // Nanotechnology. – 2010. – Vol. 21, № 26. – P. 265705-707.

181 Korin E., Froumin N., Cohen S. Surface analysis of Nanocomplexes by X-ray Photoelectron Spectroscopy (XPS) // ACS Biomater. Sci. Eng. – 2017. – Vol. 3, № 6. – P. 882-889.

182 Kong L., Guo Y., Wang X., Zhang X. Double-walled hierarchical porous silica nanotubes loaded Au nanoparticles in the interlayer as a high-performance catalyst // Nanotechnology. – 2020. – Vol. 31, № 1. – 12 p.

183 Cubric D., De Fanis A., Konishi I., Kumashiro S. Parallel acquisition electrostatic electron energy analyzers for high throughput nano-analysis // Nucl. Instruments Methods Phys. Res. Sect. A. – 2011. – Vol. 645, № 1. – P.227-233.

184 Dimitriou A., Laoutaris A., Madesis I., Doukas S., Benis E.P., Sulik B., Sise O., Lagoyannis A., Axiotis M., Zouros T.J.M. High resolution Auger projectile electron spectroscopy of Li-like ions produced by electron capture in collisions of He-like ions with gaseous targets // J. Atomic, Molecular Condensate & Nanophysics. – 2016. – Vol. 3, № 2. – P. 125-131.

185 Hoffman S. Practice of Surface and Interface Analysis with AES and XPS. In book: Auger- and X-ray Photoelectron Spectroscopy in Materials Science / Edited by Ertl G., Luth H., Mills D.L. – Publisher: Springer, 2013. – P.409-449.

186 Werner W.S., Smekal W., Hish T., Himmelsbach J., Powell C.J. Simulation of electron spectra for surface analysis (SESSA) for quantitative interpretation of (hard) X-ray photoelectron spectra (HAXPES) // J. Electron Spectrosc. Relat. Phenom. – 2013. – Vol. 190, Part B, P. 137-143.

187 Werner W.S. Electron transport for spectrum analysis and experimental design // J. Electron Spectrosc. Relat. Phenom. – 2010. – Vol. 178-179. – P. 154-179.

188 Radvanyi E., De Vito E., Porsher W., Danet J., Desbois P., Colin J.-F., Si Larbi S.J. Study of lithiation mechanisms in silicon electrodes by Auger Electron Spectroscopy // J. Mater. Chem. A. – 2013. – Vol. 1. – P. 4956-4959.

189 Mahoney J., Monroe C., Swartley A.M., et al., Surface analysis using X-ray photoelectron spectroscopy // Spectroscopy Letters. – 2020. – Vol. 53, №10. – P. 726-736.

190 Powell C.J., Jablonski A. Progress in quantitative surface analysis by X-ray photoelectron spectroscopy: current status and perspectives // J. Electron Spectrosc. Relat. Phenom. – 2010. – Vol. 178-179. – P. 331- 346.

191 Ilyin A.M., Golovanov V.N. Auger spectroscopy study of the stress enhanced impurity segregation in a Cr-Mo-V steel // J. Nucl. Mater. – 1996. – Vol. 233-237. – P. 233-235.

192 Ilyin A.M. Some features of grain boundary segregations in sensitized austenitic stainless steel // J. Nucl. Mater. – 1998. – Vol. 252, № 1-2. – P. 168-170.

193 Debehets J., Homm P., Menghini M., Chambers S.A., Marchiori M., Heyns M., Locquet J.P., Seo J.W. Detecting Fermi-level shifts by Auger electron spectroscopy in Si and GaAs // Appl. Surf. Sci. – 2018. – Vol. 440. – P. 386-395.

194 Aronova M.A., Leapman R.D. Elemental mapping by electron energy loss spectroscopy in biology // Methods Mol. Biol. – 2013. – Vol. 950. – P. 209-26.

195 Kapp N., Studer D., Gehr P., Geiser M. Electron Energy-Loss Spectroscopy as a Tool for Elemental Analysis in Biological Specimens // Methods Mol. Biol. – 2007. – Vol. 369. – P. 431-47.

196 Barabash S., Sauvaud J.-A., Gunell H., et al. The analyser of space plasmas and energetic atoms (ASPERA-4) for the Venus Express mission // Planetary and Space Science. – 2007. – Vol. 55. – P.1772-1792.

197 Cara A., Lavraud B., Fedorov A., et al. Electrostatic analyzer design for solar wind proton measurements with high temporal, energy, and angular resolutions // JGR Space Physics. – 2017. – Vol. 122, № 2. – P. 1439-1450.

198 Kazama Y. Designing a toroidal top-hat energy analyzer for low-energy electron measurement. In book: An Introduction to Space Instrumentation / Edited by Oyama K., Cheng C.Z. – Publisher: TERRAPUB, 2013. – P.181-192.

199 Barabash S., Lundin R., Andersson H., et al. The analyzer of space plasmas and energetic atoms (ASPERA-3) for the Mars Express mission // Space Science Reviews. – 2006. – Vol. 126, № 1-4. – P. 113-164.

200 Victor A.L., Zurbuchen T.H., Gallimore A.D. Top hat electrostatic analyzer for far-field electric propulsion plume diagnostics // Review of Scientific Instruments. – 2006. – Vol. 77, № 1. – P. 013505.

201 Dreval M., Rohraff D., Xiao C., Hirose A. Retarding field energy analyzer for the Saskatchewan Torus-Modified plasma boundary // Review of Scientific Instruments. – 2009. – Vol. 80, № 10. – P. 103505.

202 Clark. G, Allegrini F., McComas D.J., Louarn P. Modeling the response of a top hat electrostatic analyzer in an external magnetic field: Experimental validation with the Juno JADE-E sensor // Journal of Geophysical Research: Space Physics. – 2016. – Vol. 121, № 6. – P. 5121-5136.

203 Nicolaou G., Wicks R.T., Rae I.J., Kataria D.O. Evaluating the performance of a plasma analyzer for a space weather monitor mission concept // Space Weather. – 2020. – Vol. 18, № 12. – P. e2020SW002559.

204 Kasahara S., Yokota S., Mitani T., et al. Medium-energy particle experiments—electron analyzer (MEP-e) for the exploration of energization and radiation in geospace (ERG) mission // Earth Planets and Space. – 2018. – Vol. 70. – 16 p.

205 Kasahara S., Asamura K., Saito Y., Takashima T, et al. Cusp type electrostatic analyzer for measurements of medium energy charged particles // Rev. Sci. Instrum. – 2006. – Vol. 77. – P. 123303.

206 Morel X., Berthomier M., Berthelier J.-J. Electrostatic analyzer with a 3-D instantaneous field of view for fast measurements of plasma distribution functions in space // Journal of Geophysical Research: Space Physics. – 2017. – Vol. 122, № 3. – P. 3397-3410.

207 Ilyin A.M., Ilyina I.A. High-resolving electrostatic charged particles energy analyzer with fine tuning for space investigations // Journal of Instrumentation. – 2014. – Vol. 9. – P. P08005.

208 Ilyin A.M., Ilyina I.A. New electrostatic energy analyzer for space plasma measurements // Journal of Instrumentation. – 2007. – Vol. 2. – P. P01002.

209 Ilyin A.M., Ilyina I.A. An electrostatic face-field energy analyzer for space and plasma measurements // Meas. Sci. Technol. – 2007. – Vol. 18, № 3. – P. 724-726.

210 Gorelik V. Cylindrical mirror analyzer with entrance angles from 90.5° to 98.5° // J. Electron Spectrosc. Relat. Phenom. – 2012. – Vol. 185, № 3-4. – P. 53-54.

211 Kobayashi E., Seo J., Nambu A., Mase K. Development of a miniature double-pass cylindrical mirror electron energy analyzer (DPCMA) and its application to Auger photoelectron coincidence spectroscopy (APECS) // Surf. Sci. – 2007. – Vol. 601, № 17. – P. 3589-3592.

212 Edwards Jr D. The segmented cylindrical mirror analyzer (CMA) // J. Electron Spectrosc. Relat. Phenom. – 2016. – Vol. 209. – P. 46-52.

213 Edwards Jr D. Improving the performance of the cylindrical mirror analyzer II: Reducing the dependence of energy resolution on sample position // J. Electron Spectrosc. Relat. Phenom. – 2016. – Vol. 212. – P. 62-73.

214 Ilyin A.M. Relativistic consideration of a cylindrical mirror field focusing for a distant charged particle source // Nuclear Instruments and Methods in Physics Research Section A: Accelerators, Spectrometers, Detectors and Associated Equipment. – 2002. – Vol. 485, № 3. – P. 234-237.

215 Ilyin A.M. About some focusing properties of a cylindrical field // J. Electron Spectrosc. Relat. Phenom. – 2000. – Vol. 113, № 1. – P. 1-2.

216 Ilyin A.M., Ilyina I.A. Electrostatic energy analyzers for high energy charged particle beams // Journal of Instrumentation. – 2016. – Vol. 11. – P. P02010.

217 Bedington R., Kataria D., Smith A. A miniaturised, nested-cylindrical electrostatic analyser geometry for dual electron and ion, multi-energy measurements // Nuclear Instruments and Methods in Physics Research Section A: Accelerators, Spectrometers, Detectors and Associated Equipment. – 2015. – Vol. 793. – P. 92-100.

218 Dogan M., Ulu M., Gennarakis G.G., Zouros T.J.M. Experimental energy resolution of a paracentric hemispherical deflector analyzer for different entry positions and bias. // Rev. Sci. Instrum. – 2013. – Vol. 84. – P. 043105.

219 Dogan M., Ulu M., Sise O. Design, simulation and construction of an electron-electron coincidence spectrometer // J. Electron Spectrosc. Relat. Phenom. – 2007. – Vol. 161, № 1-3. – P. 58-62.

220 Zouros T.J.M., Benis E.P. Optimal energy resolution of a hemispherical analyzer with virtual entry // Appl. Phys. Lett. – 2005. – Vol. 86, № 9. – P. 094105.

221 Tusche C., Chen Y.-J., Schneider C.M., Kirschner J. Imaging properties of hemispherical electrostatic energy analyzers for high resolution momentum microscopy // Ultramicroscopy. – 2019. – Vol. 206. – P. 112815.

222 Benis E.P., Zouros T.J.M. The hemispherical deflector analyser revisited II. Electron-optical properties // J. Electron Spectrosc. Relat. Phenom. – 2008. – Vol. 163, № 1-3. – P. 28-39.

223 Louette P., Delage A., Roy D., Thiry P.A., Caudano R. An interelectrode distance dependent fringing field correction for the hemispherical deflector analyzer // J. Electron Spectrosc. Relat. Phenom. – 1990. – Vol. 52. – P. 867-874.

224 Cipriani F., Leblanc F., Illiano J.-M., Berthelier J.-J. A hemispherical retarding field analyzer to characterize spatially and angularly extended electron beams // Eur. Phys. J. Appl. Phys. – 2012. – Vol. 60, № 2. – P. 21002.

225 Ilyin A.M., Borisov B.A. Second-order focusing of a bounded cylindrical field for a distant source // Meas. Sci. Technol. – 2001. – Vol. 12, № 11. – P. 2015-2017.

226 Ilyin A.M., Guseinov N.R., Tulegenova M.A. Conical face-field electrostatic energy analyzers for investigating nanomaterials // Journal of Electron Spectroscopy and Related Phenomena. – 2022. – Vol. 257. – P. 147203.

227 Ren S., Cui M., Li W., Pu J., Xue Q., Wang L. N-doping of graphene: toward a long-term corrosion protection of Cu // J. Mater. Chem. A. – 2018. – Vol. 6. – P. 24136-24148.

228 Ding J., Zhao H., Ji D., Xu B., Zhao X., Wang Z., Wang D., Zhou Q., Yu H. Achieving Long-Term Anticorrosion via the Inhibition of Graphene's Electrical Activity // J. Mater. Chem. A. – 2019. – Vol. 7. – P. 2864-2874.

229 Jorio A., Martins Ferreira E.H., Cançado L.G., Achete C.A., Capaz R.B. Measuring Disorder in Graphene with Raman Spectroscopy // Physics and Applications of Graphene – Experiments. – 2011. – P. 439-454.

230 Hohenberg P., Kohn W. Inhomogeneous Electron Gas // Physical Review. – 1964. – Vol.136, № 3B. – P. B864-B871.

231 Bagayoko D. Understanding density functional theory (DFT) and completing it in practice // AIP Advances. – 2014. – Vol. 4. – P. 127104.

232 Kohn W., Sham L. J. Self-Consistent Equations Including Exchange and Correlation Effects // Phys. Rev. – 1965. – Vol.140, № 4A. – P. A1133-A1138.